

**Dynamic Properties of Quantum Dot  
Distributed Feedback Lasers**

By Hui Su

## **Acknowledgements**

I am indebted to my advisor Dr. Luke F. Lester for his advising of my PhD study. The graduate study under his guidance is one of the most memorable experiences in my life. I really appreciate the various opportunities and training he offered me during these years. I also would like to thank Prof. Kevin J. Malloy, Prof. Ravi Jain, Prof. Sanjay Krishna and Prof. Chaouki Abdallah for being on my dissertation committee and for reading and commenting on my thesis. Special thanks to Prof. Kevin J. Malloy for helpful discussions and support on equipment during the past years.

Thanks to Zia Laser, inc. for providing the quantum dot distributed feedback lasers studied in this dissertation. I would like to thank Dr. Lei Zhang for his help and collaboration on the high speed measurements and Dr. Allen L. Gray for growing the quantum dot wafers.

I have also benefited greatly from the interaction and collaboration with many of the people at CHTM. Without the testing setups built up by Dr. T. C. Newell, my experiments should have been much more time-consuming. I appreciate the help from Dr. RongHua Wang, Dr. XiaoDong Huang and YongChun Xin on my learning of clean-room processing.

Finally, I like to thank my parents, JinHua Su and LiMei Peng, for their support of my study. They did their best to make a good education possible to me. I am also grateful to my wife, Ling Song, and our son, Henry Su for the support and happiness they give me as a family.

## Publication List

1. H. Su, L. Zhang, A. L. Gray, R. Wang, T. C. Newell, K. J. Malloy and L. F. Lester, "High External Feedback Resistance of Laterally Loss Coupled Distributed Feedback Quantum Dot Semiconductor Lasers", *IEEE PHOTONICS TECHNOLOGY LETTERS* **15**, 1504-1506 (2003).
2. Zoltan Bakonyi, Hui Su, George Onishchukov, Luke F. Lester, Allen L. Gray, Timothy C. Newell, and Andreas Tünnermann, "High Gain Quantum Dot Semiconductor Optical Amplifier for 1300 nm", *IEEE Journal of Quantum Electronics*, Nov 2003, V.39, no.11, pp. 1409-1414.
3. H. Su, L. Zhang, A. L. Gray, R. Wang, T. C. Newell and L. F. Lester, "Linewidth study of GaAs-InGaAs Quantum Dot Distributed Feedback Lasers" accepted by *IEEE Photonics Technology Letter*.
4. H. Su, L. Zhang, A. L. Gray, R. Wang, T. C. Newell, and L. F. Lester, "External feedback effects on quantum dot laterally-loss-coupled distributed feedback lasers", TuD2, LEOS conference, Oct. 2003, Tucson, Arizona, USA.
5. H. Su, L. Zhang, A. L. Gray, R. Wang, T. C. Newell, K. J. Malloy and L. F. Lester, "Linewidth of quantum dot laterally-loss-coupled distributed feedback lasers with and without external feedback", Photonics West, Jan 2004.
6. Lester, L. F. , Gray, A. L., Zhang, L., Newell, T. C., Wang, R., Nabulsi, F., Olona, L., Varagnis, P. M., Bakonyi, Z., Onishchukov, G., Tünnermann, A., Su, H., Stintz, A., Zou, J., and Malloy, K. J., "Quantum Dot Device Technology on GaAs: DFB lasers, tunable lasers, and SOA's", CLEO'2003, Baltimore, Maryland, USA
7. Onishchukov, G., Su, H., Bakonyi, Z., Lester, L. F., Gray, A. L., Newell, T. C., and Tunnermann, A., "1300-nm Quantum Dot Semiconductor Optical Amplifier" 29<sup>th</sup> European Conference on Optical Communications / 14th International Conference on Integrated Optics and Optical Fibre Communication, 2003, September 21 - 25, Rimini, Italy, paper We4.P.89
8. Bakonyi, Z., Onishchukov, G., Tunnermann, A., Su, H., Lester, L. F., Gray, A. L., and Newell, T. C., "Quantum Dot (InAs/InGaAs DWELL) Semiconductor Optical Amplifier" CLEO/Europe'2003 , 2003, June 23 - 27, Munich, Germany, paper CC9-3-Wed.
9. Petros M. Varangis<sup>1</sup>, L. Zhang<sup>1</sup>, A. L. Gray<sup>1</sup>, R. Wang<sup>1</sup>, S. Luong<sup>1</sup>, L. Cheng<sup>1</sup>, K. Sun<sup>1</sup>, C. Bryan<sup>1</sup>, F. Nabulsi<sup>1</sup>, T. Whittington<sup>1</sup>, Z. Zou<sup>1</sup>, L. Olona<sup>1</sup>, C. Wiggins<sup>1</sup>, T. Tumolillo<sup>1</sup>, J. Zilko<sup>1</sup>, H. Su<sup>2</sup>, K. J. Malloy<sup>2</sup>, L. F. Lester<sup>2</sup>; <sup>1</sup>Zia Laser, Inc., USA, <sup>2</sup>Ctr. for High Technology Materials, Univ. of New Mexico, USA., "Quantum dot photonic devices and applications", PThD1, PHAST/CLEOS 2004, San Francisco, CA, USA.
10. H. Su, L. Zhang, A. L. Gray, R. Wang and L. F. Lester, "*High speed and linewidth performance of quantum dot distributed feedback lasers*", IEEE semiconductor Laser Workshop, 2004, San Francisco, CA, USA..
11. L.F. Lester, H. Su, L. Zhang, R. Wang, and A. L Gray, "*Feedback Resistance and Linewidth of Quantum Dot DFB Lasers*", ETOS, July, 2004, University College Cork, Ireland.
12. Luke. F. Lester, H. Su etc., "*1.3 to 1.6  $\mu\text{m}$  Quantum Dot Lasers.*" 16<sup>th</sup> International conference on indium Phosphide and Related Materials (IPRM'04), May 31- June 4, 2004, Kagoshima, Japan.

# **Dynamic properties of quantum dot distributed feedback lasers**

by

**Hui Su**

B.S., Physics, Wuhan University, P. R. China, 1993

Ph.D., Physical Chemistry, Fujian Institute of Research on the Structure of Matters,  
Chinese Academy of Sciences, P. R. China, 1998

Ph. D, Optical Science and Engineering, University of New Mexico, 2004

## **ABSTRACT**

Semiconductor quantum dots (QDs) are nano-structures with three-dimensional spatial confinement of electrons and holes, representing the ultimate case of the application of the size quantization concept to semiconductor hetero-structures. The knowledge about the dynamic properties of QD semiconductor diode lasers is essential to improve the device performance and understand the physics of the QDs.

In this dissertation, the dynamic properties of QD distributed feedback lasers (DFBs) are studied. The response function of QD DFBs under external modulation is characterized and the gain compression with photon density is identified to be the limiting factor of the modulation bandwidth. The enhancement of the gain compression by the gain saturation with the carrier density in QDs is analyzed for the first time with suggestions to improve the high speed performance of the devices by increasing the maximum gain of the QD medium.

The linewidth of the QD DFBs are found to be more than one order of magnitude narrower than that of conventional quantum well (QW) DFBs at comparable output powers. The figure of merit for the narrow linewidth is identified by the comparison

between different semiconductor materials, including bulk, QWs and QDs. Linewidth rebroadening and the effects of gain offset are also investigated.

The effects of external feedback on the QD DFBs are compared to QW DFBs. Higher external feedback resistance is found in QD DFBs with an 8-dB improvement in terms of the coherence collapse of the devices and 20-dB improvement in terms of the degradation of the signal-to-noise ratio under 2.5 Gbps modulation. This result enables the isolator-free operation of the QD DFBs in real communication systems based on the IEEE 802.3ae Ethernet standard.

Finally, the chirp of QD DFBs is studied by time-resolved-chirp measurements. The wavelength chirping of the QD DFBs under 2.5 Gbps modulation is characterized. The above-threshold behavior of the linewidth enhancement factor in QDs is studied, in contrast to the below-threshold ones in most of the published data to-date. The strong dependence of the linewidth enhancement factor on the photon density is explained by the enhancement of gain compression by the gain saturation with the carrier density, which is related to the inhomogeneous broadening and spectral hole burning in QDs.

# TABLE OF CONTENTS

Chapter One. Introduction .....	1
1.1. Properties of QDs: expectation and reality .....	1
1.2. Current status of selected quantum dot devices .....	4
1.3. Carrier dynamics in QDs .....	9
1.4. Motivation for this dissertation .....	16
1.5. Structure and basic performance of QD DFBs .....	18
Chapter Two. High speed performance of QD DFBs .....	25
2.1. Introduction .....	25
2.2. Experimental setup .....	27
2.3. Modulation bandwidth and its limiting factors: K-factor, effective carrier transport time and gain compression .....	28
2.4. Temperature effects on the modulation-bandwidth of QD DFBs .....	34
2.5. Conclusion .....	36
Chapter Three. Linewidth of QD DFBs .....	38
3.1. Introduction .....	38
3.2. Devices and experimental setup .....	39
3.3. QDs for narrow linewidth operation .....	43
3.4. Linewidth re-broadening in QD DFBs: gain compression .....	45
3.5. Effects of gain offset on the linewidth rebroadening .....	47
3.6. Conclusion .....	48
Chapter Four. QD DFBs under external feedback .....	52
4.1. Introduction .....	52
4.2. Experimental setup .....	57
4.3. Spectrum stability under external feedback: OSA spectrum and linewidth .....	58
4.4. DC Noise of QD DFBs under external feedback .....	64
4.5. Degradations of signal to noise ratio and jitter under external feedback .....	64

Chapter Five. Chirp of QD DFBs .....	67
5.1. Introduction .....	67
5.2. Time-resolved chirp: Experimental setup and technical background.....	71
5.3. Chirp with a fixed extinction ratio of modulation.....	74
5.4. Chirp with a fixed modulation depth $V_{pp}$ .....	82
Chapter Six. Conclusions and suggestions for future work .....	89
Appendix A. Gain compression and gain saturation in QD lasers .....	93
Appendix B. Non-degenerate four-wave mixing in quantum dot distributed feedback lasers.....	98
Appendix C. Matlab code for the threshold and yield calculations of DFBs .....	104
Appendix D. High Gain Quantum Dot Semiconductor Optical Amplifier for 1300 nm.....	108

## LIST OF FIGURES

Fig. 1.1 Ideal density of states for charge carriers in structures with different dimensionalities [10].	2
Fig. 1.2 Atomic force micrograph image of the InAs DWELL active region showing an average $1.3 \times 10^{11} \text{ cm}^{-2}$ single-layer dot density.	21
Fig. 1.3 A typical QWELL laser structure. 2.4 ML of InAs is deposited into a 10nm width InGaAs well for dot formation. The quantum dot and well are grown at 590 °C while the other layers at 610 °C. For multi-stack structures, GaAs spacers of 10-40nm width are deposited between the QWELL layers. Data and figure is from Ref. [13]	21
Fig. 1.4 The structure of a typical QD DFB.	22
Fig. 1.5 A typical optical spectrum of QD DFBs.	23
Fig. 1.6 LIV curves of a QD DFB shows a threshold of 3mA, a slope efficiency about 17% and a turn-on voltage of 1.1 V.	23
Fig. 1.7 Temperature performance of a QD DFB with a gain offset about -8.4 nm [55].	24
Fig. 1.8 The LI characteristics at various temperatures for a DFB laser with a gain-offset of 8.5nm [55].	24
Fig. 2.1 Experimental setup for high speed measurement.	28
Fig. 2.2 Small signal responses of QD DFBs with their curve fitting based on Eqn. (2.1).	30
Fig. 2.3 The resonance frequencies and damping factors from the curve fitting results of Fig 2.2.	30
Fig. 2.4 Optical spectrum of the quantum dot DFB at 40mA. The amplitude of the excited states is roughly equal to that of the side-mode of the DFB.	31



Fig. 2.5 Optical spectrum of the quantum dot DFB at 55mA pump. As a comparison to Fig. 2.4, lasing at excited states can be observed and the three-rate-equation model is not applicable anymore. ....	31
Fig. 2.6 Curve-fitting based on Eqn. (2.3) shows that gain compression output power $P_{\text{sat}}$ is $3.7\pm 0.4$ mW. ....	32
Fig. 2.7 Curve fitting based on Eqn. (2.2) to derive the K factor and effective carrier lifetime of the QD DFB. ....	32
Fig. 2.8 The carrier transport time as a function of the pump current derived from the small signal modulation response of the QD DFB. The error bar increases dramatically after the excited states lasing for a pump larger than 55mA. ....	33
Fig. 2.9 Effective carrier transport times, resonance frequencies and damping rates of QD DFBs under constant junction temperature. ....	37
Fig. 2.10 Curve-fitting of the squares of the resonance frequency to the pump current in the QD DFB with fixed junction temperature. Gain compression is found to become significant at a pump current of about 12-18mA, corresponding to 2.5-3.5 mW. ....	37
Fig. 3.1 (a), (b) and (c) are the spectra of device A, B and C at 10 mA, respectively. (d) is the spectrum of the commercial QW DFB at 10 mA. ....	40
Fig. 3.2 The experimental setup for the self-homodyne linewidth measurement of QD DFBs. ....	41
Fig. 3.3 The self-homodyne spectra and their Lorentzian curve-fittings of QD DFB device B at different pump levels. ....	42
Fig. 3.4 The self-homodyne spectra and their Lorentzian curve-fittings of the commercial 1.3 $\mu\text{m}$ QW DFB. ....	42
Fig. 3.5 Linewidths and SMSRs of the three QD DFBs as a function of optical output power. ....	49
Fig. 3.6 Linewidth and SMSR of a commercial 1.3 $\mu\text{m}$ QW DFB. ....	49

Fig. 3.7 The figure of merit for the spectral linewidth enhancement in semiconductor lasers $n_{sp}(1+\alpha^2)$ at optical gain peak as a function of the modal gain in bulk DH, QW lasers with different number of quantum wells [101] and QD lasers with six stacks of DWELL.....	50
Fig. 3.8 Schematic plot for applying an optical filter to exclude the excited-state ASE from the self-homodyne measurement. ....	51
Fig. 3.9 The measured linewidths of the QD DFB device <i>C</i> with different bandwidth of the optical filter. The linewidths are found to be independent of the filter bandwidth. ....	51
Fig. 4.1 Coherence collapse of a DFB laser is indicated by the dramatic broadening of the linewidth [102]. ....	53
Fig. 4.2 The low frequency noise of a DFB under external feedback with different linewidth enhancement factors. Noise burst after coherence collapse is shown [102]. The $\alpha$ in the figure stands for linewidth enhancement factor. ....	53
Fig. 4.3 A schematic presentation of the effects of external feedback on a semiconductor laser. ....	55
Fig. 4.4 Schematics of the experimental setup. The 2.5 Gbps pattern generator was used only for the eye-diagram measurement. ....	58
Fig. 4.5 The optical spectra of the QD LLC DFB with -14 dB and less than -60 dB external feedback. No significant broadening is observed with the resolution of the optical spectrum analyzer to be 0.06nm. ....	60
Fig. 4.6 Spectra of the commercial QW DFB with -15 dB and less than -60 dB external feedback. Significant broadening is observed. ....	60
Fig. 4.7 Self-homodyne spectra of the QD DFB under different external feedback strength, while linewidth re-broadening occurs at -14dB. ....	61
Fig. 4.8 Self-homodyne spectra of the commercial QW DFB under external feedback strength, the linewidth re-broadening at -20dB external feedback can be clearly observed. ....	61

Fig. 4.9 The noise spectrum of the QD LLC DFB before coherence collapse. Low frequency noise is the dominant component of the spectrum. ....	62
Fig. 4.10 The noise spectrum of the QD LLC DFB at coherence collapse. The spikes at integer multiples of the relaxation frequency in the noise spectrum are the indications of the coherence collapse. ....	62
Fig. 4.11 The noise spectra of the QD LLC DFB and the QW DFB under coherence collapse introduced by external feedback. QD LLC DFB shows a lower noise level compared to the commercial QW DFB. ....	63
Fig. 4.12. The eye-diagram of the QD DFB under 2.5 Gbps modulation with different external feedback levels. ....	66
Fig. 4.13. The root-of-mean-square jitter and signal-to-noise ratio (SNR) of the QD LLC DFB and QW DFB under different external feedback ratios. Although the degradation of the jitter is more same for the two devices, the SNR of the QD DFB starts to degrade under -30dB external feedback, about 20 dB improvement compared to the QW DFB. ....	66
Fig. 5.1 The experimental setup for TRC measurement [116]. The QD DFB is modulated by the pattern generator and its wavelength chirping is translated into optical intensity variation and then recorded by the DCA. ....	72
Fig. 5.2 A schematic drawing of the measurement of the wavelength chirping with the optical filter built in to the OSA [116]. ....	72
Fig. 5.3 LIV curves of the QD DFB for the TRC measurement. ....	75
Fig. 5.4 The eye diagram of the output of the modulated QD DFB biased at 20 mA with an extinction ratio of 9.5 dB. ....	76
Fig. 5.5 The chirp and corresponding power measured on the QD DFB biased at 20 mA. The chirp at '0' levels are noisier than '1' levels as a result of the increased measurement error for lower power. ....	78
Fig. 5.6 TRC measurements of the chirp and power of a QW DFB as given in ref. [121]. ....	78

Fig. 5.7 The average chirp and the peak-to-peak modulation voltage under different DC biases of the QD DFBs with the extinction ratio kept around 10 dB.....	80
Fig. 5.8 The shift between the center frequencies of the modulated and un-modulated output from the QD DFB as a function of current with the extinction ratio fixed at ~ 10 dB.....	80
Fig. 5.9 The measured effective alpha and its dependence on the output power of the QD DFB under modulation with the extinction ratio fixed at ~ 10 dB. ....	81
Fig. 5.10 The measured and curve-fitted chirps of the QD DFB under 15 mA, 20 mA and 35 mA DC biases with a peak-to-peak modulation voltage fixed at 250mV.....	85
Fig. 5.11 The effective alpha and its dependence on the output power measured in the QD DFB. ....	86
Fig. 5.12 The gain compression coefficients at different DC output powers of the QD DFB.....	86
Fig. 5.13 The distortion of the gain spectrum of QD gain media due to the inhomogeneous broadening and spectral hole burning effects. ....	87
Fig. 5.14 The overall profile of QW homogeneously-broadened gain spectrum is clamped and kept unchanged even under a strong gain compression.....	87
Fig. 5.15 The threshold gain of the QD DFB from the curve-fitting of the chirp measured at different biases. ....	88
Fig. 5.16 The average chirp of the QD DFB with a fixed $V_{pp}=0.25V$ under different DC current biases.....	88

## **LIST OF TABLES**

Table 1-1. A review of some experiments on the carrier dynamics in QDs. ....	13
Table 2-1. The variation of DFB wavelength under different pumps is controlled to be less than 0.01nm, indicating a small change of the junction temperature.....	35
Table 3-1. The performance of QD DFB <i>A</i> , <i>B</i> and <i>C</i> and the commercial QW DFB at room temperature. ....	40
Table 3-2 Estimating the figure of merit for narrow linewidth in QD DFBs .....	44

# Chapter One. INTRODUCTION

## *1.1. Properties of QDs: expectation and reality*

It is very natural for quantum dots (QD) to become attractive after the success of quantum well (QW) hetero-structures. The development of quantum well devices confirms the functionality of the quantum confinement of carriers in semiconductors and fosters the concepts and tools which are essential to design, fabricate and characterize QD devices. Theoretically, QD lasers represent an ultimate case of the application of the size quantization concept to semiconductor hetero-structure lasers [1].

The advantages of quantum dots compared to quantum wells stems from their unique density of states resulted from the 3-dimensional confinement of carriers. As shown in Fig.1.1, the energy levels of quantum dots are less convolved with each other. After the creation of the first QD lasers in 1993 and early 1994 [2,3], various potential advantages of QDs have been verified on actual devices, including the low transparency current [4], increased material and differential gain [5], less temperature sensitivity [6] and reduced linewidth enhancement factor ( $\alpha$  parameter) [7]. Furthermore, QDs can extend the achievable wavelengths on given substrates since the three dimensional structure of the nanometer dots helps to relax the strain from the lattice mismatch while minimizing dislocation formation. One of the real applications of this is the growth of 1.3  $\mu\text{m}$  InAs QD lasers on GaAs substrates. Finally, as QDs are spatially separated and the carriers are localized once they get captured into the dots, QD gain media are more resistant to defects than QW structures [8,9].

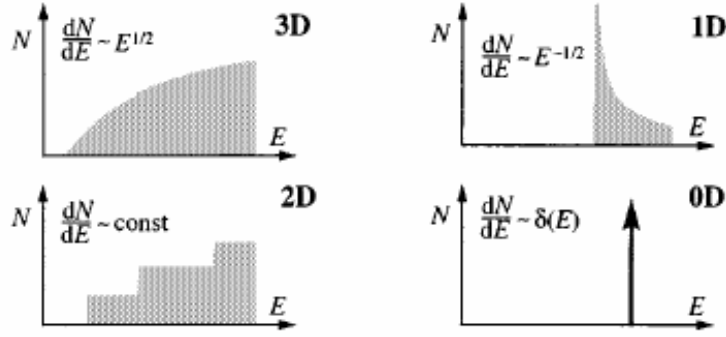


Fig. 1.1 Ideal density of states for charge carriers in structures with different dimensionalities [10].

However, quantum dots in the real world are not identical to the ideal ones people based their predictions on. The energy barrier for carrier confinement is not finite in QDs, first of all, indicating an imperfect confinement and the impact of continuum or unbound states. The size and shape dispersion of QDs, which broaden the carrier distribution in  $k$ -space, still seems insurmountable for the growth technology nowadays. Due to the large effective mass of holes, the energy separation of holes in the strained dots is less than the thermal energy of the typical temperature of operation. Carrier dynamics are very different in QDs, compared to QWs, due to the insufficiency of the optical phonons with the right energy to facilitate the carrier relaxation between energy states. All of those realities compromise the advantages of QDs mentioned previously.

### ***1.1.1. Gain and loss in QD media***

Very low threshold current densities ( $26 \text{ A cm}^{-2}$  in 3 stacks of dots-in-a-well (DWELL)), very low internal losses ( $\sim 0.5\text{-}1.5 \text{ cm}^{-1}$ ) are found in QD lasers [4]. In a quantum dot laser emitting at  $1.16 \mu\text{m}$ , with an internal quantum efficiency of 98%, its transparency current was measured to be  $6 \text{ A/cm}^2$  per quantum dot layer [11], compared to  $50 \text{ A/cm}^2$  in typical QWs [12]. The maximum modal gain of the ground state is

measured to be  $2.4 \text{ cm}^{-1}$ ,  $3.6 \text{ cm}^{-1}$  and  $5.7 \text{ cm}^{-1}$  for a single sheet of InAs/In<sub>0.1</sub>Ga<sub>0.9</sub>As (dot density  $4 \times 10^{10} \text{ cm}^{-2}$ ), InAs/In<sub>0.15</sub>Ga<sub>0.85</sub>As (dot density  $3.2 \times 10^{10} \text{ cm}^{-2}$ ) and InAs/In<sub>0.2</sub>Ga<sub>0.8</sub>As (dot density  $3.7 \times 10^{10} \text{ cm}^{-2}$ ), respectively [13]. Although different groups reported quite similar values of the gain, the published values of the differential gain in QDs are very scattered, varying from  $2 \times 10^{-12}$  [14],  $1.7 \times 10^{-14}$  [15] to  $3.1 \times 10^{-16} \text{ cm}^2$  [16], due in part to the lack of agreement on the confinement factor which is related to the shape of quantum dots and cannot be measured accurately. Since the limited number of available states in QDs, gain will saturate, and thus the corresponding differential gain will decrease rapidly as the carrier density approaches the dot density.

### ***1.1.2. Temperature insensitivity***

Though QD lasers demonstrated high characteristic temperature ( $>300\text{K}$ ) in a temperature range below 150-180 K [17],  $T_0$  was reported to be 120K, not much superior compared to commercial GaAs-based QW devices, near room temperature [18]. Ideally, the  $T_0$  value should be infinite, but the non-ideal DOS of QDs prevents this [19]. In practice it is found to vary depending on the particular size, shape, and number of electron and hole levels [20]. The key points for achieving improved high-temperature operation were proposed to be large volume density, deep potential and high quantum efficiency [21]. The  $T_0$  could also be artificially higher from the undesirable non-radiative recombination processes in the dots or the optical confinement layer [22]. P-type modulation doping was used to compensate for the closely spaced hole levels in QDs and showed a  $T_0$  of about 200 K between 0 to 80 °C [19].



### ***1.1.3. Linewidth enhancement factor***

Typically linewidth enhancement factors are measured using the Hakki-Paoli technique which requires a delicate control of the temperature of testing. The published results range from negative to about 2 [23,24]. 0.1 is reported by Newell [7] in single stack of QDs and a minimum of about 1.0 is measured by Ukhanov [16]. It is found that the excited states and the continuum state in the QWs have severe effects on the alpha factor of the ground state [25]. In tunneling-injection QD devices, alpha is measured to 0.15 [26] and 0.7 [15,27]. As one of its drawbacks, the Hakki-Paoli method is applicable only under threshold and in F-P lasers. As we know, there is still no systematic study about the alpha factor in a real QD laser operating above threshold. Gain compression can make the alpha strongly dependent on the photon density. The above-threshold alpha and gain compression effects will be investigated in this dissertation.

## ***1.2. Current status of selected quantum dot devices***

### ***1.2.1. QD Amplifiers: high saturation gain, low noise, high speed, pattern effect free, XGM, XPM and four wave mixing.***

QD semiconductor optical amplifiers (SOAs) are among the best successful applications of QDs and have been exposed to a thorough investigation. It is instructive to review the QD SOA research to help understand some of the results described for DFB lasers later in this dissertation. Although QDs have a smaller modal gain than QWs due to a smaller physical volume, or smaller confinement factor, a longer waveguide can generally result in more available gain as long as the gain is not significantly saturated. Therefore, the most fundamental issue in a SOA is the gain saturation power which sets a limit on the maximum extractable power out of the SOA [28]. The physics of this gain saturation here

is due to the competition between the carrier recombination time and the stimulated emission time, as a result of the steady state solution of rate equations. It is notable here that this gain saturation is different from the gain compression effect resultant from the competition between the carrier equilibrium time and the stimulated emission time as indicated by the steady state solution of master equations. Since the gain saturation power is inversely proportional to the differential gain, which gets saturated much easier in QDs than QWs, it is expected that QDs will have a very high gain saturation power [29,30]. Experimentally, a gain-saturation power over 20 dBm is achieved in QD SOAs [31]. High amplification (>18 dB) of 200-fs pulses was achieved in a quantum-dot (QD) semiconductor amplifier over a spectral range exceeding 100nm without pulse distortion [32]. The noise of an SOA is from the spontaneous emissions and the figure of merit is the noise figure, defined as the degradation of the input and output signal to noise ratio. It is well known that the noise figure is proportional to the population inversion factor,  $n_{sp}$ , which is believed to be smaller in QDs due to the abrupt density of states [30]. A noise figure of 5 dB is demonstrated in QD SOAs [33]. One of the most significant features of QD SOAs is the high-speed performance. In typical bulk or QW SOAs, the whole gain spectrum is typically within the gain homogeneous broadening width. Therefore, the carriers will respond as a whole unit and carrier recombination lifetime will determine the high-speed performance. In QDs, however, the homogenous broadening is found to be narrower than the inhomogeneous one and significant spectral hole burning can be observed. In this case, only the carriers within the narrower homogeneous broadening respond as a whole unit and the carriers outside of this homogeneous broadening act as a reservoir [34,35]. This physical phenomenon has relevance to the operation of QD lasers

as well and will be discussed later in the thesis. For the QD SOA, the outcome is that the carrier dynamics are determined by the carrier equilibrium time (1~10 ps), instead of the carrier recombination time (~1 ns). In this sense, QDs are much faster gain media than QWs. Experimentally, people have shown that the pattern effect is much weaker in QD SOAs than QW SOAs [36-39]. This ultrafast response is also proven in cross gain modulation due to the same carrier dynamics [40-42]. No experiments about cross phase modulation have been reported by now in QDs.

Four wave mixing has been studied by different groups in quantum dot amplifiers [36,41,43-46]. FWM is a well-established technique to characterize the carrier dynamics. The efficiency of FWM in QDs, which is proportional to  $\chi^{(3)}/g$  ( $g$  is gain) in QDs is found comparable to QWs, not enhanced by the three-dimensional confinement as theoretically predicted [47], probably due to the non-ideal features of the QD medium. Appendix 2 discusses in the FWM in QD DFB lasers.

### ***1.2.2. FP lasers: High power and filamentation free***

Besides the low threshold, high efficiency and temperature insensitivity mentioned previously, high power is demonstrated in QD devices. GaAs-based QD-lasers emitting at 1.3  $\mu\text{m}$  exhibit output power of 5 W and single transverse mode operation up to 300mW. An output power of 5 W has been obtained in 1.5  $\mu\text{m}$  QD lasers. Furthermore, single-mode lasers at 1.16  $\mu\text{m}$  and 1.3  $\mu\text{m}$  show no beam filamentation and a reduced  $M^2$ , which is believed to be related to the low linewidth enhancement factor [48].

### ***1.2.3. External cavity tunable lasers: wide tunable range and low threshold***

A grating-coupled external-cavity quantum dot laser is tuned across a 201 nm range around 1200 nm at a maximum bias of  $2.87 \text{ kA/cm}^2$ , one order of magnitude less than the bias required for comparable tuning of quantum well lasers [49]. Tuning range from 1.095 to 1.245  $\mu\text{m}$ , extended from the energy levels of the ground state to excited states, is achieved in QD external tunable lasers with a threshold density less than  $1.1 \text{ kA/cm}^2$  at any wavelength. This large tunable range and low threshold are the product of the rapid carrier filling of the higher energy states under a low pumping current and homogeneous broadening in the QD ensemble [50].

### ***1.2.4. QD Mode-locked lasers: ps pulse generation***

Intuitively, the broad spectrum in QD gain media indicates a narrow pulse from QD mode-locked lasers. The low spontaneous emission noise as discussed in previous sections also suggests low amplitude and frequency noise in QD pulse sources. More importantly, the absorption in quantum dots is more easily saturated than in QWs. Passive mode locking was achieved at 1.3  $\mu\text{m}$  in oxide-confined, two-section, bistable quantum dot (QD) lasers with an integrated intra-cavity QD saturable absorber [51]. One of the sections is forward biased to provide gain, while the other one reversed biased as a saturable absorber. Fully mode-locked pulses at a repetition rate of 7.4 GHz with a pulsewidth of 17 ps were observed without self-pulsation.

***1.2.5. Distributed feedback lasers (DFB): Threshold, efficiency, SMSR, temperature performance, high speed performances, linewidth, feedback resistance and chirp***

Single mode lasers with sufficient output power are fundamental building blocks for optical communication systems. InAs/GaAs QD DFBs are fabricated mainly with a loss-coupled grating deposited laterally to the ridge waveguide. No index-coupled InAs/GaAs QD DFBs are reported by now. In 1999 Kamp [52] et. al. reported complex coupled distributed feedback lasers at 980nm based on a single layer of InGaAs/GaAs self-organized quantum dots grown by molecular beam epitaxy. A threshold current of 14 mA, differential efficiency of 0.33 W/A and a side-mode suppression ratio (SMSR) of > 50 dB have been obtained in these devices. Single mode operation was observed for temperatures from 20 to 213 °C. In 2001, Klopff achieved single-mode operation of 1.3  $\mu\text{m}$  InAs/GaInAs QD DFBs with a SMSR of up to 55dB, threshold currents as low as 17mA and CW output powers of up to 8mW at room temperature [53]. The InAs/GaAs QD DFBs studied in this dissertation are provided by Zia Laser, InC. More than 5 GHz small-signal modulation bandwidth was observed in these first devices indicating the potential for high-speed operation of quantum dot lasers [54,55]. The linewidth-power product of the QD DFBs is measured to be 1.2 MHz-mW, one order of magnitude lower than the typical value of QW DFBs [56]. The same QD devices shows an improvement of external feedback resistance: 8 dB on the critical coherence collapse feedback level and 20 dB in term of signal-to-noise degradation [57]. These devices will be discussed in detail in this dissertation.

### *1.3. Carrier dynamics in QDs*

It has been controversial for a long time whether QDs are a fast or slow gain media. This is a fundamental question for applications such as high-speed light sources, high-speed amplifiers, all-optical gates and switches using QDs. It was proposed that the carrier relaxation between different levels could be hindered due to the lack of phonons with the large energy corresponding to the level spacing in QDs, the so called “phonon bottleneck” [58-63]. The phonon bottleneck is observed in quantum dots occupied with just one electron without a hole, and without a population in the wetting layer [64]. Meanwhile, recent proposals invoke fast mechanisms other than the phonon-assisted process in QDs, such as, electron-hole scattering [65], Auger process [66,67], phonon spectrum broadening by the QD itself [68], and support fast carrier dynamics in QDs.

The carrier dynamics is characterized by three parameters: dephasing time, electron relaxation time and hole relaxation time. The dephasing time,  $T_2$ , is basically the time scale within which the carrier is coherent to itself. Since  $T_2$  is inversely proportional to the homogenous linewidth, it can be the intrinsic limit of the  $\delta$ -function of the DOS in QDs. The electron and hole relaxation times (measured as recovery times in pump-probe experiments),  $\tau_e$  and  $\tau_h$ , are the time constants for electrons and holes to reach their intra-band equilibrium. Measurements of carrier dynamics have been carried out on QD materials from different groups as listed in Table.1. The results vary broadly due to the structural difference of the QD samples.  $T_2$  was measured to be about 150 fs ( $\sim 9$  nm homogeneous broadening width) in 1.25  $\mu\text{m}$  MOCVD-grown QDs under normal operating conditions of lasers at room temperature [69]. This result is consistent with the spectral width 13 nm (10.5 meV) of homogeneous broadening derived from the gain

behavior of the 1.23  $\mu\text{m}$  DWELL tunable laser built at CHTM with an external cavity [70]. Since  $T_2$  in QWs is about 30-50 fs for the intra-band transitions [71], it suggests that the width of homogeneous broadening of QDs will be about 3 times narrower than that of QWs. The explanation could be that once the carriers get relaxed into the QDs, they are localized and the energy barrier reduces their chance to be scattered by phonons and carriers, a similar mechanism underlying the fact that the excitonic transition generally has a longer dephasing time than the intra-band one [71].

For the carrier relaxation or capture time in the QDs, Table.1 shows that the carrier-carrier scattering provides a fast intradot relaxation on the order of 0.1-1 ps [47,69,72,73] while the carrier capture from the surrounding QWs into QDs by phonon scattering takes about 1-10 ps [33,47,69,73,74]. The phonon bottleneck with a time constant of 950 ps is observed only at low temperature ( $< 40\text{ K}$ ) and low pump level (less than one e-h pair per dot) [64]. From the loss recovery pump-probe experiments, the escape time constant of the holes in QDs is measured to be 1.25 ps, faster than the 5.9 ps of the electrons [72]. The recombination lifetime of the carriers in QDs are found to be 140 ps [33], 660 ps [69] and 900 ps [74]. The carrier heating is found not to be severe in the only study of its kind, resulting from the low total carrier density in 1.0  $\mu\text{m}$  QDs even under gain saturation [75]. The data given in Table 1.1 are quite scattered due to the differences between the material, structure, barrier height and measurement technique of the experiments. The details of those experiments are given in Table. 1.1.

As a conclusion, the phonon bottleneck is not present in the devices under room temperature or high pump, which is the case of most interest for semiconductor lasers. However, even though the carrier-carrier scattering can improve part of the capture time,

the carrier dynamics in QDs is relatively slow compared to QWs due to the 1 – 10 ps phonon-scattering relaxation time. The slow carrier dynamics (1 – 10 ps) is confirmed by the performance of the QD optical amplifiers [76]. On the other hand, since the  $T_2$  is large in QDs, a narrow homogeneous broadening is observed in QDs. The combination of those time constants indicates a strong gain compression effect, considering the gain saturation power  $P_s$  is given as [77]

$$P_s = \frac{\hbar^2 \epsilon_0 n_g^2}{|\mu|^2 E_p (\tau_e + \tau_h) T_2} \quad (1.1)$$

$$g = \frac{g_0}{1 + P/P_s}$$

where  $\hbar$  is the Planck's constant,  $\epsilon_0$  is the permittivity of vacuum,  $n_g$  is the group index,  $|\mu|$  is the dipole moment,  $E_p$  is the photon energy,  $P$  is the optical power,  $\tau_e$ ,  $\tau_h$  and  $T_2$  are the intraband relaxation times for electrons, holes, and phase, respectively.

Another consequence of the slower dephasing time  $T_2$  in QDs is the spectral hole burning [70,75,78], which makes the dynamics of the carriers much different from QWs. Since homogeneous broadening dominates the gain spectrum of QWs and all the carriers react to external modulation homogeneously, the characteristic time constant will be the recombination lifetime which is typically 1 ns but experiment is more in line with diffusion limited gain recovery, even though the intra band relaxation is in the order of 100 fs. In the case of QDs, the characteristic time constant will be the gain recovery time of the spectral hole burning which is in the order of 1-10 ps. Therefore, QDs can be much **faster** than QWs as demonstrated in the QD SOAs in ref. [79,80].



The strong gain compression and spectral hole burning also introduces interesting behavior in the linewidth enhancement factor. The gain compression itself can increase the effective alpha by

$$\alpha_{eff} = \alpha_0(1 + P/P_s) \quad (1.2)$$

At the same time, since the gain at the lasing wavelength is clamped in a laser above threshold, the spectrum hole burning will result in an increase of the carrier density on the energy levels outside of the spectrum hole burned around the lasing wavelength, especially the excited states, which in turn further increases the alpha factor [81]. This effect becomes more severe if the ground state gain is close to being saturated with the carrier density. Investigating these effects in QD DFB lasers is one of the major subjects of this dissertation.

Table 1-1. A review of some experiments on the carrier dynamics in QDs.

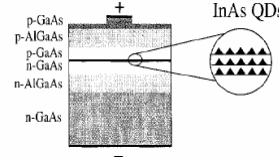
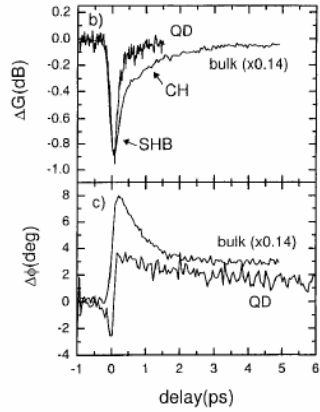
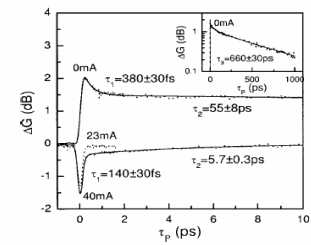
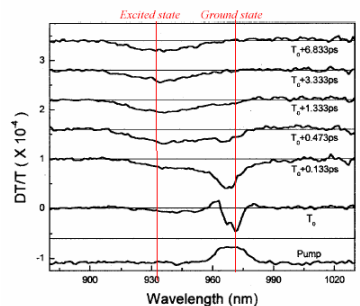
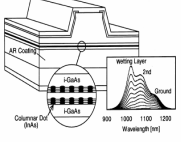
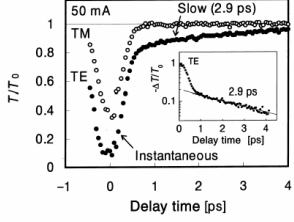
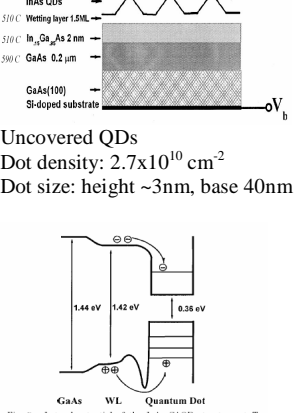
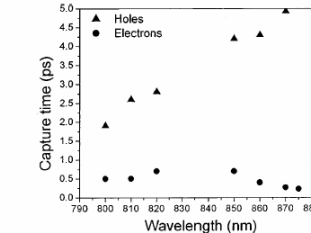
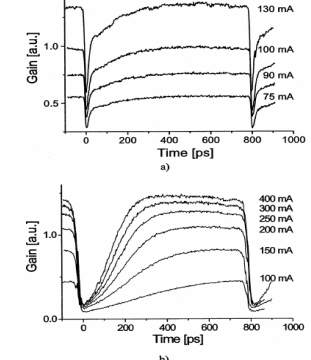
Author	Year	Sample and device	Techniques	Major results
D. Gammon [71]	1995	GaAs bulk, GaAs/Al <sub>0.3</sub> Ga <sub>0.7</sub> As (20nm) QW		T <sub>2</sub> : Exciton transition: 190fs in QW, 270fs in bulk Intraband: (30-70)fs (carrier scattering)
P. Borri , D. Bimberg [82]	1999	MOCVD pin InAs/InGaAs (1.08μm) 21nm GaAs spacer 120nm GaAs Al <sub>0.7</sub> Ga <sub>0.3</sub> As cladding Waveguide: 8μ×400μm (tilted)	1.08μm 140fs fourier transform limit pulse 300KHz repetition rate	Dephasing time (Room Temp.) T <sub>2</sub> :  290±80fs (SHB) (~10nm homogenous width) 260±20fs (FWM) <70fs for high pump (carrier-carrier scattering)
P. Borri, D. Bimberg [72]	2000	MOCVD pin InAs/InGaAs (1.08μm) 21nm GaAs spacer 120nm GaAs Al <sub>0.7</sub> Ga <sub>0.3</sub> As cladding Waveguide: 8μ×475μm (tilted)	1.08μm 140fs fourier transform limit pulse 13nm spectral width 300KHz repetition rate	Room Temp. 0mA (absorption): 1.25ps (h), 5.9ps (e) (escape time) 4mA: transparent 10mA: ground state saturates 20mA: ground state gain recovery: 115±10fs (SHB) (comparable to QW) Carrier heating: 2ps recovery time
P. Borri, D. Bimberg [75]	2001	InGaAsP/InP bulk SOA (1.53μm) Waveguide: 3x250 μm. (tilted)  Same QD structure as the last one. 	1.08μm pump probe  OPA pumped by Ti:S Tunable 0.9-2.5 μm 150 fs pulse 300KHz repetition rate	  Room temperature SHB: spectrum hole burning CH: carrier heating  CH is much less severe in QDs due to the reduced free carrier absorption resulted from the lower total carrier density in QDs even under gain saturation.
P. Borri , D. Bimberg [69]	2001	InAs/InGaAs pin (1.25 μm) InAs in 5nm In <sub>0.13</sub> Ga <sub>0.87</sub> As QW 3 stacks 30nm Be-doped GaAs spacer AlGaAs cladding Waveguide: 5μm x 1000 μm (tilted) Ground state lasing threshold 150A/cm <sup>2</sup> in 525 x 625 μm Lase at excited state for narrower waveguide Transparency current: 23mA Large confinement energy	1.25 μm Fourier limit 130fs 76MHz repetition rate (for improved SNR with balanced detector) pump: 0.2pJ probe: 1/30 pump	  Room temperature: 0mA (loss recovery): 0.38 ± 0.03 ps: escape to excited state

FIG. 2. Pump-induced gain change vs pump-probe delay time at different bias current as indicated. Solid lines are fits to the data, and the corresponding time constants are indicated. In the inset, an expansion up to 1 ns of the measured dynamics without bias current is shown.

				<p>55 ± 8 ps : escape to the wetting layer</p> <p>0.66 ns : recombination lifetime</p> <p>T<sub>2</sub> : 220 ± 10 fs</p> <p>40mA (gain recovery):</p> <p>0.14 ± 0.03 ps: carrier-carrier scattering</p> <p>(faster than undoped GaAs spacer)</p> <p>5.7 ± 0.3 ps: phonon-assisted relaxation</p> <p>T<sub>2</sub> : 150 ± 10 fs</p>
K. Kim, P. Bhattacharya [73]	2002	<p>MBE In<sub>0.4</sub>Ga<sub>0.6</sub>As (QD 975nm)</p> <p>Four stacks</p> <p>2.5nm GaAs barrier</p> <p>100nm GaAs wetting layer</p> <p>500nm AlGaAs carrier confiment grown at 520°C, other 620°C</p> <p>dot size: height 7nm, base 14nm</p> <p>dot density: 5 × 10<sup>10</sup> cm<sup>-2</sup></p> <p>MBE InAs (QD 1000nm)</p> <p>2nm GaAs barrier</p> <p>Five stacks</p>	<p>85fs</p> <p>3.5μJ</p> <p>250KHz</p> <p>pump: 10nm bandwidth filter of the Ti: Sapphire white light source</p> <p>14ps delay with respect to the gain pulse</p> <p>Optically injection by 800nm gain pulse</p>	 <p>FIG. 2. DTR spectra measured with a 970 nm pump and a broadband white-light probe in In<sub>0.4</sub>Ga<sub>0.6</sub>As QDs versus probe delay (pump pulse at approximately t = T<sub>p</sub>, gain pulse at t = T<sub>p</sub> - 14 ps).</p> <p>Measurement T=8-15K Slightly higher at room temp.</p> <p>Burn a hole in ground state first, after ~130ps hole in excited state occurs and get localized</p> <p>In<sub>0.4</sub>Ga<sub>0.6</sub>As: 0.13ps intradot carrier-carrier scattering 1ps carrier capture into dot</p> <p>InAs 0.18ps intradot carrier-carrier scattering 1.8ps carrier capture into dot</p> <p>Less than one pair per dot: 5.2ps for electrons 0.6ps for holes</p>
J. Urayama, P. Bhattacharya [64]	2001	<p>MBE In<sub>0.4</sub>Ga<sub>0.6</sub>As (QD 975nm)</p> <p>Same as the last one</p>	<p>100fs 250KHz</p> <p>10nm filtering</p>	<p>T= 40KHz</p> <p>pump with less than one e-h pair per dot.</p> <p>For excited state: Relax to ground state τ<sub>21</sub>=7ps Capture from barrier: geminate 2.5 ps Nongeminate 8.5 ps Bottleneck time constant: 750ps</p> <p>For ground state: Capture from barrier: geminate 30ps Nongeminate 100ps</p>

<p>T. Akiyama Fujisu [78]</p>	<p>2001</p>	 <p>Fig. 1. Device structure and schematic of an InAs QD optical amplifier. The injection current was set at 5.0, ..., and 90 mA, respectively, from the bottom.</p> <p>InAs QDs 1150nm</p>	<p>Pump-probe Four-wave-mixing</p>	 <p>At 50mA Gain saturates at ground state Intra-dot carrier relax: 90fs Phonon scattering: 260fs Capture from wetting layer: 2ps</p> <p>Gain recovery 97% with 4ps, no slow component (&gt;50 ps in QWs) observed.</p>
<p>D. A. Yarotski CHTM [74]</p>	<p>2002</p>	 <p>Uncovered QDs Dot density: <math>2.7 \times 10^{10} \text{ cm}^{-2}</math> Dot size: height ~3nm, base 40nm</p> <p>Fig. 5. Lateral potential of the InAs SAQD structure at <math>T = 300 \text{ K}</math>. Close to the edges of the QD, a barrier is present for holes due to the strong influence of the strain on the hole system.<sup>16</sup></p>	<p>Ultrafast STM Pump-probe Resolution: 0.2ps Time solved THz spectroscopy</p>	 <p>Fig. 3. Dependence of the capture time on the pump-probe wavelength, obtained by fitting the curves presented in Fig. 2(b).</p> <p>Room Temperature Auger capture from wetting layer: 1-2ps Lifetime in WL: 350ps Lifetime in GaAs: 2.3ns Lifetime in QDs: 900ps</p>
<p>Z. Bakonyi CHTM [33]</p>	<p>2003</p>	<p>1300nm InAs/InGaAs DWELL Amplifier MBE 001GaAs 6 stacks Dot density: <math>1.3 \times 10^{11} \text{ cm}^{-2}</math> per sheet Waveguide: <math>4 \mu\text{m} \times 2.4 \text{ mm}</math> (tilted)</p>	<p>Pump: 1.25GHz 12ps 1300nm Probe: 1.25GHz- 125Hz 1.5ps 1296nm</p>	 <p>Fig. 7. Gain recovery dynamics (a) for the QD-SOA and (b) for a common MQW-SOA for different currents. Shift of curves corresponds to the change of the small-signal gain. The pump pulse duration is: (a) 12 ps and (b) ~20 ps. The input pump pulse energy: (a) ~40 fJ and (b) ~300 fJ.</p> <p>fast component: ~ 10 ps slow component: ~140 ps Not dependent on gain saturation and gain compression</p>

#### ***1.4. Motivation for this dissertation***

As shown in previous reviews, much research has been done in QD devices. However, the dynamic properties of the QD DFBs have not been systematically studied, including the high-speed performance, linewidth, external feedback effects and wavelength chirping. The advantage of QD DFB, compared to QD FP lasers, is the single mode operation that makes the photon-carrier interaction better fitted to the standard rate equations and easier to study. From the physics point of view, the motivation of this dissertation is to investigate the effects of the increasing optical power on the basic parameters of the devices. For example, as the linewidth enhancement factor (or alpha parameter) is measured mostly under threshold, it is important to understand how the alpha factor behaves above threshold. Gain compression, which is expected to be strong in QD devices as discussed in Section 1.2, will also be characterized in this dissertation by the dynamics of QD DFBs.

The remaining part of this chapter will be a general discussion of the fabricated QD DFBs, including their material design, light-current (LI) curves, optical spectrum, and temperature performance.

Chapter 2 will be devoted to the high speed performance of QD DFBs. The modulation bandwidth, bandwidth saturation, limiting factors and gain compression effects are investigated in QD DFBs.

Chapter 3 will focus on the static linewidth issue in QD DFBs. Narrow linewidth is demonstrated, while the linewidth re-broadening is observed at low photon density, suggesting a strong gain compression. The effect of gain offset, defined as the spectral distance between the DFB lasing mode and the peak of ground state gain, is presented.

Suggestions for narrow linewidth QD devices are given after analyzing the experimental data.

Chapter 4 will present the experiments investigating the external feedback resistance of QD DFBs by studies on the effects of external feedback on optical spectra, LI curves, CW linewidth, CW intensity noise, and the signal-to-noise ratio (SNR) and jitter under 2.5 Gbps modulation. A significant improvement in the external feedback will be demonstrated with a discussion about the factors determining the external feedback resistance.

Chapter 5 will investigate the frequency chirp of the QD DFBs under large-signal modulation, simulating the operation condition in a real communication system. Time-resolved chirp measurement is carried out and the experimental result will be discussed. The wavelength chirping of the QD DFB under external modulation will be measured. The dependence of alpha parameter on the photon density in the devices will be characterized and the gain compression coefficient will be determined.

The last chapter will summarize this dissertation and make some suggestion for future work on QD devices.

In Appendix one, the effects of the gain saturation with the carrier density on the dynamic properties of QD DFBs will be modeled, include the limitation on the modulation bandwidth and the dependence of alpha parameter on the output power of the QD devices.

In Appendix two, the four wave mixing effects in QD DFBs will be discussed. Wavelength conversion is demonstrated with an efficiency from -15dB to -30dB for a spectral detuning from 0.33nm to 8nm. The cavity resonance effect is also characterized.

## ***1.5. Structure and basic performance of QD DFBs***

### ***1.5.1. fabrication***

The DWELL laser structure is grown by solid source molecular beam epitaxy on a (001) GaAs substrate using conditions similar to those published previously [83]. The DWELL structure has led to a single layer dot density of  $1.3$  to  $2.4 \times 10^{11} \text{ cm}^{-2}$ , as shown in Fig. 1.3. These values are about 5-10 times higher than what has typically been achieved in the past for InAs/GaAs QDs emitting in this wavelength range. A multi-stack DWELL structure with aggregate dot density of  $\sim 8 \times 10^{11} \text{ cm}^{-2}$  was used in most of the QD DFBs studied here. Room temperature photoluminescence (PL) measurements show a ground state peak varying from 1295-1325 nm with a typical spectral FWHM of 89 nm.

The structure of the devices is presented in Fig. 1.4. [13]. The details of MBE growth and functionalities of each epi-layer can be found in ref. [83]. Device fabrication begins with the formation of 3 to 3.5  $\mu\text{m}$  ridges, followed by the e-beam lithographic patterning and liftoff of the lateral absorptive metal grating to form laterally-loss-coupled (LLC) DFB laser diodes. The period of the first order grating is roughly 200 nm. The LLC-DFB structure has the advantages of a gain-coupled device without requiring re-growth [84]. After surface planarization, Ti/Pt/Au is deposited for the p-type contact. Finally, a Au/Ge/Ni/Au n-type contact is deposited after the substrate has been polished. The wafer is cleaved into laser bars with cavity lengths of 300  $\mu\text{m}$  and the facets are asymmetrically HR/HR coated to lower the lasing threshold and get the output dominantly out of one facet. The layout of a typical QD DFB is given in Fig. 1.5.

### ***1.5.2. Optical spectra***

The DFB lasers emitted single-mode with SMSR of greater than 50 dB in a wavelength range from 1295-1328 nm, depending on the grating period. Fig. 1.6 shows the typical optical spectra of the QD DFBs. Although no pure stop band is observed, a side-mode about 4nm away presents might rise from the residual index-coupling of the metal grating. As the pump increases up to about 10-17 times of the threshold, depending on different devices, the excited states about 60 nm away from the ground state start to lase limiting the single-mode to this pumping level. This result indicates that the total carrier density is not clamped above threshold, which can be explained by the narrow width (~20 nm) of the homogeneous broadening and slow carrier relaxation time in QDs discussed in Chapter 1.

### ***1.5.3. LIV and temperature performance***

The typical threshold of QD LLC DFBs is less than 5mA with a slope efficiency of about 12-17%, while the FP lasers fabricated on the same wafer show a lower threshold and a slope efficiency about 25%. The turn-on voltage is 1.1 Volt. As shown in Fig. 1.7, the turn-on is not abrupt and further reduction or modified grading of junction barriers in the device will improve the carrier injection.

The detailed study of the temperature performance of those QD DFBs can be found in ref. [55]. The temperature shift of the DFB mode is 0.1 nm/K, determined by the thermal effect on the refractive index in GaAs-based materials. The gain peak of QDs is found to shift at a rate of 0.25 nm/K, compared to the value of 0.4 nm/K of QWs. Therefore, QD DFBs are shown to have a wider range of temperature operation [52]. The temperature performance of the DFBs depends on the sign and amplitude of the gain offset: whether



the gain peak is moving toward or away from the DFB mode. In a negative gain offset device (the DFB mode on the shorter wavelength side relative to the gain peak),  $T_0$  is found to be around 50K, while in a position gain offset, for a low pump level, threshold is independent of the ambient temperature as shown in Fig. 1.7 and Fig. 1.8.

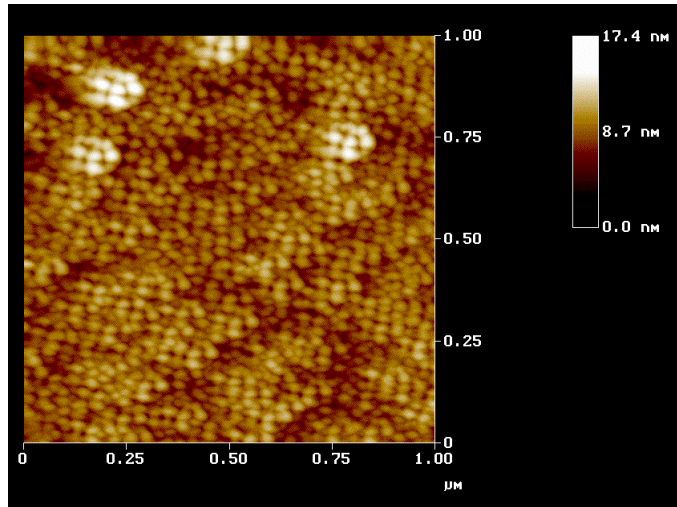


Fig. 1.2 Atomic force micrograph image of the InAs DWELL active region showing an average  $1.3 \times 10^{11} \text{ cm}^{-2}$  single-layer dot density.

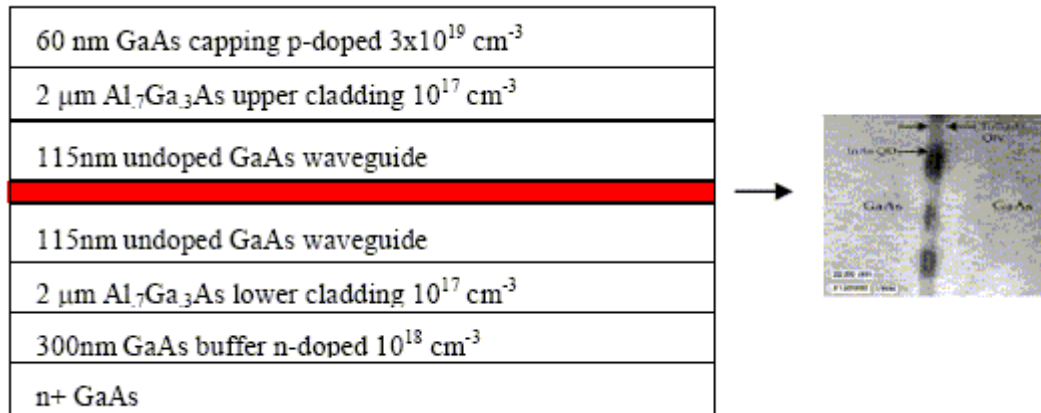


Fig. 1.3 A typical QWELL laser structure. 2.4 ML of InAs is deposited into a 10nm width InGaAs well for dot formation. The quantum dot and well are grown at  $590 \text{ }^\circ\text{C}$  while the other layers at  $610 \text{ }^\circ\text{C}$ . For multi-stack structures, GaAs spacers of 10-40nm width are deposited between the QWELL layers. Data and figure is from Ref. [13]

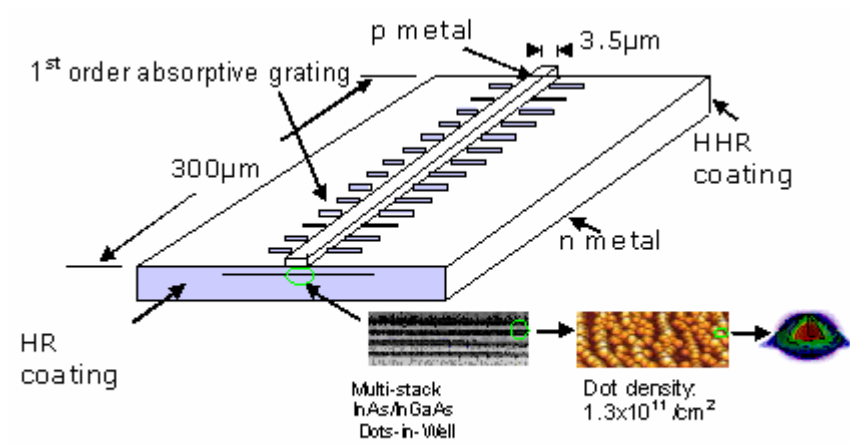


Fig. 1.4 The structure of a typical QD DFB.

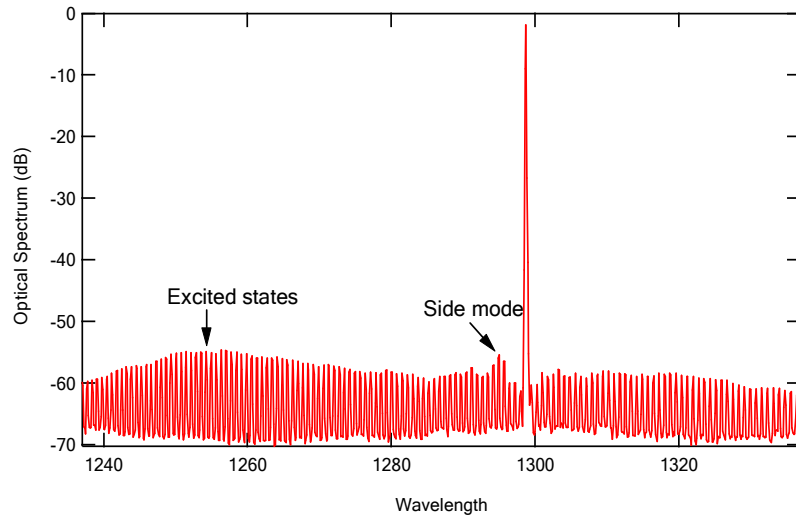


Fig. 1.5 A typical optical spectrum of QD DFBs.

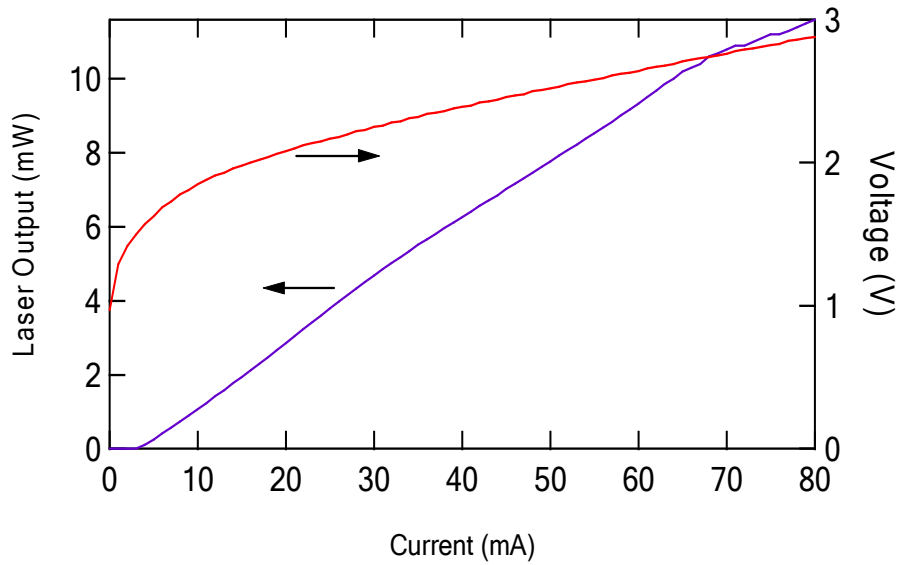


Fig. 1.6 LIV curves of a QD DFB shows a threshold of 3mA, a slope efficiency about 17% and a turn-on voltage of 1.1 V.

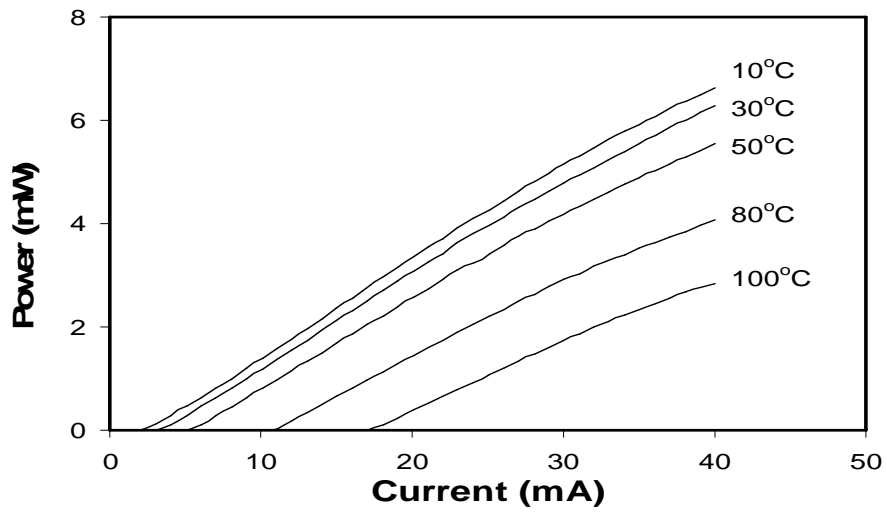


Fig. 1.7 Temperature performance of a QD DFB with a gain offset about -8.4 nm [55].

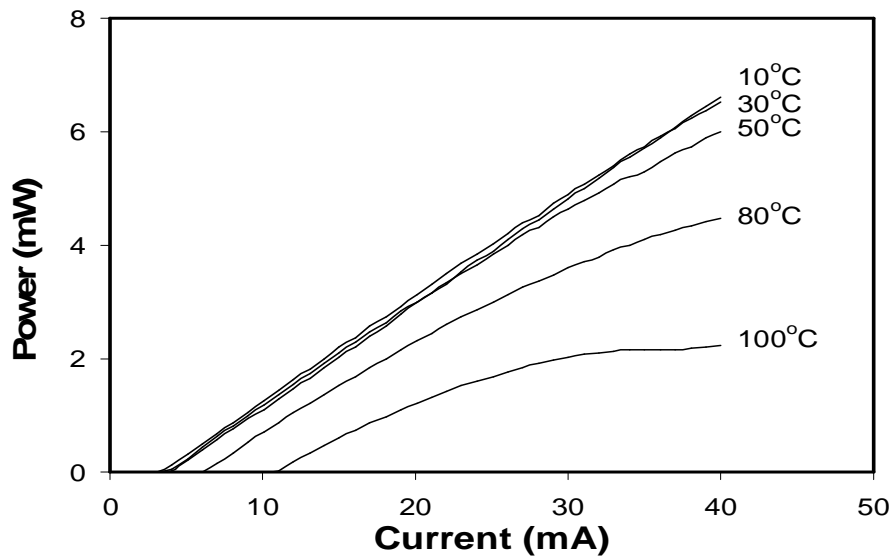


Fig. 1.8 The LI characteristics at various temperatures for a DFB laser with a gain-offset of 8.5nm [55].

## **Chapter Two. HIGH SPEED PERFORMANCE OF QD DFBs**

### ***2.1. Introduction***

High-speed semiconductor lasers are compact, reliable and inexpensive coherent sources for high-bit-rate optical communication systems. Among all the properties of high speed lasers, modulation bandwidth is the most important one. Efforts have been put on QD devices to improve the high speed performance, especially since the lasing wavelength of QDs on GaAs covers 1.3  $\mu\text{m}$ , the zero-dispersion window of commercial communication systems. By now, however, most of the high speed performance is measured in QD FPs [85,86]. The high speed performance of QD DFBs was reported very briefly in ref. [54] without giving physical analyses. A systematical study of the high speed performance of QD DFBs will be presented in this chapter.

The advantages of using QD DFBs, rather than FPs, to study high-speed properties are obvious. First of all, DFBs are more directly related to the real applications in communication systems. Secondly, the single mode of DFBs eliminates the effect of multimode dynamics of FPs, including mode hopping and mode competition under external modulation. Finally, since the DFB wavelength is associated with the junction temperature of the device, it can be fixed at a certain value by adjusting the heat sink temperature so that the thermal effects will be reduced and even eliminated in this high-speed measurement.

The high-speed performance of semiconductor lasers is typically characterized by their response to external small-signal modulation. Since the amplitude of the external modulation is small, the consequential optical response can be linearly tracked back to the driving force, that is, the modulation on the current injection. In dots-in-a-well QD structures, the carriers are injected into the QW first and then relax into the QDs. The slow relaxation corresponds to the slow carrier transport from the QW into the ‘active’ levels and can limit the high-speed performance as a parasitic RC constant. Based on this simplification, the dynamics of QD lasers can be described by a similar set of equations applied to SCH QW lasers considering the carrier transport from the SCH to QWs [87]. There are three rate equations in this model: one for the carriers directly involved in the lasing process, one for the carriers functioning as a reservoir outside of the lasing wavelength and another one for the photon density inside the laser cavity. By this model, the optical modulation response  $M(f)$  of a QD laser is given as [85]:

$$|M(f)|^2 \propto \frac{1}{((f_r^2 - f^2)^2 + \gamma^2 f^2)(1 + (2\pi f \tau_c)^2)} \quad (2.1)$$

The relationship between the resonance frequency  $f_r$  and the damping factor  $\gamma$  defines the  $K$ -factors as:

$$\gamma = Kf_r^2 + \frac{1}{\tau_{eff}} \quad (2.2)$$

$$\omega_R^2 \approx \frac{V_g(a_0/\chi)S}{\tau_p(1 + \epsilon_s S)} \quad (2.3)$$

$$g = \frac{g_0}{1 + \epsilon_s S} \equiv \frac{g_0}{1 + \epsilon_p P} \equiv \frac{g_0}{1 + \frac{P}{P_{sat}}} \equiv \frac{g_0}{1 + \frac{I - I_{th}}{I_{sat}}} \quad (2.4)$$

where  $\tau_c$  is the carrier transport time which includes capture,  $\tau_{eff}$  is the effective carrier lifetime,  $V_g$  is the group velocity,  $a_0$  the differential gain without gain compression,  $S$  the photon density,  $P$  is the output power measured at the facet of the device,  $I$  the pump current,  $I_{th}$  is the threshold current,  $\tau_p$  is the photon lifetime,  $\chi=1+\tau_{esc}/\tau_c$  is the modification factor due to the carrier transport with  $\tau_c$  the carrier capture time and  $\tau_{esc}$  the carrier escape time,  $\epsilon_s$  and  $\epsilon_p$  are the gain compression coefficients related to photon density and output power respectively. The introduction of  $P_{sat}$  and  $I_{sat}$  is for the convenience to estimate at what output power or DC pump current the gain compression becomes significant. The gain compression factor,  $\epsilon_s$ , can be calculated using Eqn. (2.3) if  $\omega_R$  and  $S$  can be experimentally obtained. The  $K$  factor will give us the ultimate limit of the 3-dB modulation bandwidth, which is  $8.89/K$ . The carrier transport time,  $\tau_c$ , gives rise to the parasitic-like low frequency roll-off in Eqn. (2.1). The  $\tau_c$  must be extended to include various parasitic effects, such as the equivalent RC constants of the p-n junction and the measurement circuit, since they are indistinguishable from the transport effect.

## ***2.2. Experimental setup***

The experimental setup is presented in Fig.2.1. The high-speed performance was measured using a HP8722D network analyzer and a New Focus 1014 detector with a bandwidth of 25GHz. An optical isolator is used to avoid external feedback into the device. The heat sink temperature is fixed during the first part of the measurements. In the second part of the experiment, as a comparison, the DFB wavelength is fixed to isolate the thermal effects inherent in the first part.



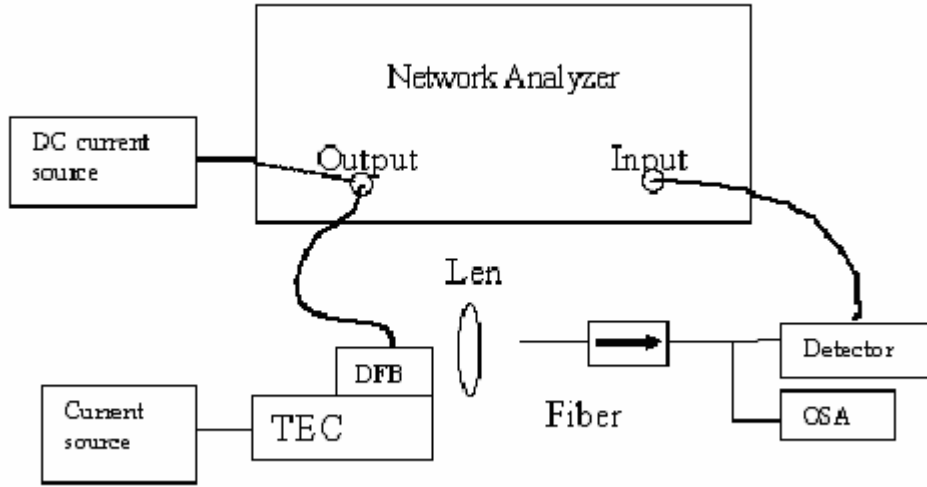


Fig. 2.1 Experimental setup for high speed measurement

### ***2.3. Modulation bandwidth and its limiting factors: K-factor, effective carrier transport time and gain compression***

Firstly we carry out the measurement with the heat sink temperature fixed at 20 °C. The responses under different DC biases are plotted in Fig. 2.2 with their curve-fitting based on Eqn. (2.1). The curve fittings are much better than the ones with the carrier transport time ignored (that is,  $\tau_c$  is fixed to be zero). The roll-off in the regime below 500 MHz arises from the detector itself rather than the QD DFB. As the pump current increases, the resonance frequency and damping factor saturate as shown in Fig. 2.3 and the 3-dB bandwidth is saturated at about 5 GHz until the excited states start lasing. This saturation can be attributed to the gain compression indicated by Eqn. (2.3), as long as the emission from the excited states is ignorable so that the three-rate-equation model still applies (without an additional equation for the excited state lasing). For the pump currents up to 40 mA, the amplitudes of the FP modes around the excited states are still not greater than those of the side modes near the DFB mode. Therefore, the three-rate-equation model

should apply up to at least 40 mA. The optical spectrum at 40 mA is shown in Fig. 2.4 compared to the case of excited-state lasing at 55 mA as illustrated in Fig. 2.5.

In Fig. 2.6, we curve-fit the square of the resonance frequency as a function of output power and find that the characteristic output power for gain compression,  $P_{sat}$ , is  $3.7 \pm 0.4$  mW. The definition of  $P_{sat}$  is given in Eqn. (2.4). With this value of the gain compression factor, the maximum resonance frequency is estimated to be 4.9 GHz. The curve fitting range can be extended up to 50 mA (still below the threshold of excited-state lasing) as shown in Fig. 2.6, confirming that the applicability of the rate equation model without considering the excited state lasing.

Given the facet reflectivity and modal volume of the DFB laser, we can calculate the gain compression coefficient,  $\epsilon_s$ , to be  $3\text{-}4 \times 10^{-16} \text{ cm}^3$ , which is more than 30 times higher than the typical value of QWs and is consistent with the value of  $4 \times 10^{-16} \text{ cm}^3$  measured by D. Bimberg et. al. in QD FPs with the same technique [86]. A modified nonlinear gain coefficient expression has been derived to explain this large enhancement of  $\epsilon_s$  in QD lasers. The novel theory is detailed in Appendix 1. The important result is

$$\epsilon_{s,eff} = \frac{g_{max}}{g_{max} - g_{th}} \epsilon_s \quad (2.5)$$

with  $g_{max}$  the maximum gain supplied by the QD active region,  $g_{th}$  the threshold gain and  $\epsilon_{s,eff}$  the effective gain compression factor. This enhancement is unique to QD lasers due to the abrupt gain saturation with carrier density. In these particular DFB lasers,  $g_{max}$  is estimated to be  $15 \text{ cm}^{-1}$  and  $g_{th}$  is about  $12 \text{ cm}^{-1}$ . This makes the enhancement factor  $g_{max}/(g_{max}-g_{th})$  about 5.

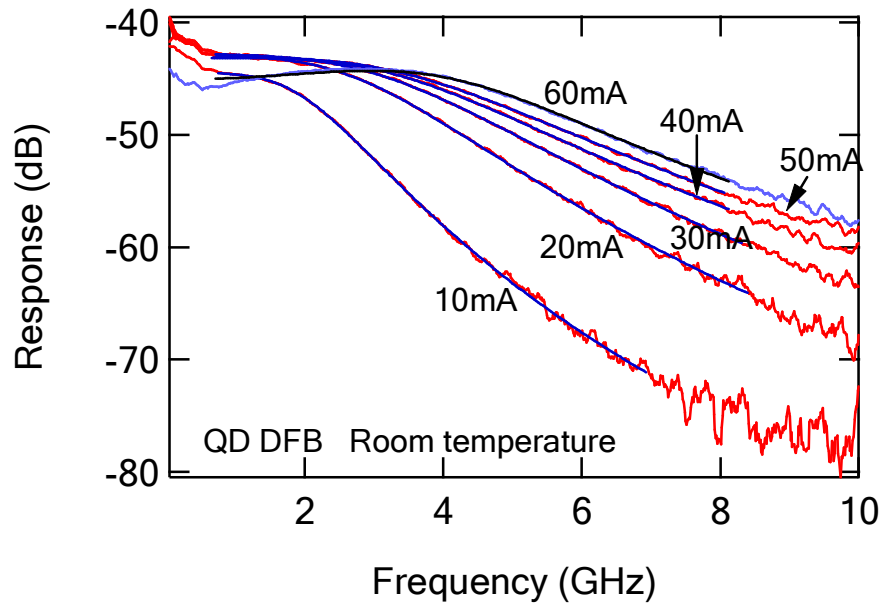


Fig. 2.2 Small signal responses of QD DFBs with their curve fitting based on Eqn. (2.1).

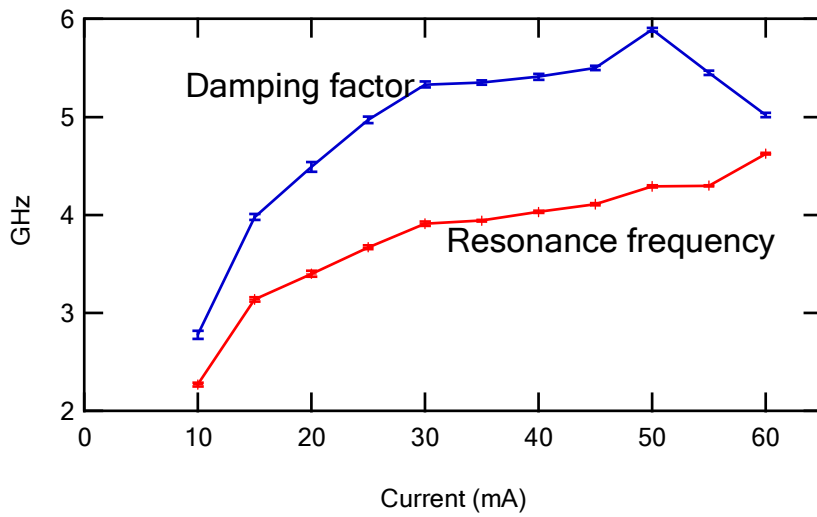


Fig. 2.3 The resonance frequencies and damping factors from the curve fitting results of Fig 2.2.

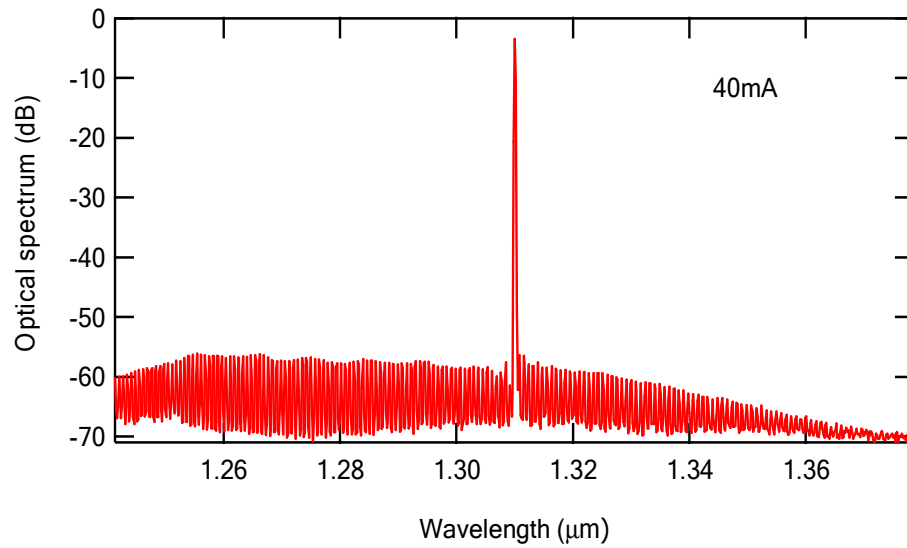


Fig. 2.4 Optical spectrum of the quantum dot DFB at 40mA. The amplitude of the excited states is roughly equal to that of the side-mode of the DFB.

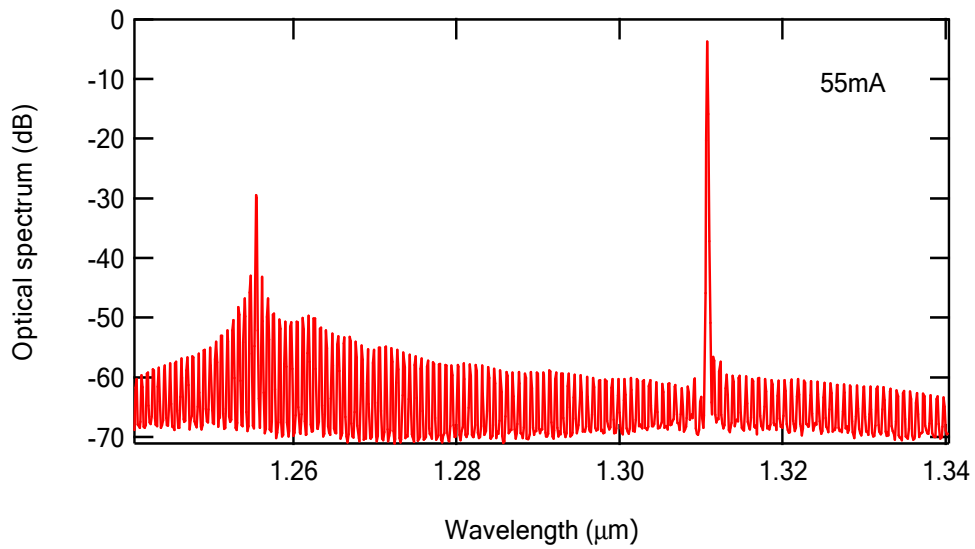


Fig. 2.5 Optical spectrum of the quantum dot DFB at 55mA pump. As a comparison to Fig. 2.4, lasing at excited states can be observed and the three-rate-equation model is not applicable anymore.

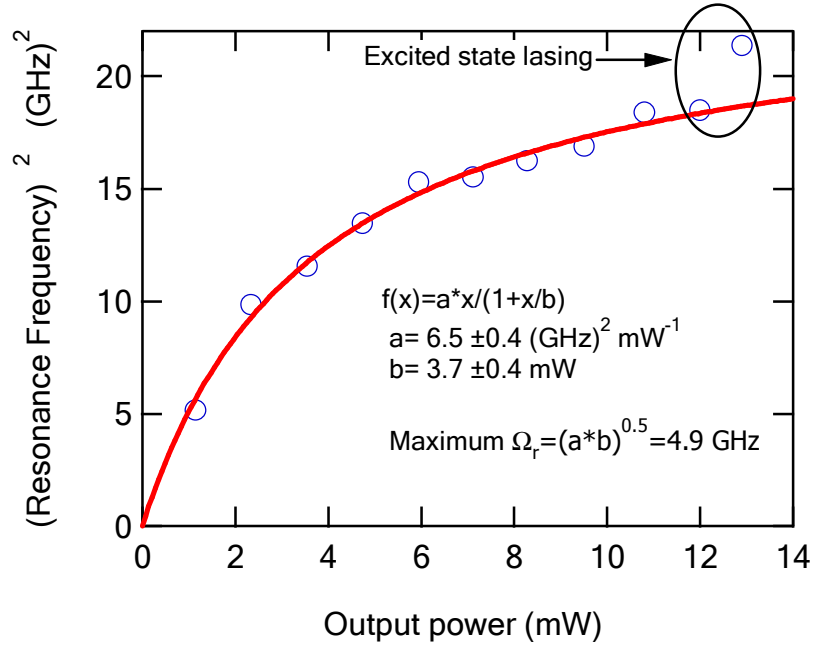


Fig. 2.6 Curve-fitting based on Eqn. (2.3) shows that gain compression output power  $P_{\text{sat}}$  is  $3.7 \pm 0.4 \text{ mW}$ .

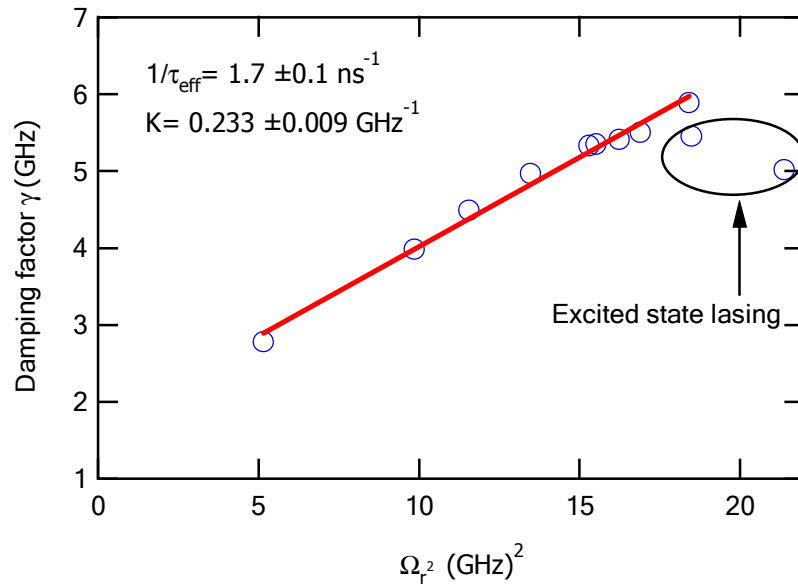


Fig. 2.7 Curve fitting based on Eqn. (2.2) to derive the K factor and effective carrier lifetime of the QD DFB.

The damping factor is plotted in Fig. 2.7 as a function of the square of resonance frequency. Curve fitting based on Eqn. 2.2 shows a  $K$  factor of  $0.23 \text{ GHz}^{-1}$  and an effective carrier lifetime of 590 ps. It is notable that the linearity can be extended to 50 mA pump, suggesting that the three-rate-equation model applies as long as no lasing occurs at the excited states. When the pump is greater than 55 mA, the excited-states start to lase, and the linear relation between the damping factor and resonance frequency fails. In these cases, an additional equation is required for the lasing mode at the excited states. The effective carrier lifetime,  $\tau_{eff}$ , is curve-fit to be 590 ps in the QDs, about half of the typical value in the QWs [87].

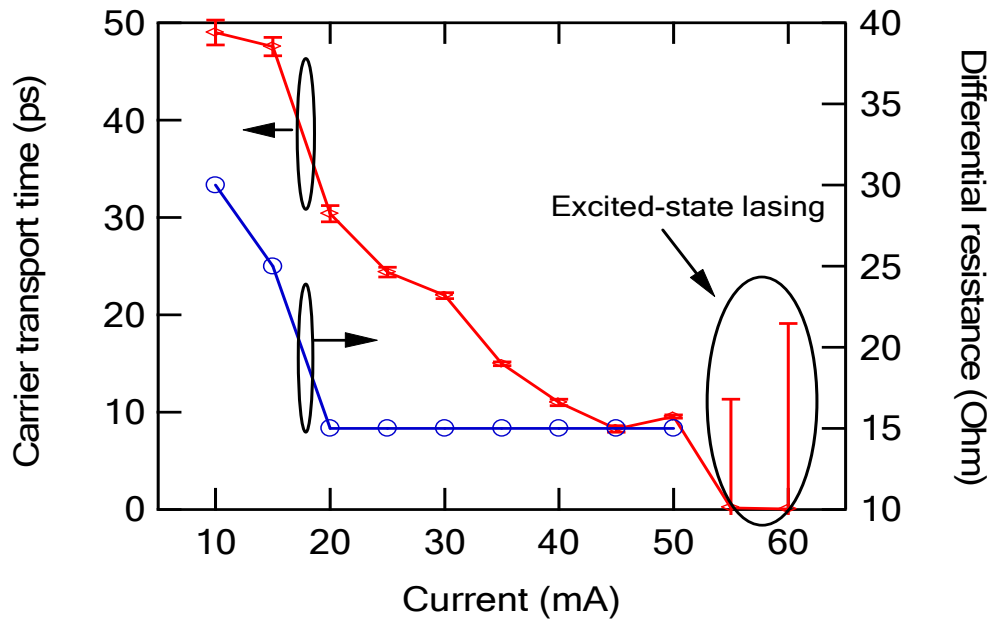


Fig. 2.8 The carrier transport time as a function of the pump current derived from the small signal modulation response of the QD DFB. The error bar increases dramatically after the excited states lasing for a pump larger than 55mA.

The carrier transport time,  $\tau_c$ , can also be determined from the curve fittings of the modulation responses. The monotonic decrease of the carrier transport time with the

increasing pump is demonstrated in Fig. 2.8 with the differential resistance derived from the I-V curve of the device. The drop of  $\tau_c$  below 20 mA could result from the decrease of the differential resistance and thus the RC parasitic time constant. However, for the pump current greater than 20mA, the decrease of the  $\tau_c$  is relatively much more compared to the change of the differential resistance, indicating a carrier-density dependent relaxation time constant. This is the first observance of this effect in the high-speed response of QD lasers and could be attributed to an Auger dominated carrier relaxation process [66,67]. At high pump levels, the carrier transport time reaches about 10ps and the corresponding parasitic bandwidth is 16 GHz. When the excite states start to lase, we can see a large error bar on the carrier transport time suggesting that the three-rate-equation model is inapplicable.

Since the maximum 3-dB bandwidth of  $K=0.23 \text{ (GHz)}^{-1}$  and  $\tau_c = 10 \text{ ps}$  correspond to 38 and 16 GHz, much larger than the 5-6 GHz maximum bandwidth actually measured in these QD DFBs, it can be concluded that the  $K$  factor and the carrier transport time are not the limiting factors. The most possible reasons are strong gain compression in the QD DFBs.

#### ***2.4. Temperature effects on the modulation-bandwidth of QD DFBs***

To make sure that the bandwidth saturation described in previous section is not due to thermal effects, the small signal modulation is measured with a fixed DFB wavelength by controlling the heat sink temperature. This will keep the junction temperature constant, since the DFB wavelength is directly associated with the refractive index which is sensitive to the junction temperature. Table 2.1 shows the corresponding heat sink

temperature and DFB wavelength under different DC pump levels. The DFB wavelength differs less than 0.01nm as we increase the pump current from 6mA to 40mA. The SMSR is still greater than 50dB in the DFB pumped at 40mA with a heat sink temperature of 6.7 °C.

Pump current (mA)	Heat Sink Temp. (°C)	DFB wavelength (nm)
6	20.2	1319.61
10	19	1319.62
15	17.3	1319.62
20	15.2	1319.61
25	13.4	1319.62
30	11.1	1319.61
35	9	1319.61
40	6.7	1319.61

Table 2-1. The variation of DFB wavelength under different pumps is controlled to be less than 0.01nm, indicating a small change of the junction temperature.

The resonance frequency and damping rate at a fixed DFB wavelength are presented in Fig. 2.9, showing a difference less than 10% from the case with fixed heat sink temperature as presented in Fig. 2.3. The effective carrier transport time at high pump is 10 ps, the same as the value without the DFB wavelength control. This indicates that carrier transport time at high pump is not sensitive to the junction-temperature change originating from the current injection. A curve fitting based on Eqn. (3.3) is shown in Fig. 2.11 and  $I_{sat}$  is found to be  $15 \pm 3$  mA with an effective threshold current about  $2.7 \pm 0.7$  mA. Since the variation of the slope efficiency with temperature can be ignored as indicated in Fig. 1.7 and Fig. 1.8, a gain-compression output power,  $P_{sat}$ , of 2.5 - 3.5 mW can be found corresponding to the  $15 \pm 3$  mA current. Compared to the 3.3 – 4.1 mW value determined without the junction-temperature control, we can conclude the thermal



effects do not significantly affect the gain compression coefficient measured in previous section.

## ***2.5. Conclusion***

In conclusion, the high-speed performance of QD DFBs is measured and the 3-dB modulation band width is found to saturate at about 5 GHz in the case of ground state single mode lasing. The curve-fittings of the small signal responses give the resonance frequency and damping factor under different pump levels, from which the gain compression coefficient is determined to be  $3-4 \times 10^{-16} \text{ cm}^3$  in QD DFBs. This strong gain compression makes the modulation bandwidth saturated at about 5 GHz. It is also found that neither the K factor nor the carrier transport time limits the modulation bandwidth of the QD DFBs. Finally, by fixing the DFB wavelength, the thermal effects from the junction temperature changing are also checked to have an ignorable impact on the gain compression coefficient determined by this high speed measurement. Therefore, reducing the gain compression effects is crucial to improve the high speed performance of QD devices. A new physical origin for the enhanced gain compression, abrupt gain saturation, has been proposed and quantified in these QD DFB lasers. Analytical expressions have been derived to explain the physical phenomenon making rapid and simple device characterization possible.

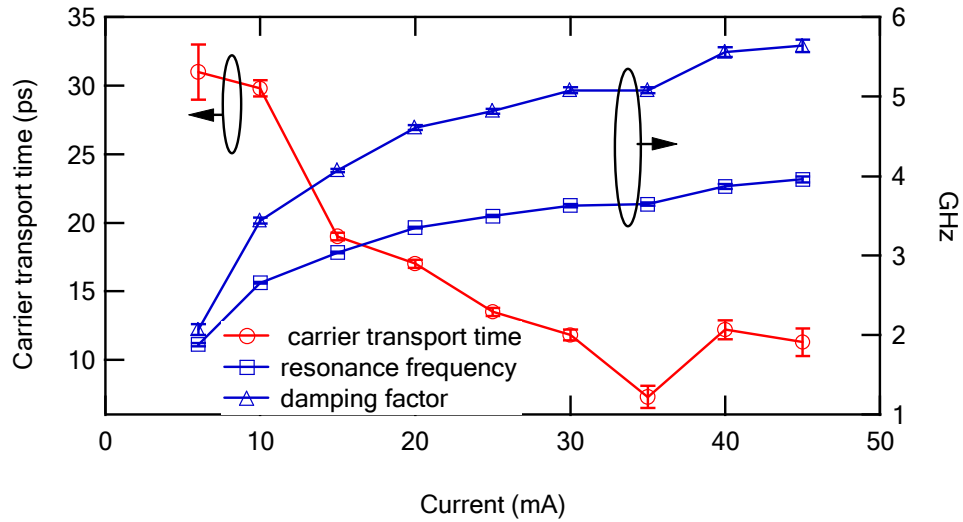


Fig. 2.9 Effective carrier transport times, resonance frequencies and damping rates of QD DFBs under constant junction temperature.

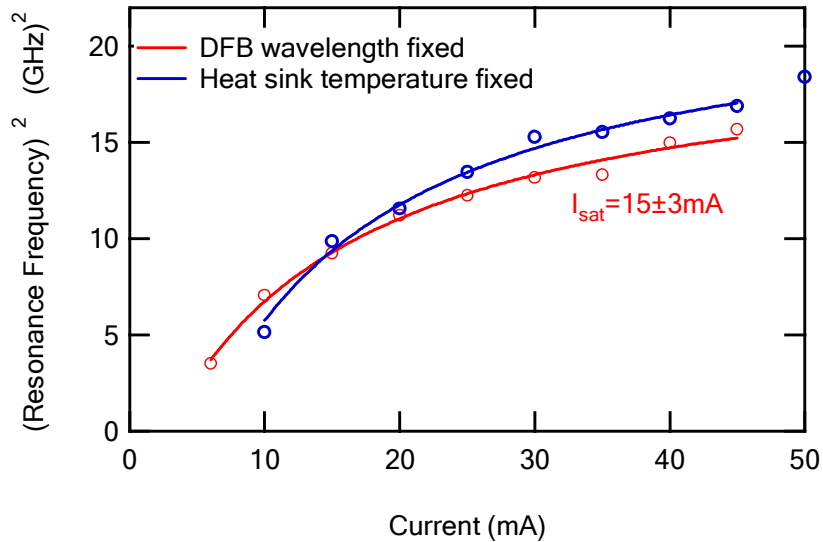


Fig. 2.10 Curve-fitting of the squares of the resonance frequency to the pump current in the QD DFB with fixed junction temperature. Gain compression is found to become significant at a pump current of about 12-18mA, corresponding to 2.5-3.5 mW.

## Chapter Three. LINEWIDTH OF QD DFBS

### *3.1. Introduction*

Since the invention of the first laser, the spectral purity of the lasing mode has always been one of the most central interests. Although typically gas- and solid-state lasers show a narrower linewidth than semiconductor lasers, the former are inferior when their cost, size and reliability are considered. Much research has been conducted on narrow linewidth semiconductor lasers. Different device designs, such as the external cavity configuration [88-90] and chirped grating DFBS [91,92], have been proposed to achieve narrow linewidth. Meanwhile, new semiconductor materials, for instance, strained QWs [93] and finally QDs, have been proposed for narrow linewidth operation because of their the low internal loss and small linewidth enhancement factor. Therefore, studies of the linewidth of QD lasers are important. In real world applications, single-mode distributed feedback (DFB) lasers at 1.3  $\mu\text{m}$  with narrow spectral linewidth are essential for various applications, such as coherent sources and local oscillators for communication systems [94].

As discussed in the previous chapter, 1.3  $\mu\text{m}$  devices based on InAs/InGaAs “dots-in-a-well” (DWELL) technology have become promising alternatives to lasers built on InP-based materials, due to their low substrate cost, excellent temperature performance, low threshold current and small linewidth enhancement factor. Theoretical calculations also show that the population inversion factor,  $n_{\text{sp}}$ , is lower in QDs than in QWs [30]. These advantages of QDs over QWs suggest that QD lasers can have narrow linewidth, considering

$$\Delta\nu = \frac{\Gamma g_{th} v_g^t \alpha_m h\nu}{4\pi P_0} n_{sp} (1 + \alpha^2) \quad (3.1)$$

where  $\Delta\nu$  is the linewidth,  $g_{th}$  is the threshold gain,  $P_0$  is the optical output power,  $\Gamma$  is the confinement factor,  $v_g$  is the group velocity,  $\alpha_m$  is the mirror loss, and  $h\nu$  is the photon density [87].

Theoretically, narrow linewidth is always obtained by increasing the laser power as indicated by Eqn. (3.1). In real cases, however, the minimum achievable linewidth is typically limited by the linewidth rebroadening or floor due to the mode instability [95], existence of side modes [96], spatial hole burning [91,97] and the gain compression [98,99]. The first three effects are mostly related to the device structure and can be minimized or eliminated by optimizing the device design. The gain compression is fundamentally related to the time scales for the carrier equilibrium dynamics in the semiconductor gain media and is enhanced in QD gain media. Therefore, to understand the pros and cons of QDs device for narrow linewidth is essential research that motivates the experiments described in this chapter.

### ***3.2. Devices and experimental setup***

The linewidth of three loss-coupled QD DFBs with different gain offsets and a commercial 1.3  $\mu\text{m}$  index-coupled QW DFB from Mitsubishi, Inc. are studied in this chapter. The gain offset is defined as the difference between the DFB wavelength and the gain-peak wavelength. The cavity length of the QD and QW DFBs is 300  $\mu\text{m}$ . The static

characteristics of those devices are presented in table 3.1. The optical spectra of at 10mA injection current are shown in Fig. 3.1. FP modes can be clearly observed in the loss-coupled QD DFBs, while a stop band is clearly observed in the index-coupled QW DFB.

Device #	A	B	C	QW DFB
$I_{th}$ (mA)	3	5	6	7.8
Slope efficiency $\eta$ (mW/mA)	0.16	0.20	0.12	0.2
$\lambda$ at 10 mA (nm)	1297	1309	1324	1305
Gain peak at 10 mA (nm)	1309	1309	1305	N.A
SMSR at 10 mA (dB)	57	48	41	44.6
SMSR at 45 mA (dB)	56	53	45	50

Table 3-1. The performance of QD DFB A, B and C and the commercial QW DFB at room temperature.

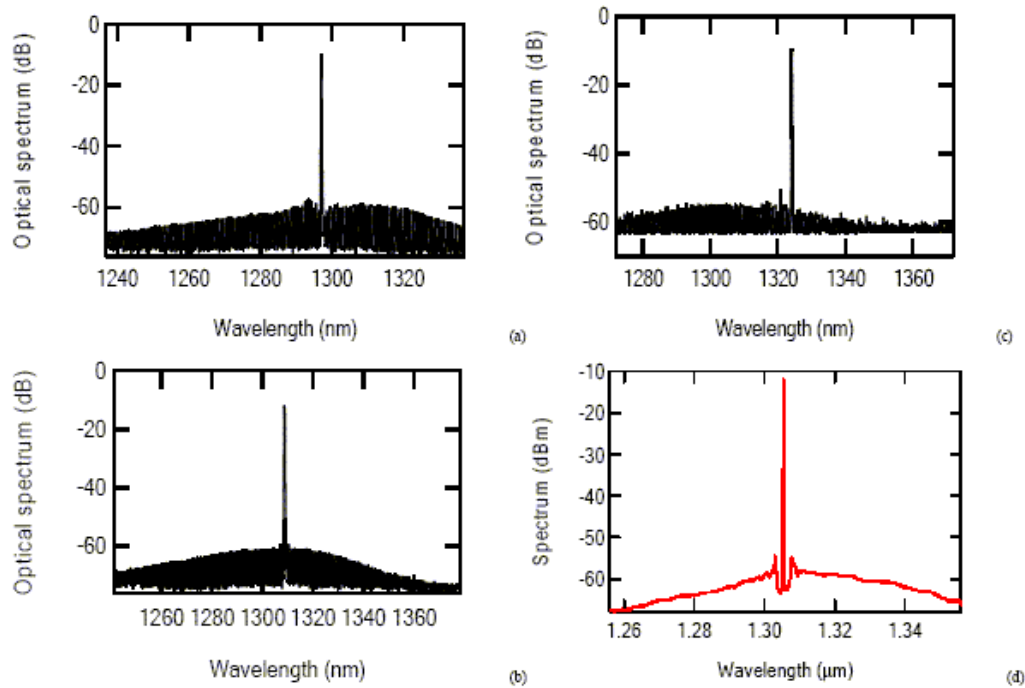


Fig. 3.1 (a), (b) and (c) are the spectra of device A, B and C at 10 mA, respectively. (d) is the spectrum of the commercial QW DFB at 10 mA.

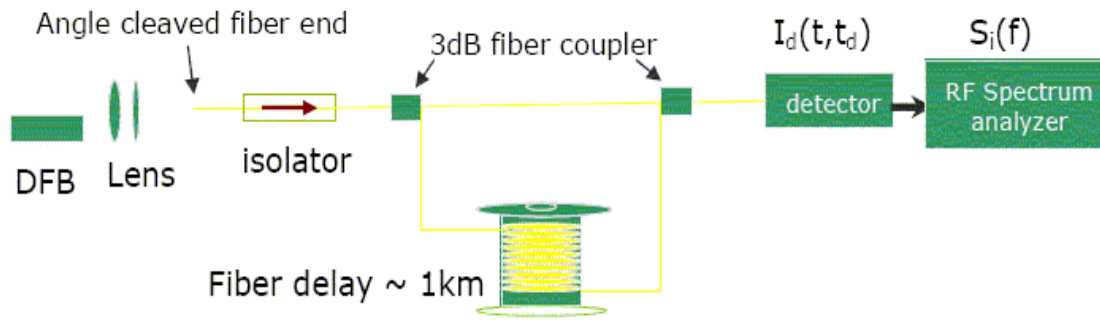


Fig. 3.2 The experimental setup for the self-homodyne linewidth measurement of QD DFBs.

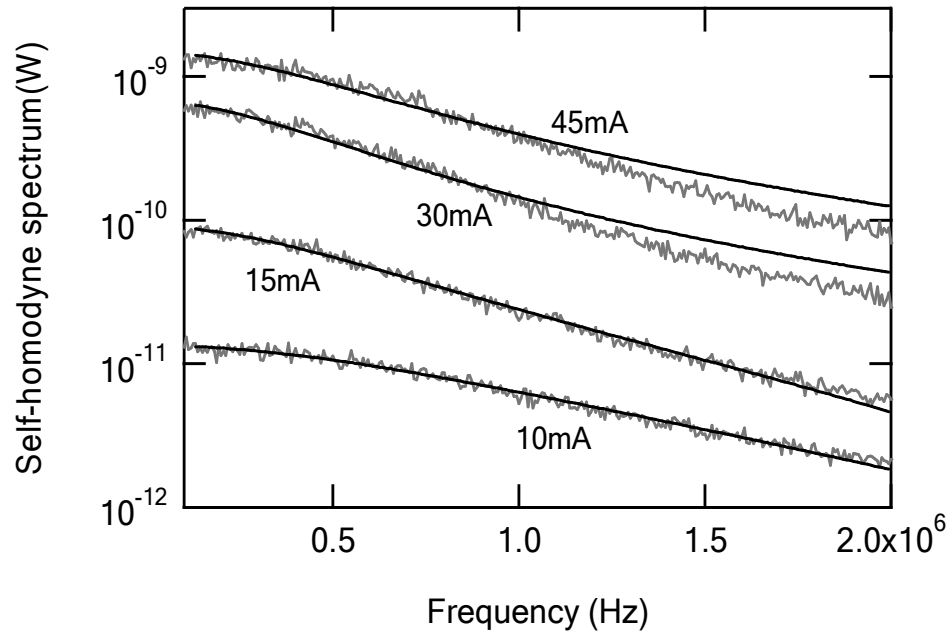


Fig. 3.3 The self-homodyne spectra and their Lorentzian curve-fittings of QD DFB device B at different pump levels.

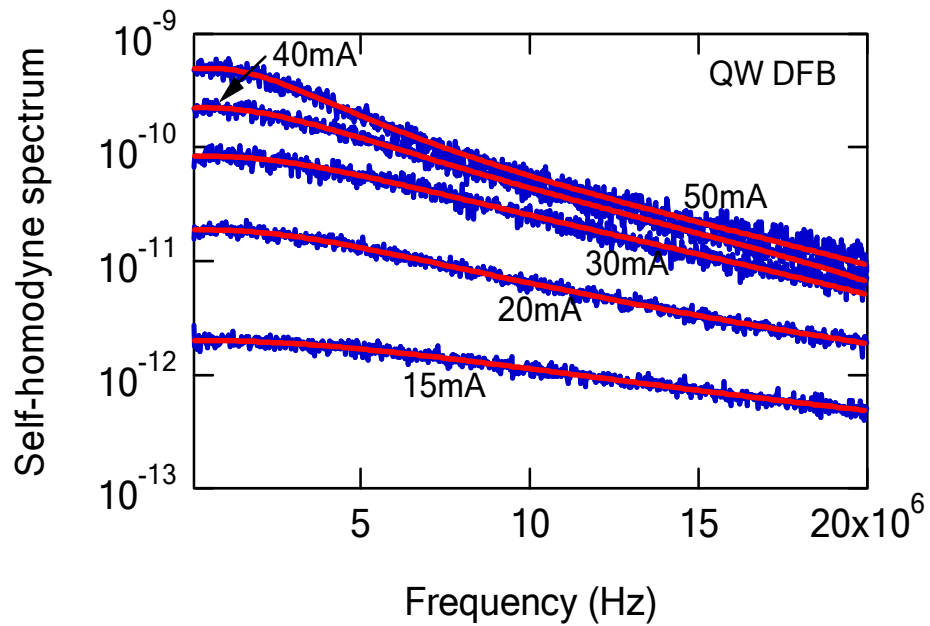


Fig. 3.4 The self-homodyne spectra and their Lorentzian curve-fittings of the commercial  $1.3 \mu\text{m}$  QW DFB.

The linewidth is measured with the self-homodyne technique [100] using a fiber interferometer with a 3.5  $\mu\text{s}$  delay. The experimental layout is shown in Fig. 3.2. An ILX lightwave LDP-3620 ultra-low-noise current source is used to avoid excess noise from the pump source. When a current source without noise control, ILX lightwave 3811, is used, the linewidth is measured to be 40 MHz, instead of the sub MHz when the low-noise current source is used. The heat-sink temperature is controlled to be 20  $^{\circ}\text{C}$ . To avoid the external feedback into the DFBs, two cascaded isolators are applied for isolation better than 60 dB. In addition, the fiber end in the coupling system is angle polished. The absence of sensitivity to external feedback is confirmed by the fact that the measured linewidth does not change even when the tilted angle of the coupling fiber is varied by about 3 degrees.

### ***3.3. QDs for narrow linewidth operation***

The self-homodyne spectra of device *B* biased at different pump levels are shown in Fig. 3.3 with their Lorentzian curve-fits. Although the spectral tails at high pump levels fall off faster than the fitted Lorentzian functions, the parts of the spectra within 3 dB from the peak still deviate less than 1% from ideal. This suggests that there are small non-Lorentzian components in the noise of the devices. For the case of the QW DFB, the non-Lorentzian tale is not observed as illustrated in Fig. 3.4. The origin of the non-Lorentzian linewidth in these QD devices is unclear at present.

Fig. 3.5 shows the linewidths and SMSRs of the three QD DFBs as a function of the optical output power. The linewidth-power product of devices *A* and *B* is about 1.2 MHz-mW for the output power less than 2 mW, which is more than an order of magnitude



smaller than the value of 16 MHz measured in the commercial QW DFB at 2 mW output with the same setup, while the typical linewidth-power product in QW DFBs is tens of MHz – mW depending on the cavity length [87]. This result is physically consistent with the properties of the QD gain media discussed in the introduction section, as well as the implementation of the loss coupled grating, which reduces the adverse spatial-hole-burning effect [13], and the HR/HR coatings that lower the threshold gain. In device *C*, due to its larger gain offset and therefore larger  $\alpha_0$ , a wider linewidth at low power compared to device *A* and *B* is observed.

Table 3-2 Estimating the figure of merit for narrow linewidth in QD DFBs

Mirror Loss :  $\alpha_m = \frac{1}{2L} \ln\left(\frac{1}{R_1 R_2}\right) = 4.7 \text{ cm}^{-1}$

Internal loss :  $\alpha_i \approx 2 \text{ cm}^{-1}$

Slope efficiency of QD FPs :  $\eta_{\text{FP}} = 0.25 \text{ mW/mA} \propto \frac{\alpha_m}{\alpha_i + \alpha_m}$

Slope efficiency of QD DFBs :  $\eta_{\text{DFB}} = 0.14 \text{ mW/mA} \propto \frac{\alpha_m}{\alpha_i + \alpha_m + \alpha_{\text{grating}}}$

DFB grating loss :  $\alpha_{\text{grating}} = \frac{0.11}{0.14} (\alpha_i + \alpha_m) = 5.3 \text{ cm}^{-1}$

DFB threshold modal gain :  $\Gamma g_{\text{th}} = 12 \text{ cm}^{-1}$

Output coupling factor :  $F = 1$ , since most of the light is output from one facet

Linewidth - power product :

$$(\Delta\nu)_{\text{linewidth}} P = \frac{\Gamma g_{\text{th}} v_g^2 F \alpha_m h\nu}{4\pi} n_{\text{sp}} (1 + \alpha^2) = 0.8 \text{ MHz} - \text{mW} \text{ at } 1 \text{ mW output}$$

$$n_{\text{sp}} (1 + \alpha^2) = 23$$

To understand the narrow linewidth of the QD DFBs, threshold modal gain, mirror loss and  $n_{sp}(1+\alpha^2)$  is estimated and compared to the values of typical QW DFBs. By knowing the internal loss, mirror loss and the slope efficiency of the QD FPs with the same facet coatings on the same wafer processed for QD DFBs, the threshold DFB modal gain and  $n_{sp}(1+\alpha^2)$  are estimated to be  $12 \text{ cm}^{-1}$  and 23, respectively, from the fact that device A has a linewidth-power product of 800 KHz-mW at an output power of 1mW. For a comparison, Fig. 3.7 shows the values of  $n_{sp}(1+\alpha^2)$  in different semiconductor gain media. Since both small  $n_{sp}(1+\alpha^2)$  and low threshold gain are required for narrow linewidth operation, QDs are advantageous compared QWs. Fig. 3.7 suggests that the narrow-linewidth operation is improved by a factor 4-5 in quantum dot DFBs due to the unique material properties of QDs.

### ***3.4. Linewidth re-broadening in QD DFBs: gain compression***

As the output power is further increased, we can observe that a linewidth floor of 500-600 kHz is achieved in device B for optical outputs of 3-10 mW. Although device A shares the same property of low linewidth-power product in device C, its linewidth re-broadens instead of reaching a floor. Those phenomena are presented in Fig. 3.5. In each device, it is notable that the linewidth rebroadens or minimizes even as the SMSR is improving and greater than 50 dB as demonstrated in Fig. 3.5. Thus, the origin of the broadening is not related to the mode competition caused by the degradation of SMSR. Since the loss-coupled grating reduces the non-uniformity of the optical power distribution along the cavity compared to the  $\lambda/4$  phase-shifted quantum well DFB, spatial hole burning cannot underlie the linewidth behavior of these QD DFBs. As shown

in Chapter 2 from the small-signal response, the gain compression is strong in these QD devices. For the QD DFBs, the linewidth floor starts to occur at an output power of 2-4 mW, approximately the same as the value of the gain saturation power we derived from the small signal modulation. For the output power of 2-4 mW, at which the linewidth nonlinearity becomes significant in these devices, an inside-cavity photon density  $S$  of  $1.2\text{-}2.4 \times 10^{16} \text{ cm}^{-3}$  is found using Eqn. (2.33) in [87] for which a mode volume of  $440 \mu\text{m}^3$  and a mirror loss of  $4.8 \text{ cm}^{-1}$  are calculated for these lasers. From this  $S$  value, the gain compression coefficient of these QD devices is estimated to be  $4\text{-}8 \times 10^{-16} \text{ cm}^3$ , which is more than 30 times higher than the typical value of QWs and is consistent with both the value of  $4 \times 10^{-16} \text{ cm}^3$  published by D. Bimberg et. al. [9] and value of  $3\text{-}4 \times 10^{-16} \text{ cm}^3$  from the high speed measurement in Chapter 2. It is worth mentioning that no significant linewidth re-broadening or floor is observed in the commercial QW DFB with an improving SMSR as shown in Fig. 3.6, clarifying that the linewidth re-broadening is not from the testing setup.

As discussed in Chapter 2, the amplitude of FP modes around the excited states keeps increasing as the output of the QD DFBs rises. It is crucial to investigate if the amplified spontaneous emission (ASE) of the excited states contributes to the linewidth rebroadening or floor mentioned above, since the self-homodyne technique collects all the light from the DFBs. Therefore, an optical filter is introduced to filter out the excited state emissions and repeat the linewidth measurement. When the bandwidth of the filter is varied from 0.5 to 10 nm, the measured linewidth differs less than 3% as shown in Fig. 3.8. This excludes the possibility that the linewidth rebroadening and floor result from the increasing ASE of the excited states.

### 3.5. Effects of gain offset on the linewidth rebroadening

It was noticed by G. P. Agrawal that the alpha under gain compression changes differently as a function of the gain offset [98], that is, the position of  $\lambda_{\text{DFB}}$  relative to the gain peak. From the master equations describing the interactions of the photon-carrier system and carrier thermal equilibrium dynamics, the effective linewidth enhancement factor was derived to be:

$$\alpha_{\text{eff}} = \alpha_0 \sqrt{1 + \varepsilon S} + \frac{1}{g(\omega_L) \tau_{in}} \left( \frac{dg(\omega)}{d\omega} \right)_{\omega=\omega_L} \varepsilon S (1 + \varepsilon S) / (2 + \varepsilon S) \quad (3.2)$$

here  $\alpha_0$  is the linewidth enhancement factor without gain compression effects,  $\varepsilon$  is the gain compression coefficient,  $S$  is the photon density,  $g(\omega)$  is the small signal gain,  $\omega_L$  is the lasing frequency and  $\tau_{in}$  is the carrier dephasing time. Eqns. (3.1) and (3.2) show that the linewidth can re-broaden, reach a constant (floor), or narrow down faster than  $1/P$  with increasing power, depending on the sign of  $dg(\omega)/d\omega$  as determined by the offset of the DFB mode relative to the gain peak. The effects of gain offset indicated by Eqn. 3.2 are found applicable to the linewidth floor in device *B* ( $dg(\omega)/d\omega \sim$  zero) and the rebroadening in device *C* ( $dg(\omega)/d\omega$  positive), but not to the rebroadening in device *A* which has a blue-shifted gain offset. Theoretically,  $dg(\omega)/d\omega$  should be negative in this region of the gain spectrum and a linewidth narrowing faster than a  $1/P$  dependence should occur if the QD ground state is sufficiently isolated from other states. However, it is believed that the blue-shifted offset of device *A* is subject to the homogeneous and inhomogeneous broadenings from the excited states which causes an increase of the alpha [16], and that the gain spectrum does not have the inverted parabolic shape that would be expected for an idealized QD ground state.

### 3.6. Conclusion

Linewidths of QD LLC DFBs with different gain offsets from QD gain peaks are investigated and compared to a commercial QW DFB. The linewidth-power product of a QD DFB with a 300  $\mu\text{m}$  cavity is measured to be less than 1.2 MHz-mW for the output power less than 2 mW, more than one order less than the typical value of the QW DFB. Small internal loss, low mirror loss and low  $n_{\text{sp}}(1+\alpha^2)$  are the contributing factors for this significant improvement. The  $n_{\text{sp}}(1+\alpha^2)$  is estimated to 23 in QDs with a modal gain around 12  $\text{cm}^{-1}$ . It is unique for QDs to achieve this low modal gain and low  $n_{\text{sp}}(1+\alpha^2)$  simultaneously, while much higher modal gain is required for this low  $n_{\text{sp}}(1+\alpha^2)$  in QWs. Therefore, QDs are advantageous for narrow linewidth operation compared to QWs. On the other hand, due to the strong gain compression in QDs, the linewidths are found to re-broaden or floor at much lower photon density. Although the floor for the output power of 3-10 mW is 500 KHz, still small compared to typical QW DFBs, the gain compression is the limiting factor for the further reduction of linewidth at high output power. At the same time, the excited-state ASE is found not to contribute to the measured linewidth by applying an optical filter with variable bandwidth to the output of QD DFBs. Finally, the effects of gain offset of the QD DFBs are discussed. These results suggest that QD LLC DFBs with a larger mode volume to reduce the effect of gain compression and zero gain offset will have improved narrow linewidth performance.

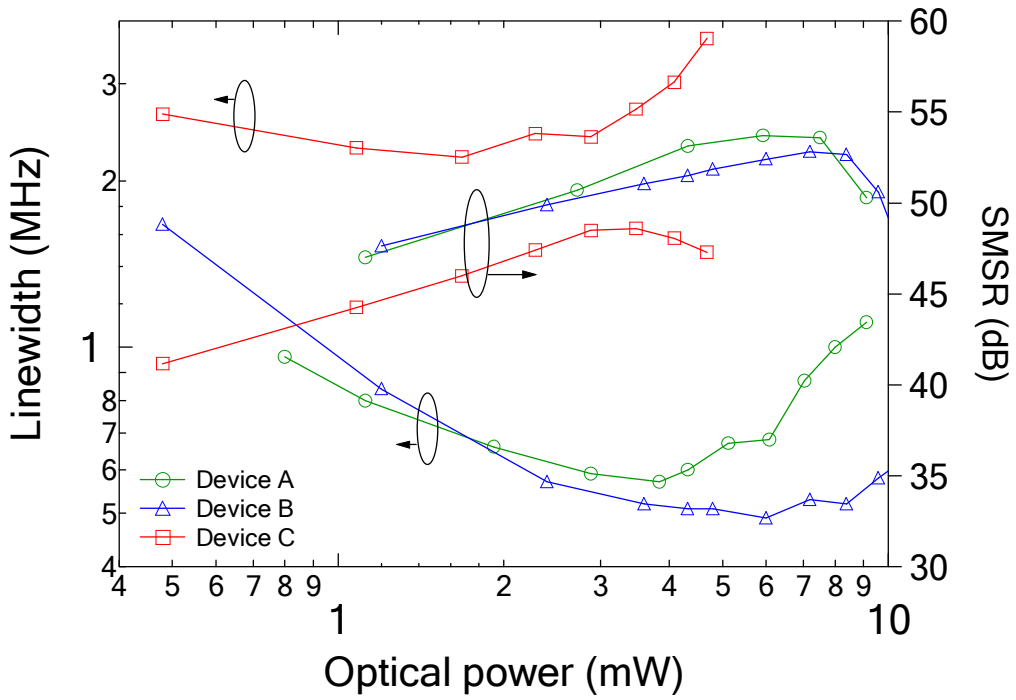


Fig. 3.5 Linewidths and SMSRs of the three QD DFBs as a function of optical output power.

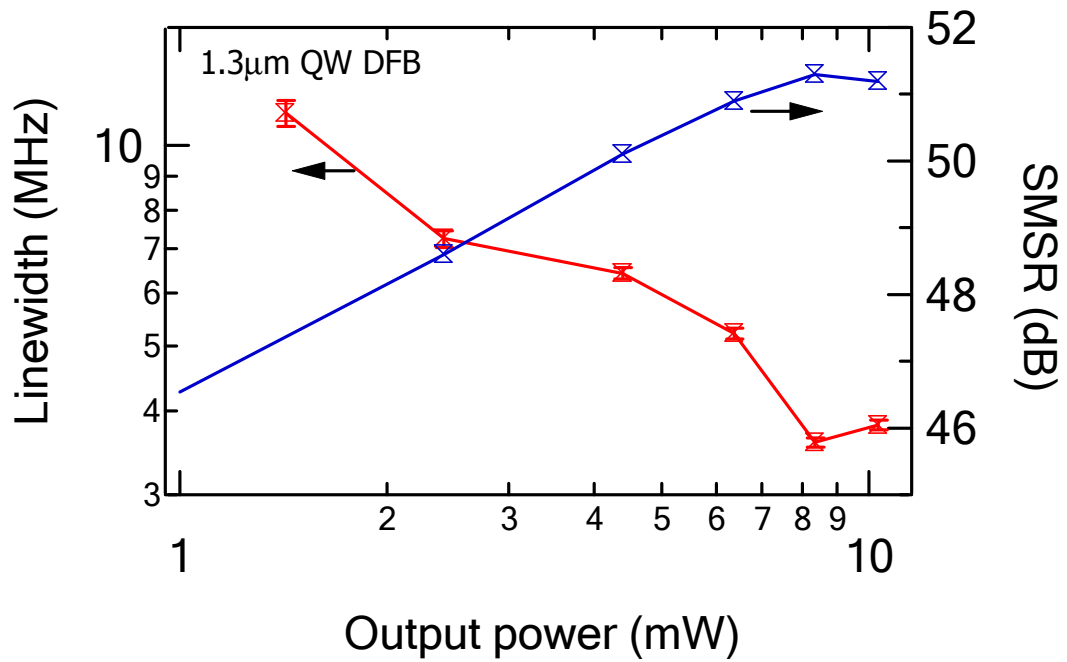


Fig. 3.6 Linewidth and SMSR of a commercial 1.3  $\mu\text{m}$  QW DFB.

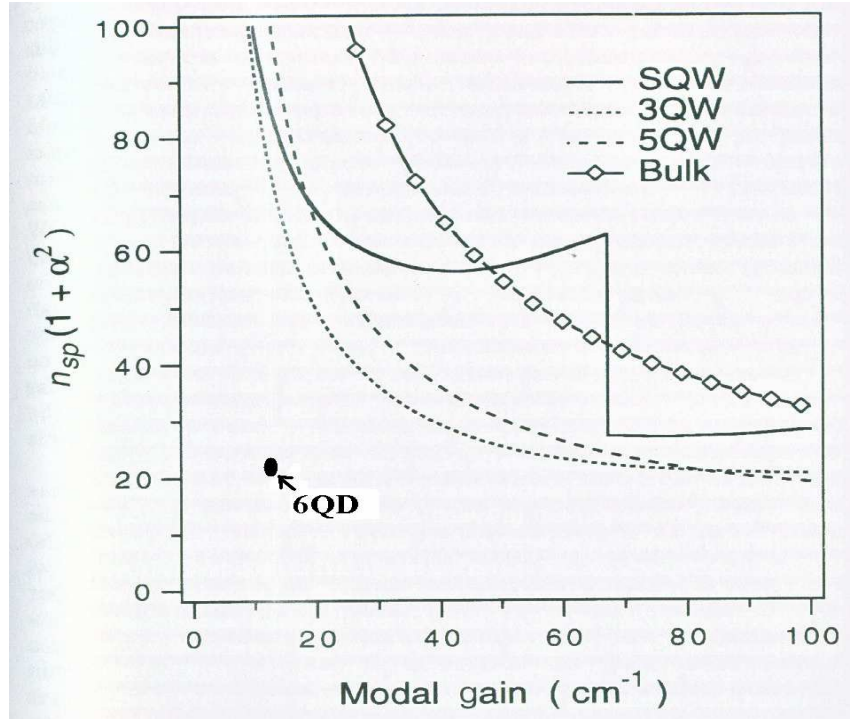


Fig. 3.7 The figure of merit for the spectral linewidth enhancement in semiconductor lasers  $n_{sp}(1+\alpha^2)$  at optical gain peak as a function of the modal gain in bulk DH, QW lasers with different number of quantum wells [101] and QD lasers with six stacks of DWELL.

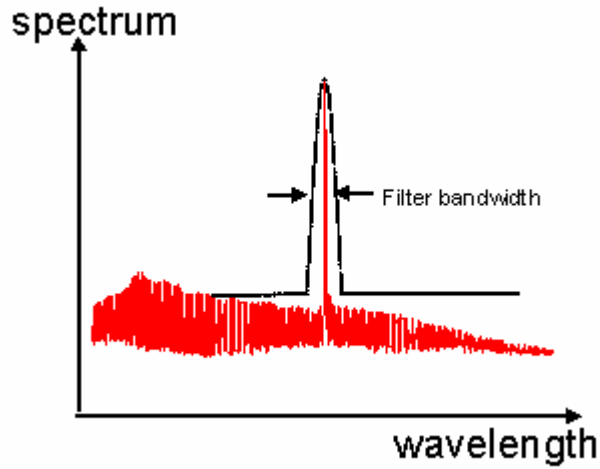


Fig. 3.8 Schematic plot for applying an optical filter to exclude the excited-state ASE from the self-homodyne measurement.

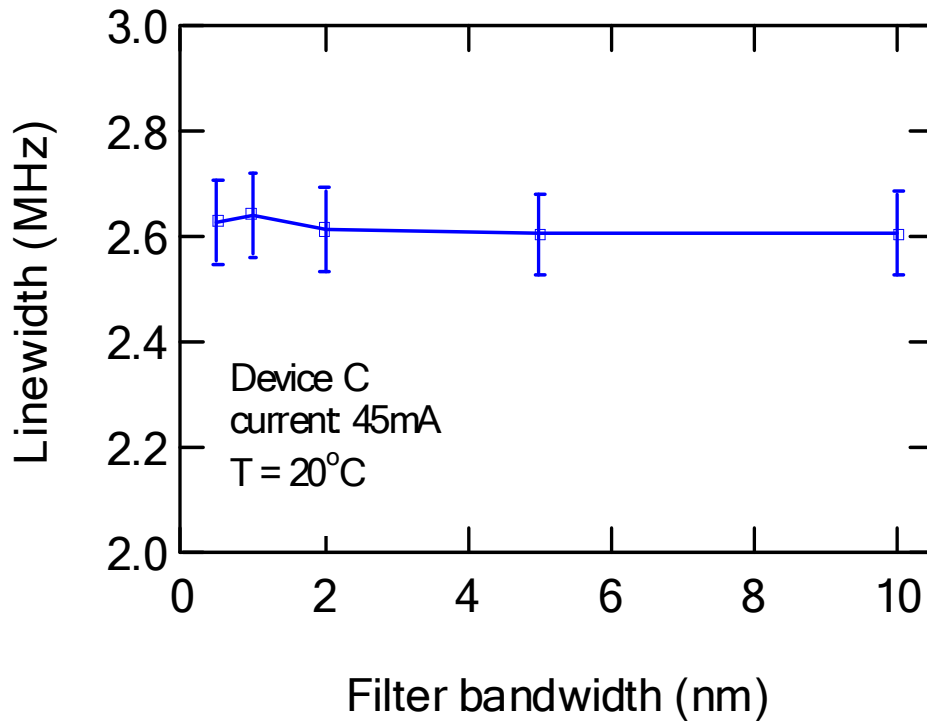


Fig. 3.9 The measured linewidths of the QD DFB device *C* with different bandwidth of the optical filter. The linewidths are found to be independent of the filter bandwidth.



## **Chapter Four. OD DFBS UNDER EXTERNAL FEEDBACK**

### ***4.1. Introduction***

A major problem with semiconductor lasers, both FP and DFB types, is that they are highly sensitive to the laser light which re-enters the laser cavity after being reflected by an external reflector. External optical feedback of the laser light usually causes instability of operation of a laser diode and generates excessive noise in optical communication systems [102,103]. A variety of optical elements, including lenses, fiber ends and integrated external cavities, can be the sources of unwanted optical feedback. For these reasons, costly and bulky optical isolators are typically required in most applications to protect semiconductor lasers from optical feedback-induced noise.

One of the consequences of the external feedback on a laser is coherence collapse. When the external feedback exceeds a certain level, the laser becomes unstable and the coherence of the laser output is dramatically reduced. The linewidth vs external feedback level is plotted in Fig. 4.1 from ref. [102], showing a narrowing of the linewidth as a function of external feedback before the coherence collapse point and a dramatic linewidth rebroadening after. Associated with the linewidth broadening is the increase of noise, which is demonstrated in Fig. 4.2. Avoiding coherence collapse is essential for real-world applications.

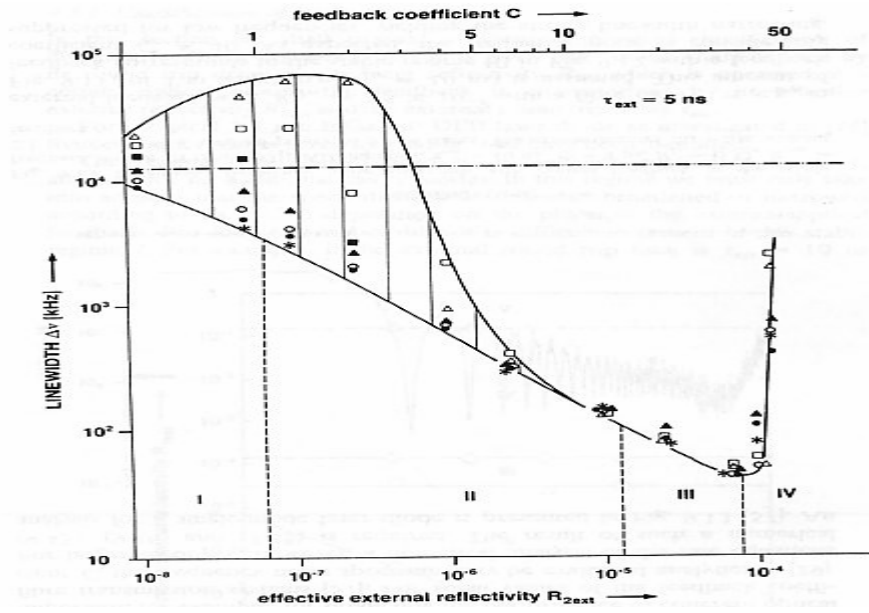


Fig. 4.1 Coherence collapse of a DFB laser is indicated by the dramatic broadening of the linewidth [102].

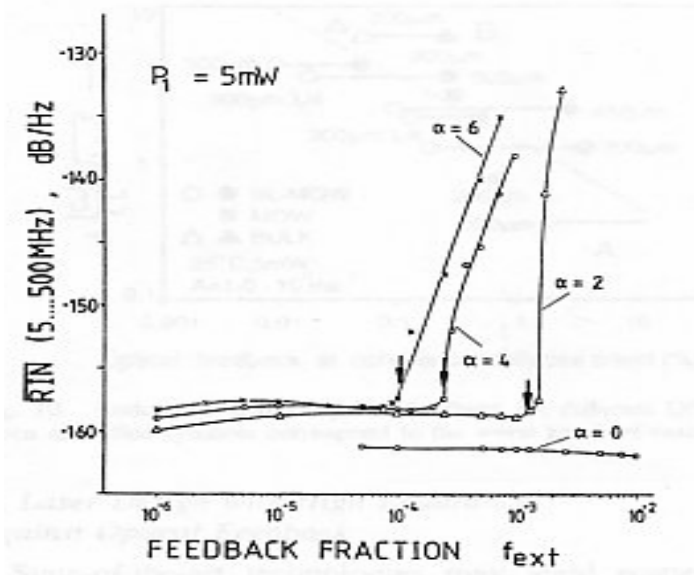


Fig. 4.2 The low frequency noise of a DFB under external feedback with different linewidth enhancement factors. Noise burst after coherence collapse is shown [102]. The  $\alpha$  in the figure stands for linewidth enhancement factor.

The effects of external feedback can be explained in Fig. 4.3. The external feedback is coupled into the laser cavity through the output facet and causes a perturbation on the photon density. As described by the rate equations on the small signal modulation, this perturbation leads to a fluctuation of the carrier density and thus the optical gain. The variation of gain itself changes the output power and consequently the external feedback strength. These processes form an intensity fluctuation loop that is effectively a self-intensity modulation and not sufficient to cause the complex dynamics of the laser system. On the other hand, since the fluctuations of optical index and gain are coupled by the linewidth enhancement factor, the external feedback can also introduce the phase fluctuation loop as indicated in Fig. 4.3. The interaction of the intensity and phase loop essentially makes the dynamics of the laser system under external feedback very complex and results in the system instability and even chaos.

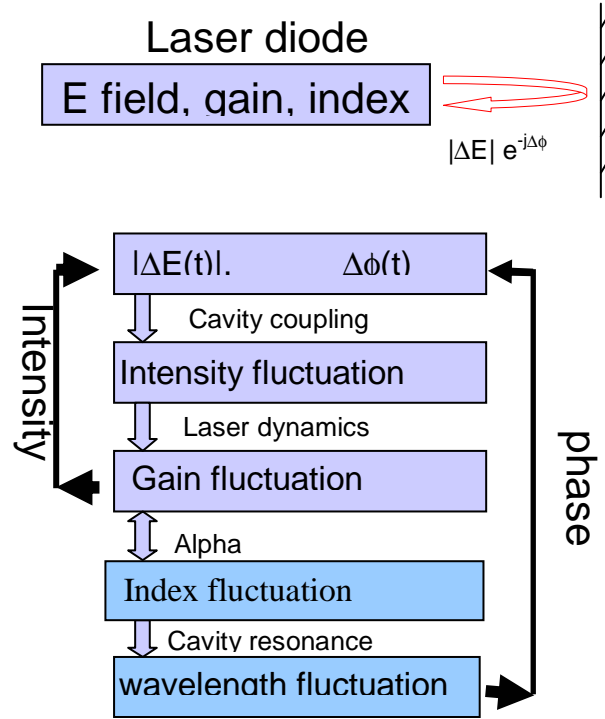


Fig. 4.3 A schematic presentation of the effects of external feedback on a semiconductor laser.

Fig. 4.3 also indicates the possible approaches to increase the external feedback resistance. First of all, to reduce the coupling of the laser diode to the external cavity will effectively reduce the external feedback strength. HR coated facets will help to diminish this coupling. Secondly, if the laser dynamics are heavily damped, the gain fluctuation introduced by the photon-density variation can be suppressed. Therefore, a large damping factor will increase the external-feedback resistance of the laser. Thirdly, we need to decouple the interaction between the intensity and phase loops by minimizing the linewidth enhancement factor (or alpha parameter). Finally, longer cavities have less change of the lasing wavelength for the same amount of phase fluctuation caused by the external feedback.

Petermann introduced a parameter to characterize the external feedback sensitivity: the critical external-feedback level for coherence collapse [102]:

$$f_{critical} = \frac{\tau_L^2 \gamma^2}{16|C_e|^2} \frac{1 + \alpha^2}{\alpha^4} \quad (4.1)$$

where  $\tau_L$  is the round trip time of the laser cavity,  $\gamma$  is the damping factor of the laser,  $C_e$  is the cavity coupling factor and  $\alpha$  is the linewidth enhancement factor.  $C_e$  is related to the facet reflectivity and is equal to  $(1-R)/(2R^{1/2})$  in the case of FP lasers. Compared to QWs, we can expect the improvement of external feedback resistance in QDs, since the much stronger damping and possibly smaller alpha as discussed in previous chapters. From the device point of view, the loss coupled grating, which is less subject to the spatial hole burning due to the more uniform distribution of the optical intensity along the cavity compared to conventional quarter-wavelength shift index coupled gratings, and the HR coated facet are also beneficial to improve the external feedback resistance. The

motivation of this chapter is to investigate the behavior of the device under external feedback and demonstrate the improvement in the external feedback resistance in LLC QD DFBs.

## 4.2. *Experimental setup*

The setup for the feedback experiment is shown in Fig.4.4. The laser output is coupled into a 3 dB optical fiber coupler. The feedback ratio is controlled by a variable optical attenuator, which gives attenuation from 1.5 dB to 80 dB. A film of 5000 Å Au is evaporated onto the flat fiber end of one arm of the coupler and functions as a reflective mirror. The distance between the laser and the external reflector is about 7 meters. It is noteworthy that the critical external feedback level for coherence collapse does not depend on the distance between the external reflector and the output facet of the device. To avoid excess uncontrolled feedback, the coupling lens is AR coated and the fiber ends are angle-polished in all connections. The external feedback ratio, which is defined as the ratio of the power reflected back to the laser facet and the single-facet output power of the device, is calculated as follows:

$$\Gamma_{\text{dB}} = P_1(\text{dBm}) - P_0(\text{dBm}) + C_{\text{dB}} \quad (4.2)$$

where the  $P_1$  is the reading from the power meter in Fig. 4.4,  $P_0$  is the output power of the laser and  $C_{\text{dB}}$  is the -3.4 dB coupling loss from the semiconductor laser to the fiber. The coupling loss  $C_{\text{dB}}$  is determined by the ratio between the total power after the 3dB optical coupler (assumed loss-less) and the output power directly measured at the facet of the DFB. The polarization controller is adjusted to obtain the maximum feedback effect to

guarantee the same polarization of the feedback beam and the DFB cavity mode. The device is epoxy-mounted on a heat sink and the temperature is controlled at 20 °C.

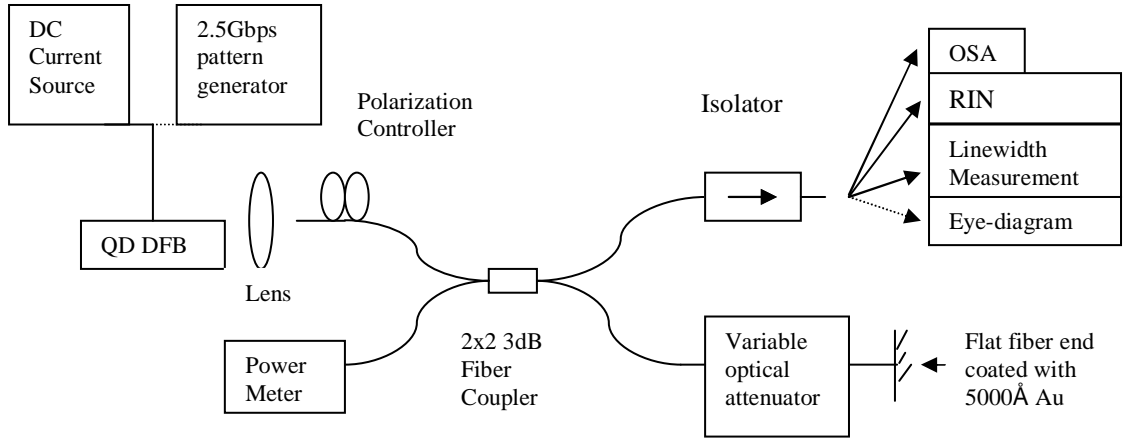


Fig. 4.4 Schematics of the experimental setup. The 2.5 Gbps pattern generator was used only for the eye-diagram measurement.

### ***4.3. Spectrum stability under external feedback: OSA spectrum and linewidth***

Optical spectra of the QD DFB under two different feedback levels are shown in Fig.4.5. For a feedback ratio of -14 dB, the lasing spectrum peak is slightly shifted. However, the spectral width is unchanged within the OSA resolution limit of 0.06 nm. As a comparison, the spectrum of a commercial 1.3  $\mu\text{m}$  InGaAsP/InP QW lambda/4 phase-shifted DFB with and without external feedback is presented in Fig. 4.6. In the case of the QW DFB, the -20dB spectrum width is broadened about 50% due to the -14dB external feedback. Therefore, the QD DFB shows a higher external feedback resistance considering the degradation of the optical spectrum.

For a higher resolution measurement, the linewidth of the DFB laser is determined by self-homodyne technique [104] with a fiber interferometer having a fixed delay of 3.5  $\mu$ s. The linewidth with an external feedback ratio below -60 dB is 650 kHz at 5 mW output. As the feedback ratio increases, the linewidth narrows down quickly until the feedback ratio reaches -14 dB, where the linewidth rebroadening occurs due to the coherence collapse. However, the laser linewidth under -14 dB feedback is still less than 20 kHz, much less than the 650 kHz free-running linewidth. This result confirms the unchanged spectrum measured by OSA. For comparison, the critical coherence collapse feedback ratio of an index-coupled QW DFB is typically between -20 and -30 dB [1, 11], which we also confirmed in Fig. 5.8 by a measurement of the commercial QW DFB. For the 802.3ae 10 Gbps Ethernet standard, the laser must tolerate up to -12 dB feedback from the network. For typical coupling losses of 4-6 dB in fiber-pigtailed lasers, a feedback ratio of -14 dB at the laser facet corresponds to -2 to -6 dB feedback from the system. Thus, the QD LLC-DFB has the potential to operate as an isolator-free light source in fiber-optic communication networks.



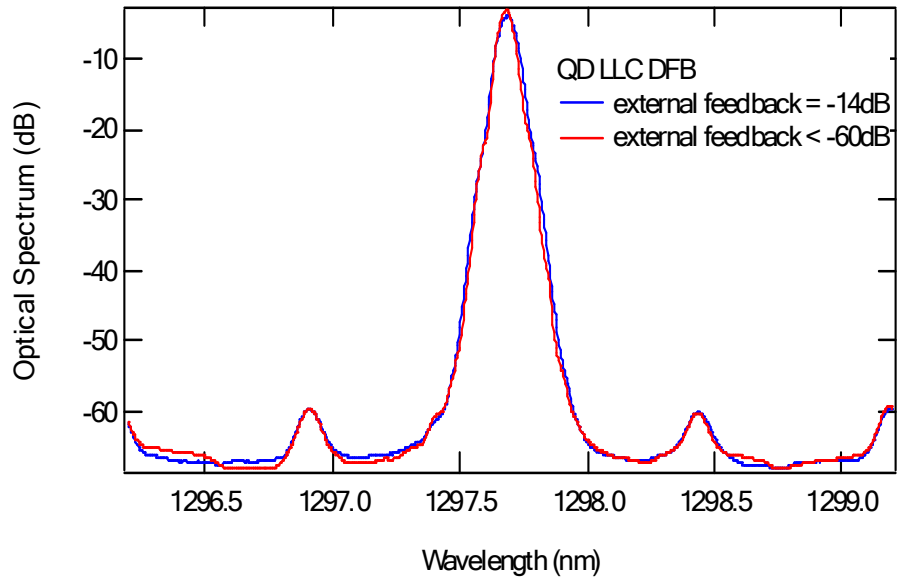


Fig. 4.5 The optical spectra of the QD LLC DFB with -14 dB and less than -60 dB external feedback. No significant broadening is observed with the resolution of the optical spectrum analyzer to be 0.06nm.

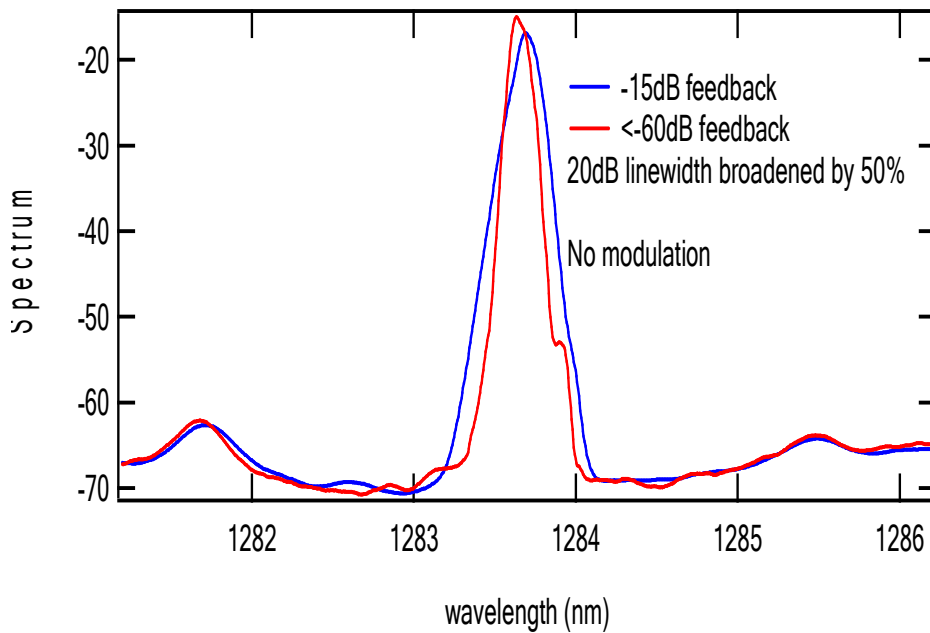


Fig. 4.6 Spectra of the commercial QW DFB with -15 dB and less than -60 dB external feedback. Significant broadening is observed.

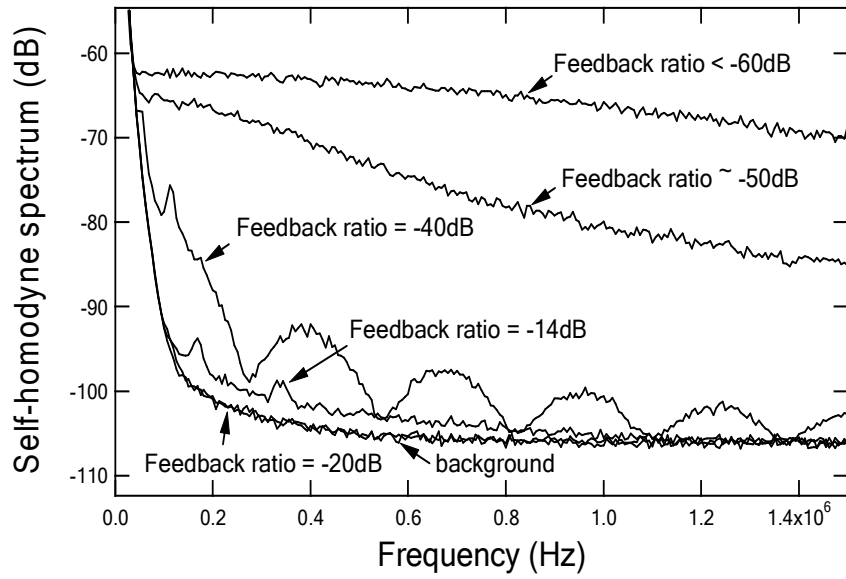


Fig. 4.7 Self-homodyne spectra of the QD DFB under different external feedback strength, while linewidth re-broadening occurs at  $-14\text{dB}$ .

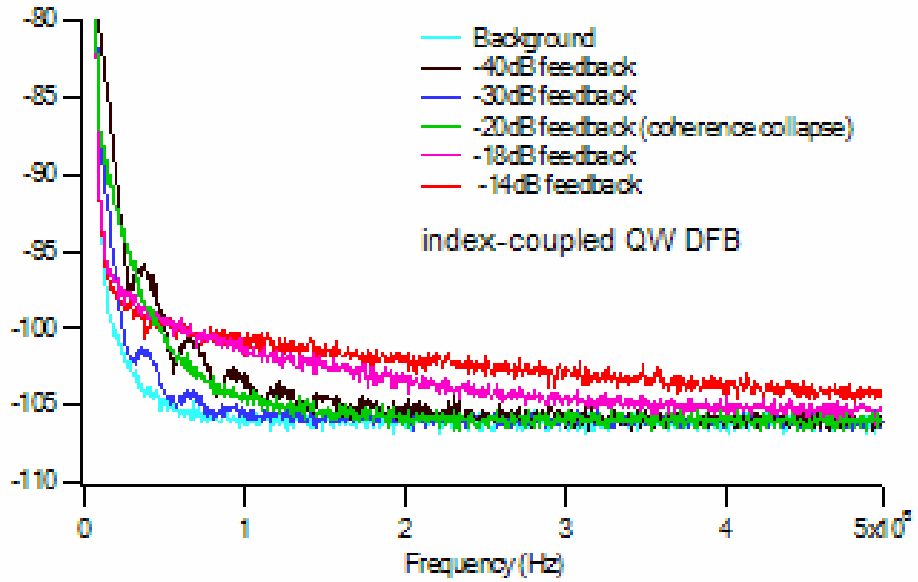


Fig. 4.8 Self-homodyne spectra of the commercial QW DFB under external feedback strength, the linewidth re-broadening at  $-20\text{dB}$  external feedback can be clearly observed.

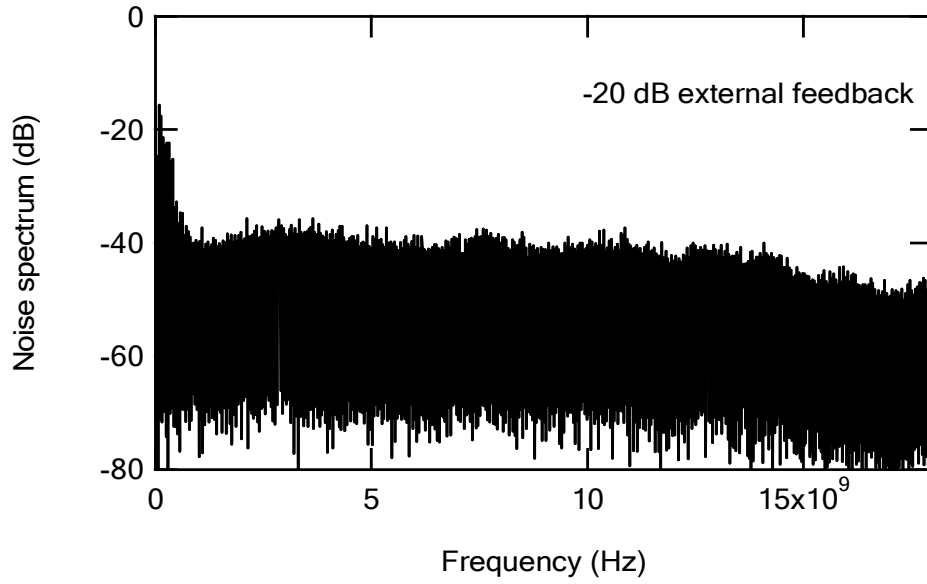


Fig. 4.9 The noise spectrum of the QD LLC DFB before coherence collapse. Low frequency noise is the dominant component of the spectrum.

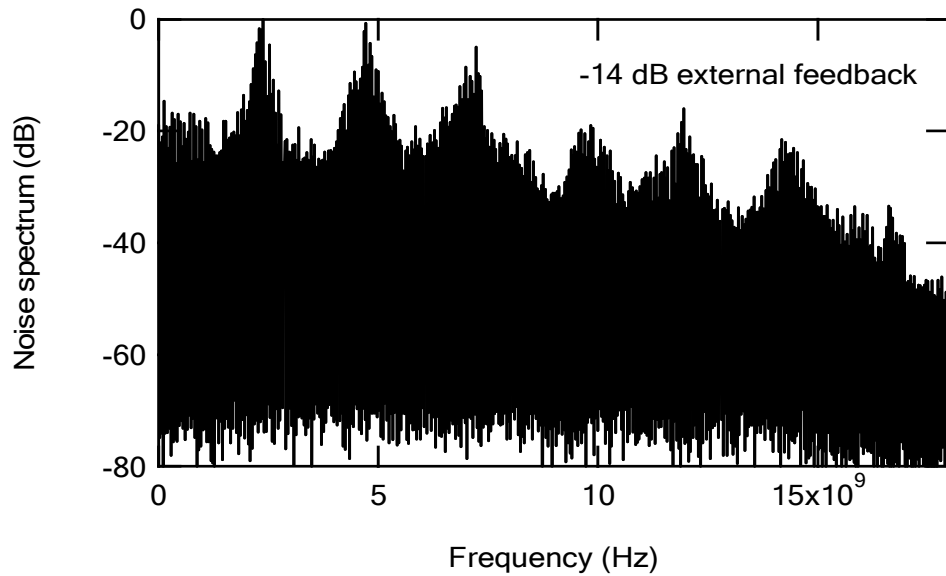


Fig. 4.10 The noise spectrum of the QD LLC DFB at coherence collapse. The spikes at integer multiples of the relaxation frequency in the noise spectrum are the indications of the coherence collapse.

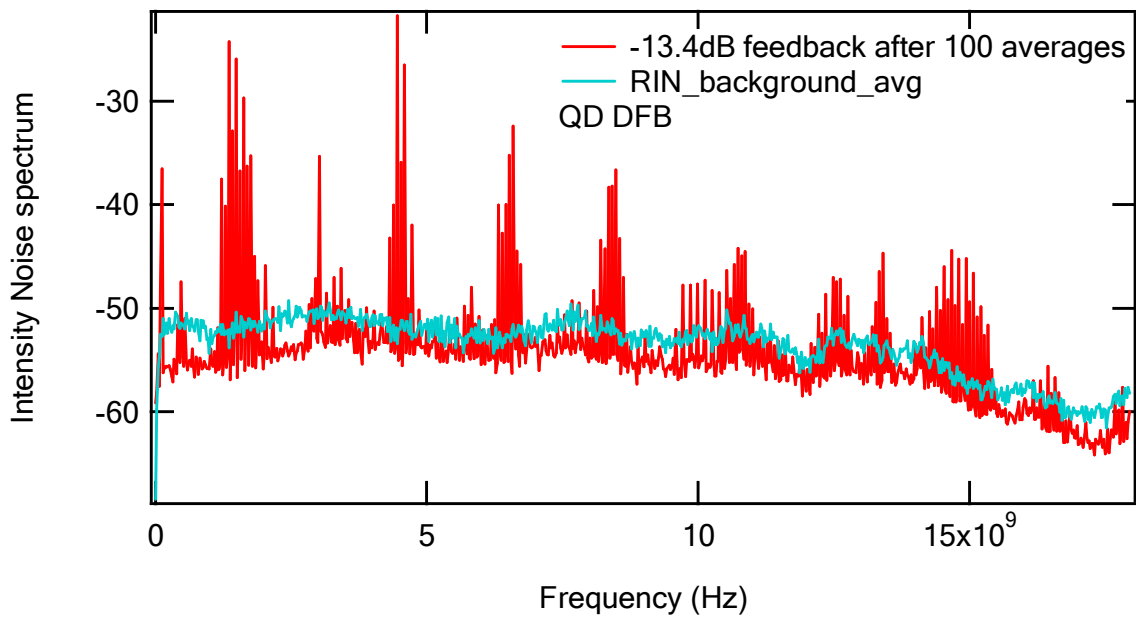
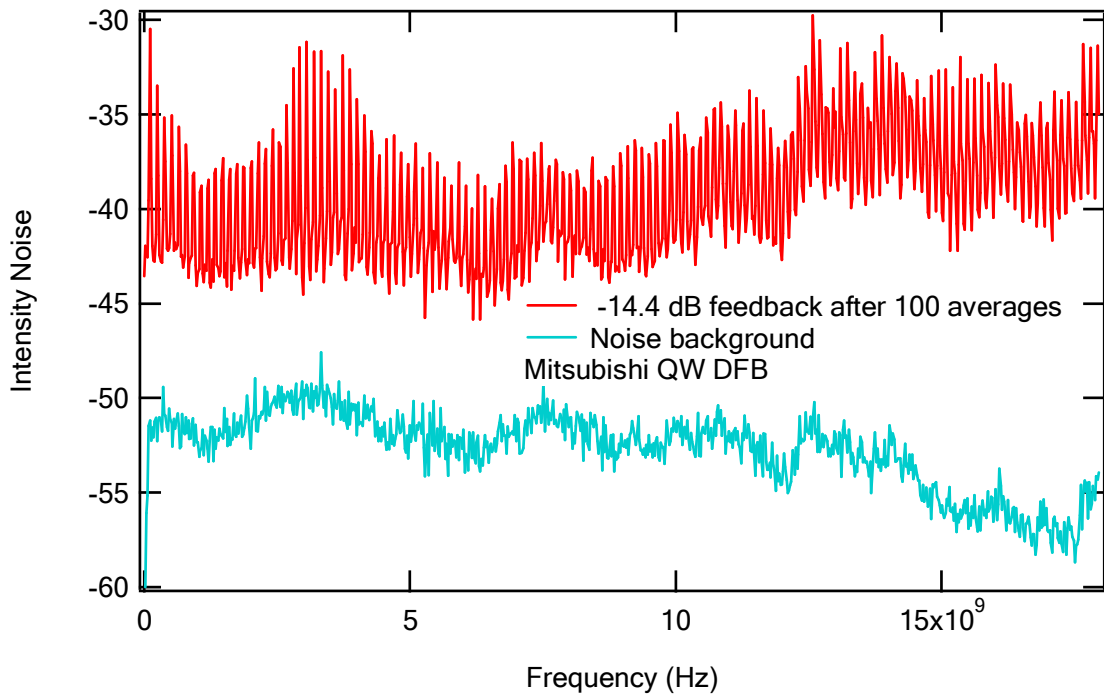


Fig. 4.11 The noise spectra of the QD LLC DFB and the QW DFB under coherence collapse introduced by external feedback. QD LLC DFB shows a lower noise level compared to the commercial QW DFB.

#### ***4.4. DC Noise of QD DFBs under external feedback***

The noise of the QD LLC DFB is also investigated with external feedback. At weak external feedback, low frequency noise (<1 GHz) is found dominate in the noise spectrum of the QD LLC DFB as shown in Fig. 4.9. This is consistent to the observations reported in ref. [103]. As the external feedback is further increased into the coherence collapse regime, spikes at the integer multiples of the relaxation frequency become significant in the spectrum in Fig. 4.10. This is an indication of the complexity of the laser dynamics. This noise measurement also confirms that the critical external feedback level for coherence collapse is -14 dB. In Fig. 4.11, the noise spectra of the QD LLC DFB and index-coupled QW DFB under -14 dB external feedback are compared. The RIN in the QW DFB is about 7 dB higher than in the QD DFB, indicating a higher resistance to the external feedback in the case of QD DFBs.

#### ***4.5. Degradations of signal to noise ratio and jitter under external feedback***

It is possible, however, that the degradation of the signal to noise ratio (SNR) would limit the laser performance under feedback at a level significantly less than what is required to induce coherence collapse [102,103,105]. Eye diagrams under 2.5 Gbps modulation are shown in Fig. 4.12 for the QD DFB feedback of (a) -60 dB, (b) -20 dB and (c) -14dB respectively. Both of the '1' and '0' levels are appreciably broadened when the feedback changes from -60 dB to -14 dB due to the excess intensity noise induced by the external feedback. The signal to noise ratio of the eye diagram with different feedback ratios is shown in Fig. 4.13. We use a commercially-available QW DFB as reference. Both the lasers have an output power of 5mW and an extinction ratio of 6.6 dB.

The QW DFB has a higher SNR at low levels of feedback than the QD DFB although we believe that this is not an inherent feature of the QD technology since a RIN as low as -146 dB at an output power of about 4 mW was measured in these devices. It is obvious that the commercial QW DFB signal to noise ratio (SNR) starts to degrade at a feedback ratio of -50 dB, which is the same value reported in the literature for the feedback that causes excess noise in typical QW DFB's [105]. In contrast, the SNR of the QD DFB starts to degrade at a feedback level around -30 dB. This result amounts to about 20 dB improvement of the feedback resistance in the QD DFB. The shoulder near -22 dB on the QW DFB curve in Fig. 4.13 is due to the coherence collapse. The signal to noise ratios of the QD LLC-DFB under -20 dB and -14 dB external feedback are 8.3 and 6.0, and the bit-error-rate (BER) are theoretically calculated to be  $4 \times 10^{-17}$  and  $10^{-9}$  respectively [106]. For the typical fiber coupling efficiency mentioned above, the QD DFB should still be able to tolerate network feedback in terms of maintaining sufficient SNR without an isolator.

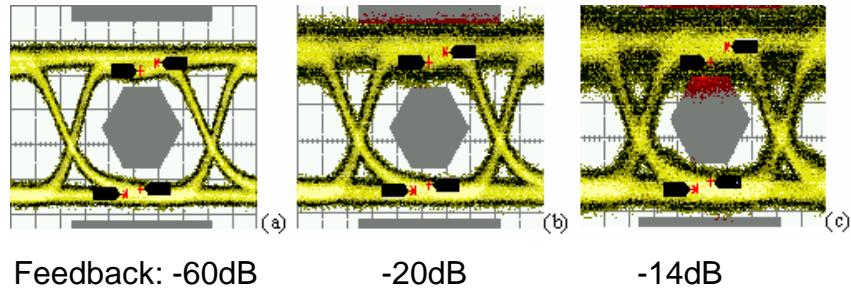


Fig. 4.12. The eye-diagram of the QD DFB under 2.5 Gbps modulation with different external feedback levels.

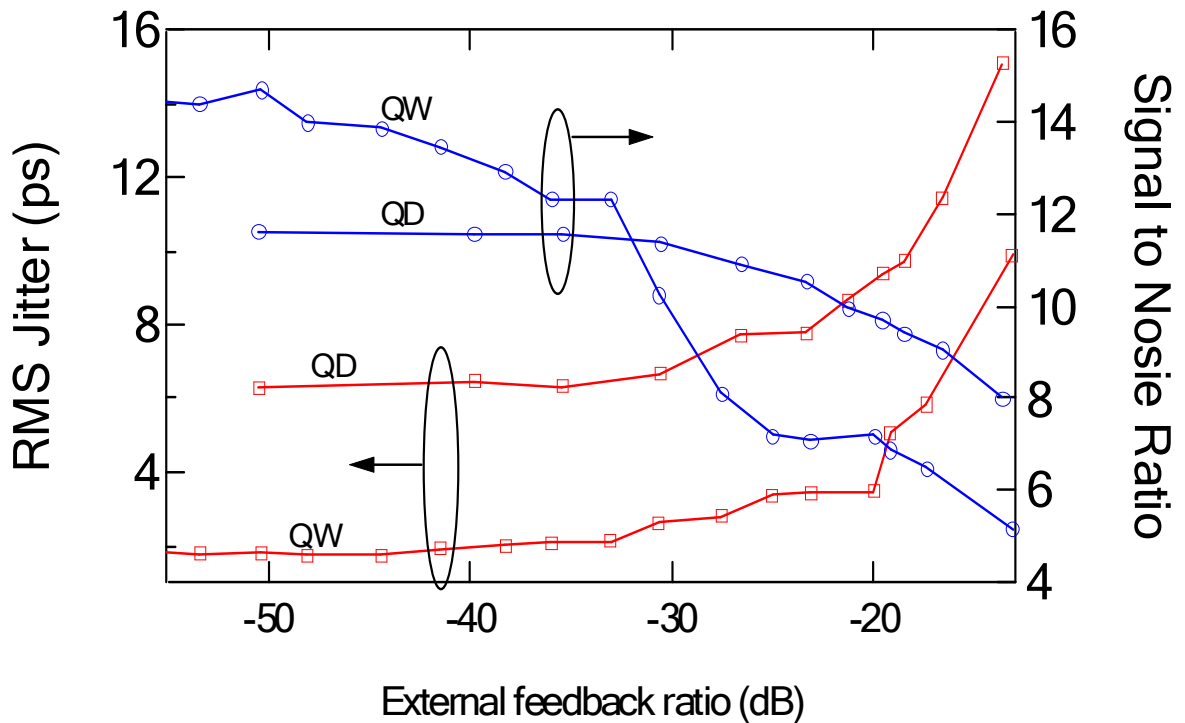


Fig. 4.13. The root-of-mean-square jitter and signal-to-noise ratio (SNR) of the QD LLC DFB and QW DFB under different external feedback ratios. Although the degradation of the jitter is more same for the two devices, the SNR of the QD DFB starts to degrade under -30dB external feedback, about 20 dB improvement compared to the QW DFB.

## **Chapter Five.      CHIRP OF QD DFBS**

### ***5.1. Introduction***

To explore the potential of QD DFBS for communication systems, knowledge of the optical spectrum of the devices under modulation is critical. The optical spectrum of a modulated laser typically gets broadened due to the direct intensity modulation and the resulting frequency chirp. Chirp has two major detrimental outcomes in a typical transmissions system. The first is that the chirp can interact with the fiber dispersion to create a power penalty, which ultimately limits the number of channels or the distance over which the signal can propagate in today's wavelength division multiplexed (WDM) systems. The second is that chirp can broaden the transmitted spectrum limiting the channel spacing by interfering with adjacent channels even in a short-haul ultra-dense WDM environment. Therefore, low chirp semiconductor lasers have been of interest for a long time [107-112]. The development of quantum dot lasers has been expected to improve the chirp characteristics considering the small linewidth enhancement factor [113,114].

QD lasers with a frequency chirp one order of magnitude lower than that of QW lasers were demonstrated in ref. [113]. Grown by MBE, the QD lasers are designed for high aspect ratio (height/base diameter), so that the ground state is well separated from the first excited states by about 70 meV, which is larger than the room-temperature thermal energy. The gain medium consists of three InAs QD layers but the gain is still low. Therefore, 97% HR coatings on both facets and a cavity length of 970  $\mu\text{m}$  are necessary to lower the threshold gain. This low threshold gain can reduce the adiabatic chirp of the



devices [115]. Although these devices show a good chirp performance, they are less desirable for practical applications in terms of the lasing wavelength (1.2  $\mu\text{m}$ ), low output power ( $\sim 0.1$  mW) and low slope efficiency (0.01 mW/mA). Furthermore, due to the limitation of the device performance and experimental setup, the authors only qualitatively compared the chirp of QD to QW FP lasers and no quantitative measurement is carried out to investigate the alpha factor and gain compression coefficient in the QD devices.

Due to the relatively low modal gain of the QD gain media, multiple stacks of QDs are necessary for good high-speed performance. The multi-stack structure increases the inhomogeneous broadening and thus the linewidth enhancement factor [16]. The alpha factor also becomes larger when the excited states are populated [16], which is severe considering the typical spacing between the ground state and the first excited state is around 45 meV for 1.3  $\mu\text{m}$  QDs as shown in Chapter.1. Moreover, the strong gain compression in QDs demonstrated in previous chapters makes the alpha factor power-dependent and become large at elevated outputs. The adiabatic chirp is also expected to be large due to the gain compression. It is crucial to understand the effects of these factors on the chirp performance of QD lasers. On the other hand, a quantitative time-resolved-chirp measurement is possible [116] as a result of the single-mode operation and several mWs output power of the QD LLC DFBs. This offers, for the first time as we know, an opportunity to study the alpha factor and gain compression in a device above threshold, which can be much different from the values measured below threshold [7,16]. The motivations of this chapter are to measure the chirp and thus estimate the alpha

factor and gain compression coefficient of the QD LLC DFBs. The definition of the gain compression coefficient is given in Eqn. (2,4).

Chirp is the drift of the optical wavelength of a laser under direct intensity modulation. The rate equations describing the photon density and frequency of a laser are given as following:

$$\frac{dS}{dt} = \left( \frac{\Gamma v_g g}{1 + \epsilon S} - G_{th} \right) S + R_{sp} \quad (5.1)$$

$$\Delta \nu = \nu - \nu_{th} = -\frac{\nu_{th}}{n} \Delta n = -\frac{\nu_{th}}{n} \frac{\partial n}{\partial g} (g - g_{th}) = \frac{\alpha}{4\pi} \Gamma v_g (g - g_{th}) = \frac{\alpha}{4\pi} (\Gamma v_g g - G_{th}) \quad (5.2)$$

where  $\Gamma$  is the confinement factor,  $v_g$  is the group index,  $g$  is the material gain,  $S$  the photon density,  $\epsilon_s$  is the gain compression factor associated with the photon density,  $G_{th}$  is the temporal threshold gain,  $R_{sp}$  the spontaneous emission rate,  $\alpha$  the linewidth enhancement factor,  $\nu$  is the lasing frequency,  $\nu_{th}$  is the frequency at threshold. After solving Eqn.(5.1) for  $\Gamma v_g g$  and putting it into Eqn. (5.2), we can have:

$$\begin{aligned} \Delta \nu &= \frac{\alpha}{4\pi} \left[ (1 + \epsilon_s S) \frac{dS}{S dt} + \epsilon_s S G_{th} - \frac{(1 + \epsilon_s S) R_{sp}}{S} \right] \\ &\approx \frac{\alpha(1 + \epsilon_s S)}{4\pi} \left[ \frac{dS}{S dt} + \frac{\epsilon_s S G_{th}}{(1 + \epsilon_s S)} \right] \\ &= \frac{\alpha(1 + \epsilon_p P)}{4\pi} \left[ \frac{dP}{P dt} + \frac{\epsilon_p P G_{th}}{(1 + \epsilon_p P)} \right] \end{aligned} \quad (5.3)$$

with  $P$  is the output power of the device,  $\varepsilon_p$  the gain compression coefficient associated with the output power. The spontaneous emission term is ignored since the laser operates well above the threshold. Since the gain compression is not severe in most of the QW lasers, that is  $\varepsilon_p P \ll 1$ , people typically approximate Eqn. (5.3) into:

$$\Delta v \approx \frac{\alpha}{4\pi} \frac{dP}{P dt} + \frac{\alpha}{4\pi} \varepsilon_p P G_{th} \quad (5.4)$$

with the first term, proportional to the derivative of the optical power, dubbed as transient chirp and the second term, proportional to the optical power itself, as adiabatic chirp [115]. Compared Eqn (5.3) and (5.4), the effective alpha considering the effects of gain compression can be expressed as:

$$\alpha_{eff} = \alpha(1 + \varepsilon_p P) \quad (5.5)$$

with the transient chirp is the dominant component in most of the QW lasers. It is notable that the adiabatic chirp is directly related to the gain compression coefficient and threshold gain of the lasers.

Equation (5.4) is well known for the measurement of alpha and the compression coefficient in QW lasers [115,117]. Since the gain compression effect is stronger in QDs than QWs, we use Eqn. (5.3), instead of Eqn. (5.4), to describe the chirp in QD DFBs. It is remarkable that Eqn. (5.3) can apply to lasers under large signal modulation. To obtain a large signal to noise ratio, the laser sources in some communication systems are digitally modulated with an extinction ratio of about 10 dB for a large separation of '1' and '0' levels. The chirp can be still well modeled by Eqn. (5.3) [118].

## ***5.2. Time-resolved chirp: Experimental setup and technical background***

The time-resolved chirp (TRC) is a technique to measure the wavelength chirping directly in the time domain. The wavelength chirp,  $\Delta\nu$ , of a laser under external modulation is measured in real time, while the output of the laser,  $P$ , is also recorded simultaneously. Based on the relation between  $\Delta\nu$ ,  $P$  and  $dP/dt$  expressed in Eqn. (5.3), the alpha factor and the gain compression coefficient can be extracted.

The experimental setup for TRC is given in Fig. 5.1. The pseudo-random pattern generator (PRPG) generates a 2.5 Giga-bit-per-second (Gbps) pseudo random '0' and '1' data string with a length of  $2^7-1$ . The optical filter in the OSA, originally designed for the monochromatic output, is used as a wavelength discriminator which transfers the wavelength chirping into optical intensity variation. The band pass of the optical filter is adjustable and has a minimum resolution of 0.04 nm, that is, 7.12 GHz at the wavelength of 1.3  $\mu\text{m}$ . If the band pass is set to be much larger than the spectral width of the modulated light, the OSA will transmit all of the spectral components and just convey the same output from the modulated DFBs, without spectral filtering, to the digital communication analyzer (DCA). Then the DCA records the un-filtered and filtered optical signals from the OSA with the information of the variations of the output power and wavelength chirping, respectively, in time domain. Since the PRPG and DCA are synchronized by the trigger output from the PRPG, the chirp and the optical intensity of the laser output can be aligned up in time domain, so that alpha factor and gain compression can be obtained based on Eqn. (5.3).

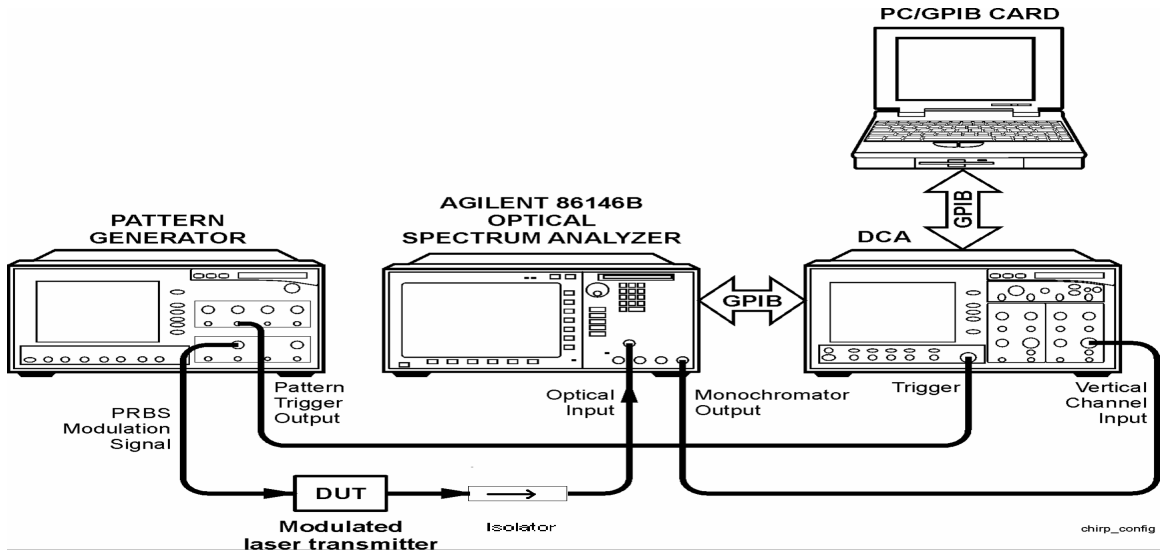


Fig. 5.1 The experimental setup for TRC measurement [116]. The QD DFB is modulated by the pattern generator and its wavelength chirping is translated into optical intensity variation and then recorded by the DCA.

$$\overline{\lambda(t)} = \frac{\sum_{i=1}^N A_{i,d} (\lambda_i - \lambda_s)}{\sum_{i=1}^N A_{i,d}}$$

where  $\lambda_s$  is the center wavelength of the modulated spectrum.

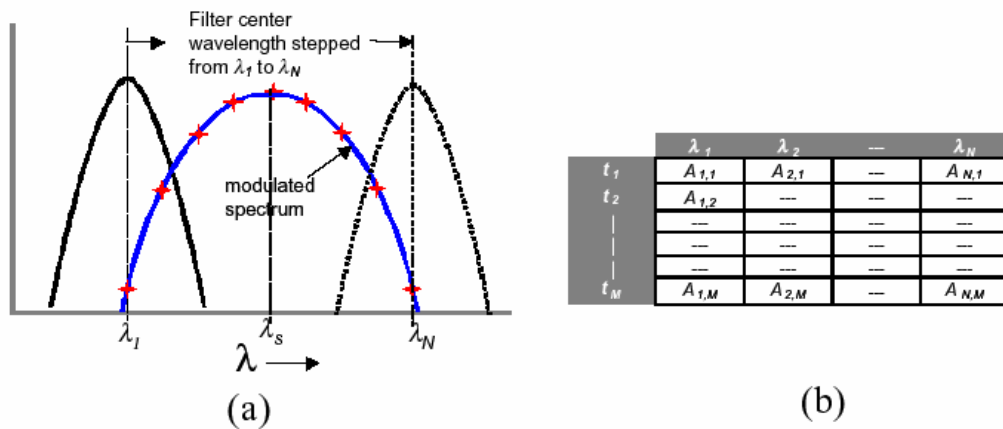


Fig. 5.2 A schematic drawing of the measurement of the wavelength chirping with the optical filter built in to the OSA [116].

The wavelength chirping is measured by the wavelength discriminator method [119] utilizing the very low dispersion monochromator of the 86146B OSA. Referring to Fig 5.2, the monochromator filter is step-tuned through the modulated laser wavelength. The lowest wavelength,  $\lambda_l$ , and the highest wavelength,  $\lambda_N$ , are set to fully tune through the chirped spectrum to achieve a 30-dB amplitude drop on each side of the filter response. At each wavelength, an intensity vs. time record of length M is measured on the DCA. The resulting collection of data contains the chirp information in an N by M matrix as shown in Fig. 5.2. For each row in the matrix, a weighted-average wavelength value of  $\delta\lambda(t)$  can be calculated based on the following algorithm with  $f(x)$  the transfer function of the optical filter.

Since the transfer function is symmetric about the center wavelength,  $\lambda_0$ , and the transmission for the wavelength far away from  $\lambda_0$  is vanished,  $f(x)$  can be expressed as:

$$f(\lambda_0, \lambda) = f(|\lambda - \lambda_0|) \xrightarrow{|\lambda - \lambda_0| \rightarrow \infty} 0 \quad (5.6)$$

with  $\lambda$  the wavelength of the light input to the filter. Then the matrix element  $A_{i,j}$  given in Fig. 5.2 can be calculated from the  $f(x)$  as:

$$A_{i,j} = f(\lambda_{0,i}, \lambda_{t=j}) = f(|\lambda_{0,i} - \lambda_{t=j}|) \quad (5.7)$$

with  $\lambda_{0,i}$  denotes the center wavelength at the  $i$ -th step-tune of the optical filter and  $\lambda_{t=j}$  the wavelength of the modulated DFB laser at time  $j$ . Therefore, the wavelength chirp can be obtained from the matrix  $A_{i,j}$ :

$$\overline{\delta\lambda(t)} = \frac{\sum_{i=1}^N A_{ij} (\lambda_i - \lambda_s)}{\sum_{i=1}^N A_{ij}} \quad (5.8)$$

based on the following property of the matrix A:

$$\begin{aligned}
\sum_{i=0}^{i=N} A_{i,j} \lambda_{0,i} &\approx \int_{-\infty}^{\infty} f(|\lambda_0 - \lambda_{i=j}|) \lambda_0 d\lambda_0 \\
&= \int_{-\infty}^{\infty} f(|\lambda_0 - \lambda_{i=j}|) (\lambda_0 - \lambda_{i=j}) d(\lambda_0 - \lambda_{i=j}) + \lambda_{i=j} \int_{-\infty}^{\infty} f(|\lambda_{i=j} - \lambda_0|) d(\lambda_0 - \lambda_{i=j}) \\
&= \lambda_{i=j} \int_{-\infty}^{\infty} f(|\lambda_i - \lambda_0|) d(\lambda_0 - \lambda_i) \\
&\approx \lambda_{i=j} \sum_{i=0}^{i=N} A_{i,j}
\end{aligned} \tag{5.9}$$

The LIV curves of the QD DFB tested are shown in Fig. 5.3. The threshold of the device is 5 mA and the slope efficiency is approximately 0.1 mW/mA. The resistance of the device is calculated to be 20.6 Ohms in the range of 10 mA – 40 mA DC bias. As the output of the pattern generator is designed to be voltage, the resistance is used to convert the voltage modulation-amplitude approximately into a current one. The device has a side mode suppression ratio of about 50 dB with a DFB wavelength of 1320 nm. All the testing is done with the heat sink temperature controlled to be 20 °C. Two 30-dB isolators are cascaded to avoid unintended external optical feedback.

### ***5.3. Chirp with a fixed extinction ratio of modulation.***

The extinction ratio of a digitally modulated signal is defined as the ratio between the power levels at the ‘1’ and ‘0’ states. For communication systems, a large extinction ratio is preferred to overcome the penalties of the transmission loss and noise. In this part of the experiment, we measure the chirp of the QD DFBs biased at different DC currents with the amplitudes of the digital modulations adjusted to keep an extinction ratio of about 10 dB. The eye diagram of the DFB output at 20 mA is presented in Fig. 5.4 with

an extinction ratio of 9.48 dB and shows no touching on the 2 Gbps internet standard mask. Since the rise time is estimated to be 120 ps and the fall time about 180 ps based on Fig. 5.2, we can conclude that the interference between the two '1' bits separated by a '0' bit is ignorable. This helps to eliminate the dependence of the measured chirp on the modulation pattern. Another significant feature of the eye diagram is that no overshoot is observed at the rising edge, indicating a reduced transient chirp. This is consistent with the strong damping rate from the high-speed measurement presented in Chapter 2.

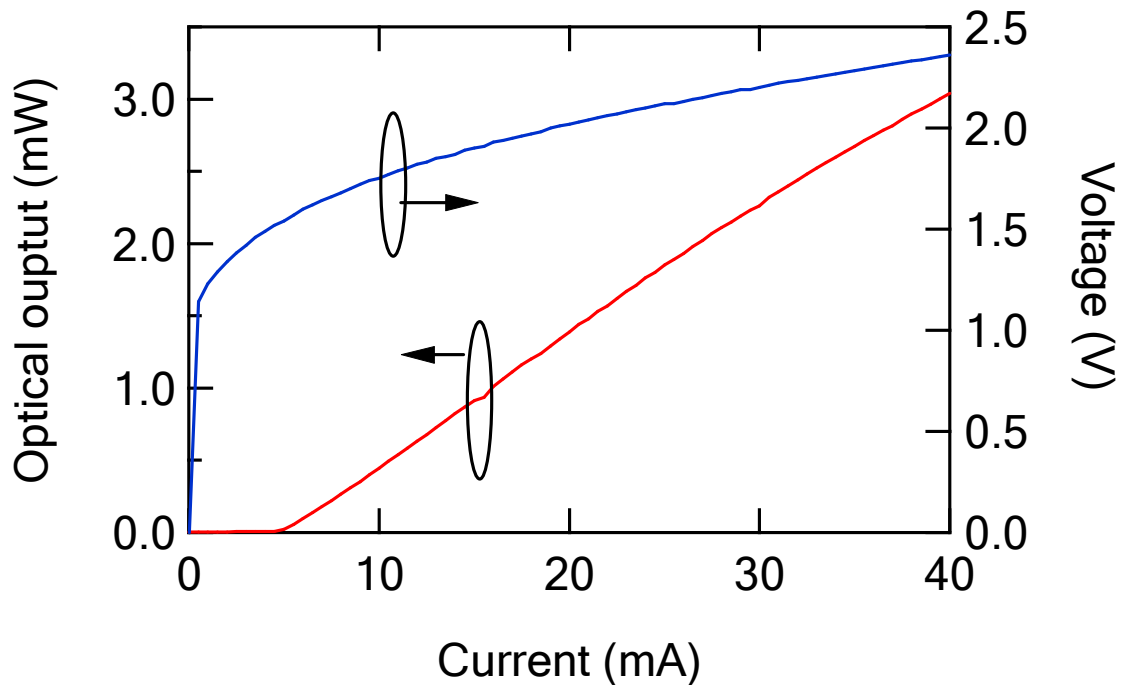


Fig. 5.3 LIV curves of the QD DFB for the TRC measurement.



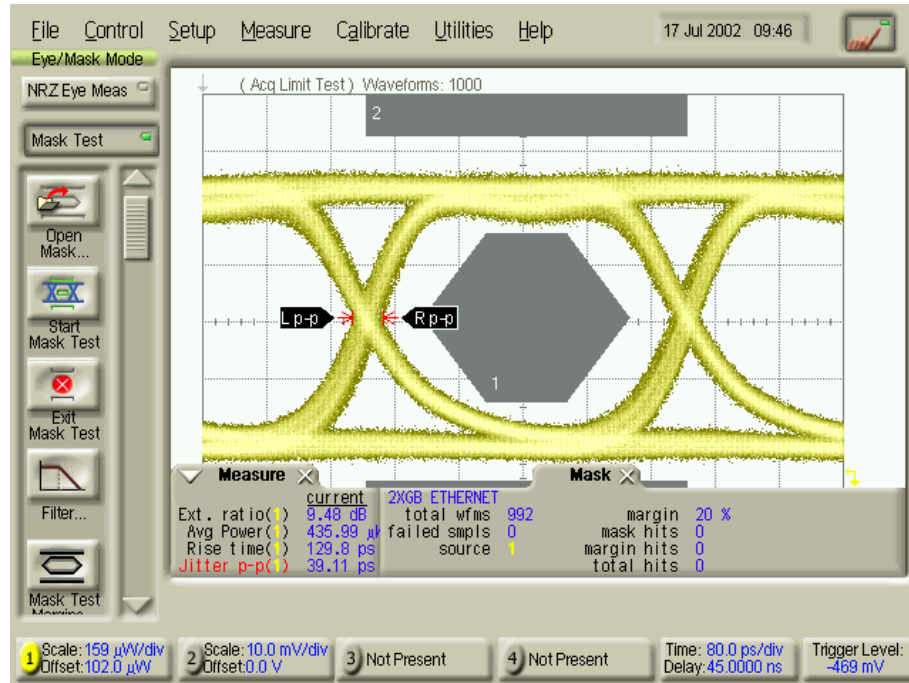


Fig. 5.4 The eye diagram of the output of the modulated QD DFB biased at 20 mA with an extinction ratio of 9.5 dB.

The measured time-resolved chirp and optical power of the QD DFB are given in Fig. 5.5. The output power of the QD DFB at 20mA is 1.4 mW. The total coupling loss of the fiber optical isolator and monochromator in OSA is measured to be - 12 dB. The power in Fig. 5.5 is the power output from the monochromator. The time resolved chirp of the QD DFB shows weak spikes at the rising edges of the modulated optical signal, and, significantly, the transient chirp does not dominate over the adiabatic chirp. As a comparison, a TRC result of a QW DFB is shown in Fig. 5.6, showing the dominance of the transient chirp over the adiabatic chirp. In QD DFBs, the transient chirp is suppressed due to the large damping factor discussed in Chapter 2 and the adiabatic chirp is enhanced due to the strong gain compression.

Table 5.1 gives the results of TRC measurement with the extinction ratio around 10 dB. The peak-to-peak voltages,  $V_{pp}$ , is the voltage modulation depth on the QD DFB for

the 10dB extinction ration (ER). The effective alpha is defined in Eqn. (5.4) with the gain compression effect included. The average chirp here is the difference between the average chirps on ‘1’ and ‘0’ levels. For the chirp is positive at ‘1’ levels and negative at ‘0’ levels, the alpha parameter here is a positive value. For large-signal modulation, higher order harmonic and nonlinear effects can be significant and cause a shift of the average optical frequency of the modulated light relative to the un-modulated one [120]. The *freq\_shift* in Table 5.1 gives this parameter, which is an importance factor determining the cross-talk strength between different channels in WDM communication systems.

Bias (mA)	Power (mW)	V <sub>pp</sub> (V)	ER (dB)	Effective Alpha	Avg chirp (GHz)	freq_shift (GHz)
15	0.912	0.57	<a href="#">9.34</a>	5.52	7.55	-0.75
20	1.39	0.84	<a href="#">9.48</a>	6.34	12.65	-1.35
25	1.85	1.15	<a href="#">10.16</a>	7.20	13.83	-1.44
30	2.26	1.4	<a href="#">9.92</a>	7.94	16.03	-1.72
35	2.67	1.64	<a href="#">9.73</a>	8.31	23.06	-2.71
40	3.04	1.93	<a href="#">9.82</a>	9.48	24.54	-2.75

Table. 5-1 The experimental results of the TRC of the QD DFB with the extinction ratio kept around 10 dB.

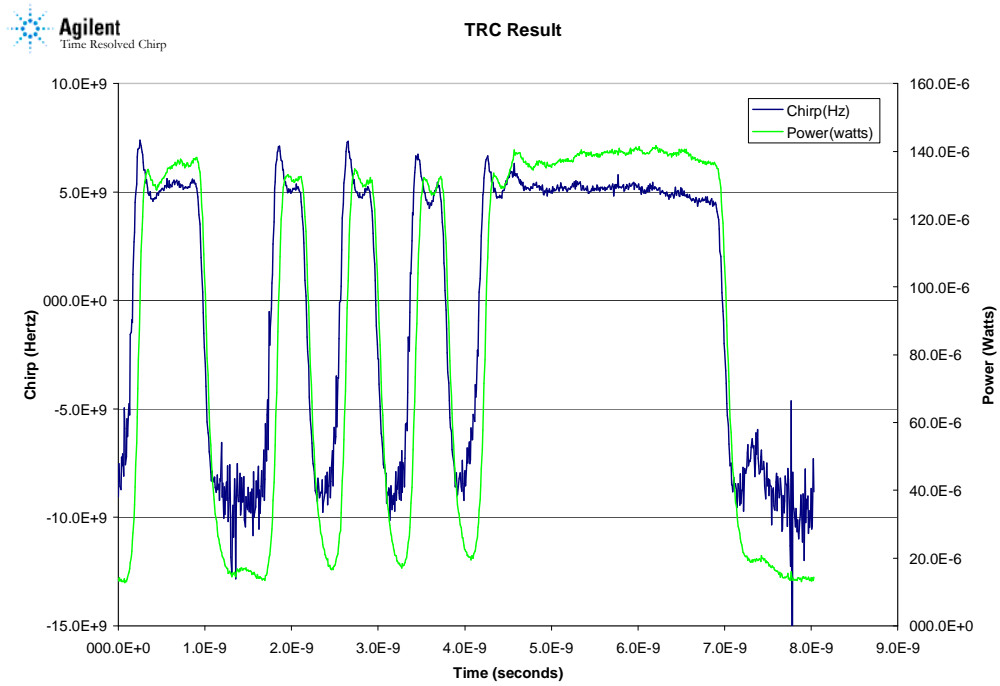


Fig. 5.5 The chirp and corresponding power measured on the QD DFB biased at 20 mA. The chirp at '0' levels are noisier than '1' levels as a result of the increased measurement error for lower power.

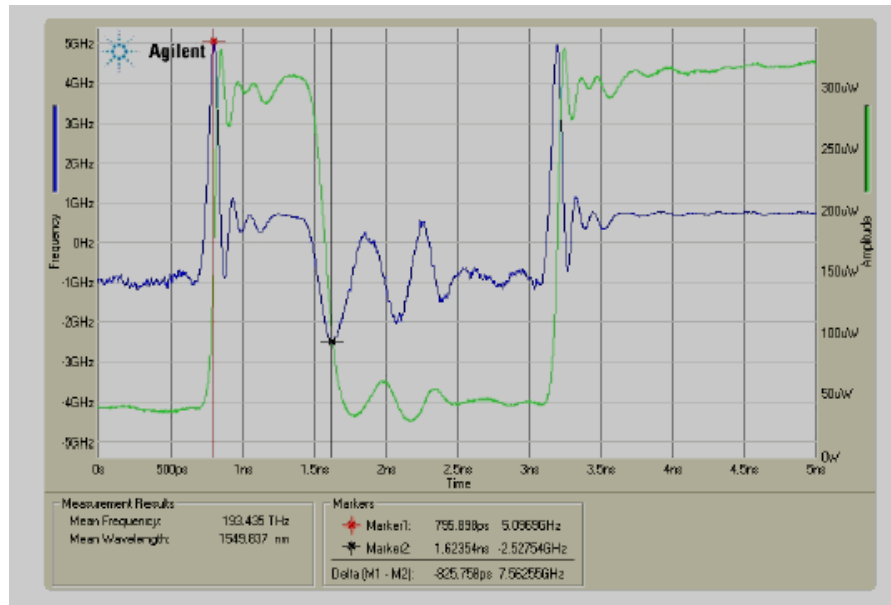


Fig. 5.6 TRC measurements of the chirp and power of a QW DFB as given in ref. [121].

For an extinction ratio of 10 dB, we have  $(S+\Delta S)/(S-\Delta S)=10$ , then  $\Delta S/S=9/11$ . The output power is proportional to the injection current and thus the voltage, so  $V_{pp} \propto (I-I_{th})$ . Since the adiabatic chirp dominates the average chirp, the average chirp  $\propto \Delta S \propto S \propto (I-I_{th})$  for a fixed extinction ratio. The linear dependence of the  $V_{pp}$  and average chirp on the DC bias is shown in Fig. 5.7. The value of the chirp-per- $V_{pp}$  is  $\sim 13$  MHz/mV. Considering the 20 Ohms of resistance of the QD DFB, the change in the chirp with current is estimated 260 MHz/mA, comparable to the typical value of QW lasers [122].

The shift of the average optical frequency of the modulated light relative to the unmodulated one is given in Fig. 5.8. The shift of the center frequency is -1.4 MHz/mV, approximately 10% of the total chirp. This shift of the center frequency could be related to the higher order harmonic response of the device to the large signal modulation, including the non-perfect linearity on the L-I and I-V curves and the higher order behaviors of gain compression.

The effective of alpha parameter, defined as  $\alpha(I+\epsilon_P P)$  in Eqn. 5.5, is given in Fig. 5.9. The curve fitting results show that the alpha is  $\sim 4$  at threshold and doubles once the output power is increased by  $\sim 2$  mW. This is consistent with the linewidth re-broadening that occurs at about 2-4 mW output in the QD DFBs discussed in Chapter 2.

As a conclusion of this section, the chirp of the QD DFB is measured to be 13 MHz/mV with a shift of the center frequency of about -1.3 MHz /mV for a fixed extinction ratio of 10 dB. These results show that these QD DFBs have a similar chirp performance as typical QW DFBs for real communication systems. The alpha at threshold is determined to be around 4 and doubles when the output power reaches 2 mW.

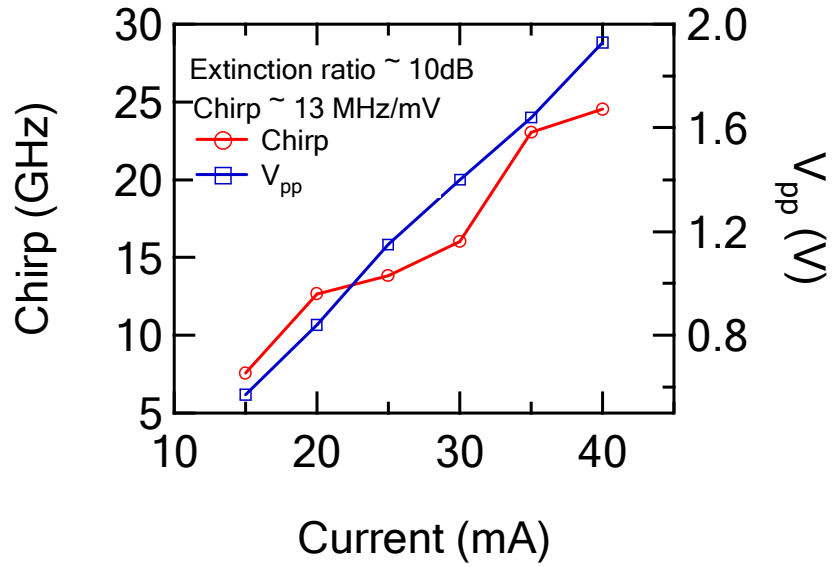


Fig. 5.7 The average chirp and the peak-to-peak modulation voltage under different DC biases of the QD DFBs with the extinction ratio kept around 10 dB.

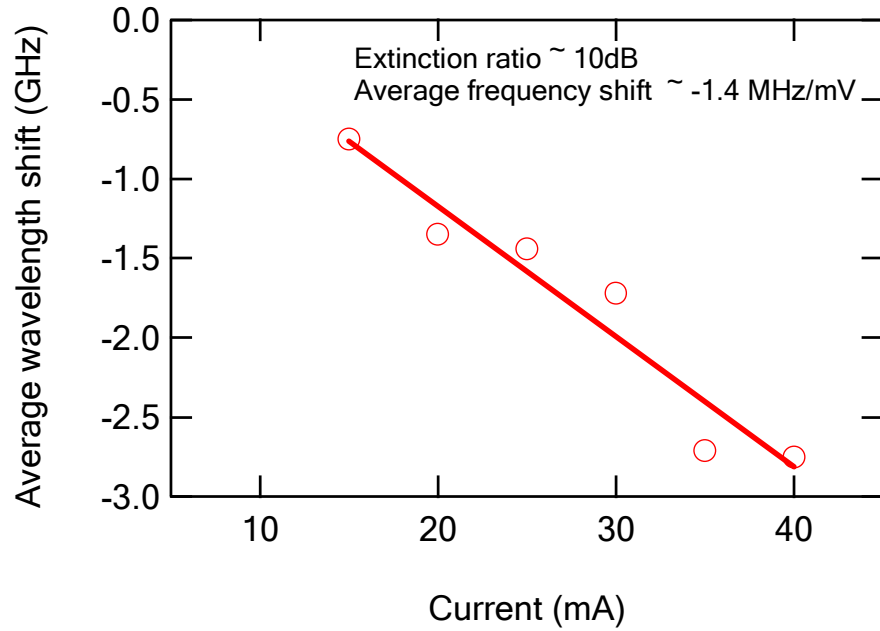


Fig. 5.8 The shift between the center frequencies of the modulated and un-modulated output from the QD DFB as a function of current with the extinction ratio fixed at  $\sim 10$  dB.

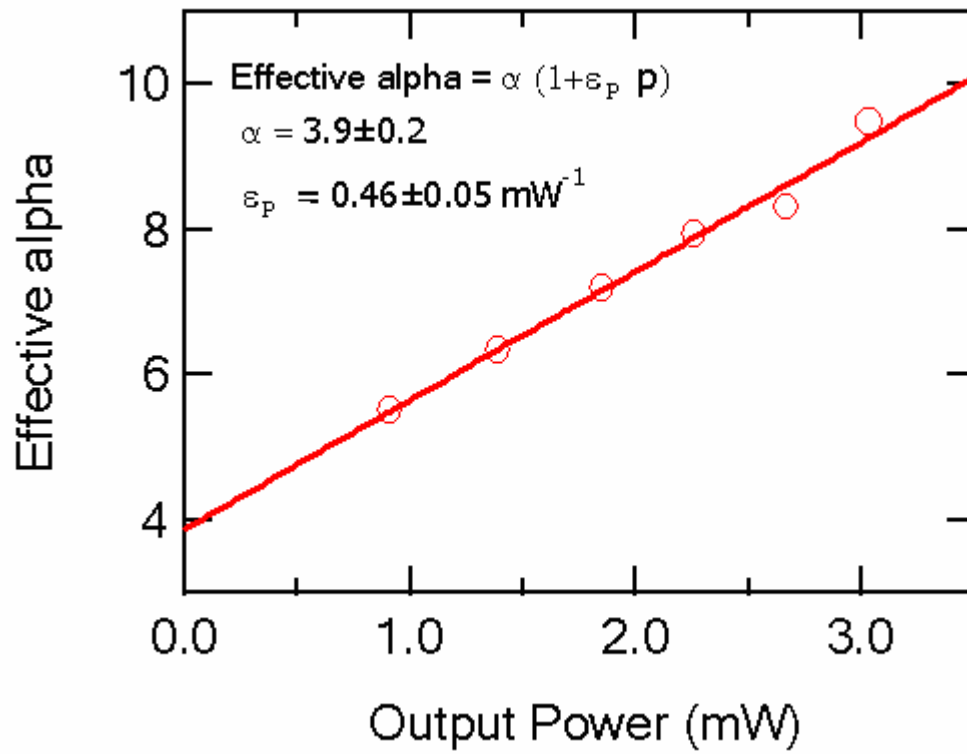


Fig. 5.9 The measured effective alpha and its dependence on the output power of the QD DFB under modulation with the extinction ratio fixed at  $\sim 10$  dB.

#### 5.4. Chirp with a fixed modulation depth $V_{pp}$

In the previous section, a large signal modulation was used and the alpha measured was the average over a large range of DC bias. To study the relationship of the dependence of alpha on the output power, smaller modulation is needed. In this part of experiment, the time resolved chirp is measured under different biases with the peak-to-peak voltage,  $V_{pp}$ , of the modulation fixed at 250mV, corresponding to a current modulation with a peak-to-peak amplitude of about 12 mA. Therefore, the alpha measured here will be an average value over the (-6mA, 6mA) vicinity of the bias. The experimental results are given in Table 5.2 with the same definitions for the effective alpha, average chirp and frequency shift given in Table 5.1.

Fig. 5.10 gives the measured chirps at 15 mA, 25 mA and 35 mA with their curve-fits. Compared to the chirp under large modulation discussed in the previous section, the adiabatic chirp still dominates the overall chirp while the transient chirp spikes are further weakened because of the smaller modulation depth. The curve fittings based on Eqn. (5.3) are quite good as demonstrated in Fig. 5.10.

The effective alpha is plotted in Fig. 5.10. The alpha factor at threshold is found to be  $2.6 \pm 0.4$  and  $\epsilon_p$   $0.7 \pm 0.2$  mW<sup>-1</sup> by curve-fitting the measured effective alpha as a linear function of the output power based on Eqn. 5.5. The alpha factor is lower and  $\epsilon_p$  is larger than the values we got from the modulation with extinction ratio fixed at 10 dB. This can be explained by the fact that the measured alpha and  $\epsilon_p$  are averaged over a smaller range of the DC bias and that their dependence on the output power is significant. The alpha factor without the gain compression effects is close to the results in Ref. [16] and doubles when the output power is 1-2 mWs.

Fig. 5.12 gives the gain compression coefficient of the QD DFBs. The curve-fitting error bar comes from the large signal modulation and the sensitivity of the derivative  $dP/dt$  to the measurement noise. The gain compression factor is estimated to be  $0.2 \pm 0.1 \text{ mW}^{-1}$  from the curve-fitting based on Eqn. 5.3. Therefore, roughly speaking, the gain compression becomes significant for an output power of 7 mW, comparable to the 2-5 mW estimated from the linewidth and high-speed experiments, and the gain compression photon density,  $\epsilon_s$ , is still one order of magnitude lower than the typical value of QWs. However, the gain compression coefficient  $\epsilon_p = 0.2 \pm 0.1 \text{ mW}^{-1}$  determined here is smaller than the value of  $\epsilon_p = 0.7 \pm 0.2 \text{ mW}^{-1}$  determined from the dependence of alpha factor on the output power. This could be explained the enhancement of the gain compression by the gain saturation with the carrier density in QD devices. Since the homogenous broadening is 10 - 20 meV [70], three times narrower than the inhomogeneous broadening, spectral hole burning will occur in QDs at elevated powers. As the gain at the lasing wavelength is clamped to the threshold value, the consequence of the spectral hole burning is the increase in the carrier density at the energy levels outside of the homogeneous broadening of lasing wavelength, especially the higher excited states, as shown in Fig. 5.13. Therefore, the magnitude of the alpha factor in QDs is further increased as a result of the global distortion of the gain spectrum in addition to the local one purely from the spectral hole burning. Since the homogeneous broadening dominates the gain spectrum of typical QW lasers, all the carriers behave homogeneously [123]. In this case, the increase of the effective alpha in QWs is dominantly from the gain compression with the overall profile of carrier distribution considered to be clamped at threshold as presented in Fig. 5.14. The detailed model describing the alpha dependence



on the output power in QD lasers is given Appendix 1 to explain the effects observed here.

Fig. 5.16 shows the decrease of the chirp with the increase of the DC bias. Since the adiabatic chirp dominates the average chirp, therefore

$$\begin{aligned} \text{Average chirp} &\propto \frac{\varepsilon(S + \Delta S)G_{th}}{1 + \varepsilon(S + \Delta S)} - \frac{\varepsilon(S - \Delta S)G_{th}}{1 + \varepsilon(S - \Delta S)} \\ &\propto \frac{2\Delta S}{(1 + \varepsilon S)^2 - (\varepsilon\Delta S)^2} \end{aligned}$$

$\Delta S$  can be approximated constant since the  $V_{pp}$  is fixed to 0.25mV. Therefore, the average chirp will decrease with the  $S$  or pump current increase. The change of chirp per mV modulation is roughly 17 MHz /mV, slightly larger than the 13 MHz /mV in the cases of modulation with the extinction ratio fixed, which could be explained by the nonlinearity of the V-I curve of the QD DFB.

Bias (mA)	Power (mW)	$V_{pp}$ (V)	<i>Effective Alpha</i>	<i>Avg chirp (GHz)</i>	<i>freq_shift (GHz)</i>
15	0.912	0.25	4.9	4.81	-0.57
20	1.39	0.25	6	4.58	-0.57
25	1.85	0.25	7.1	4.45	-0.56
30	2.26	0.25	9.1	4.20	-0.52
35	2.67	0.25	10.1	4.10	-0.53
40	3.04	0.25	10.5	3.77	-0.50

Table 5-2. TRC results of the QD DFB with a fixed peak-to-peak voltage modulation depth.

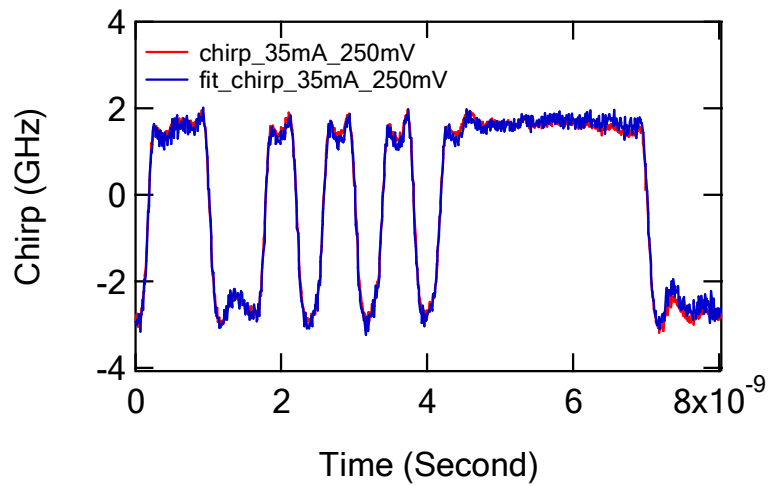
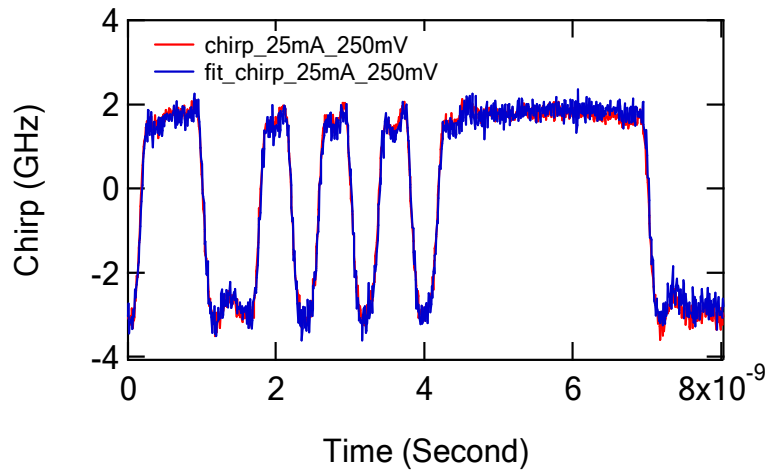
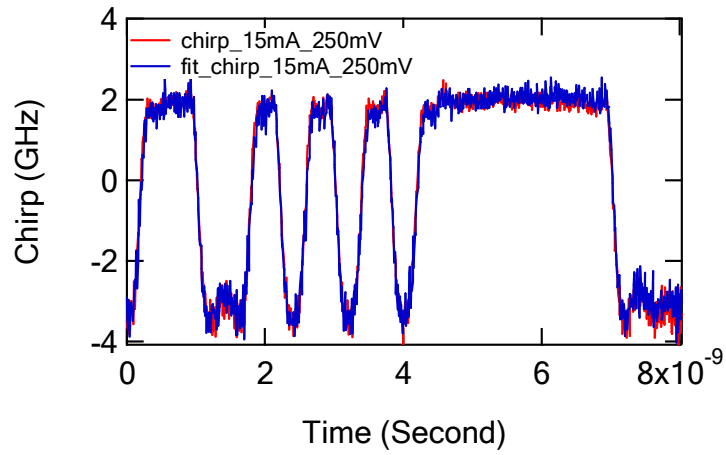


Fig. 5.10 The measured and curve-fitted chirps of the QD DFB under 15 mA, 20 mA and 35 mA DC biases with a peak-to-peak modulation voltage fixed at 250mV.

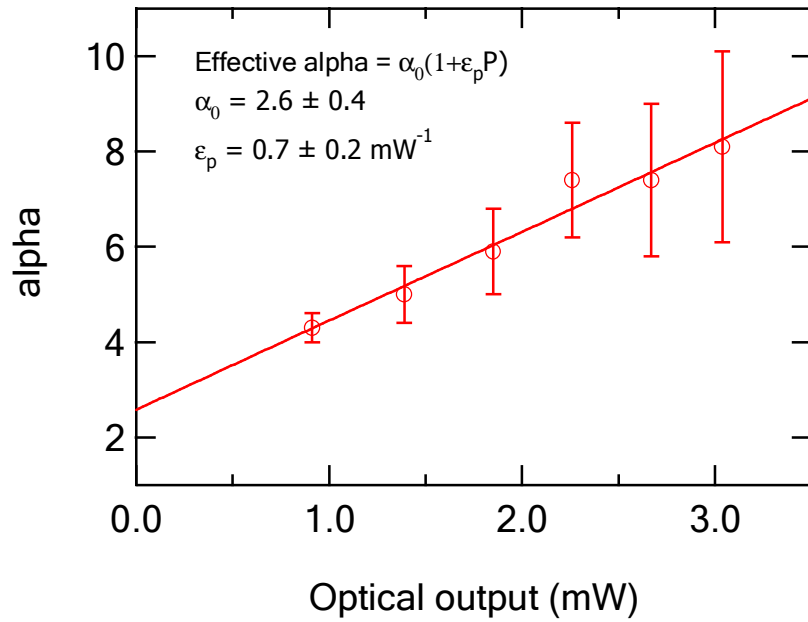


Fig. 5.11 The effective alpha and its dependence on the output power measured in the QD DFB.

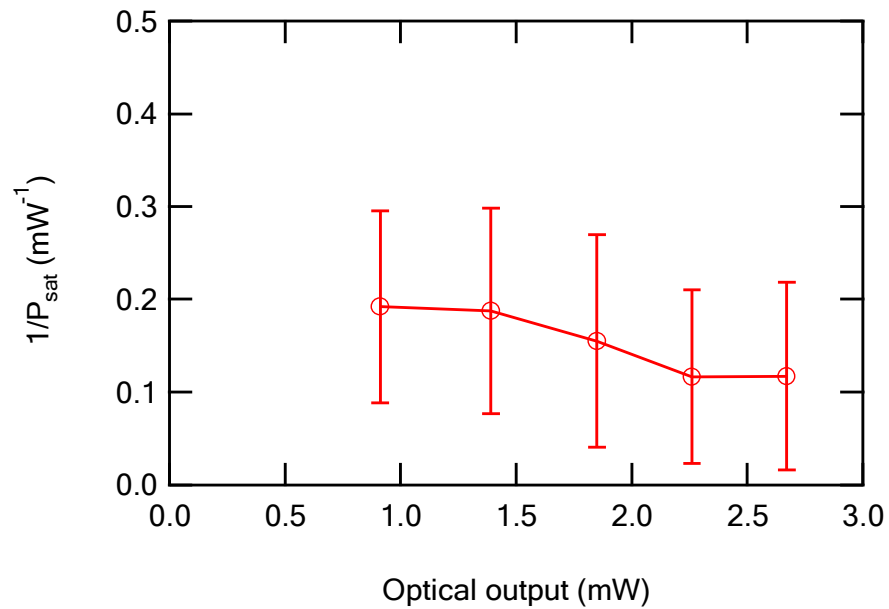


Fig. 5.12 The gain compression coefficients at different DC output powers of the QD DFB.

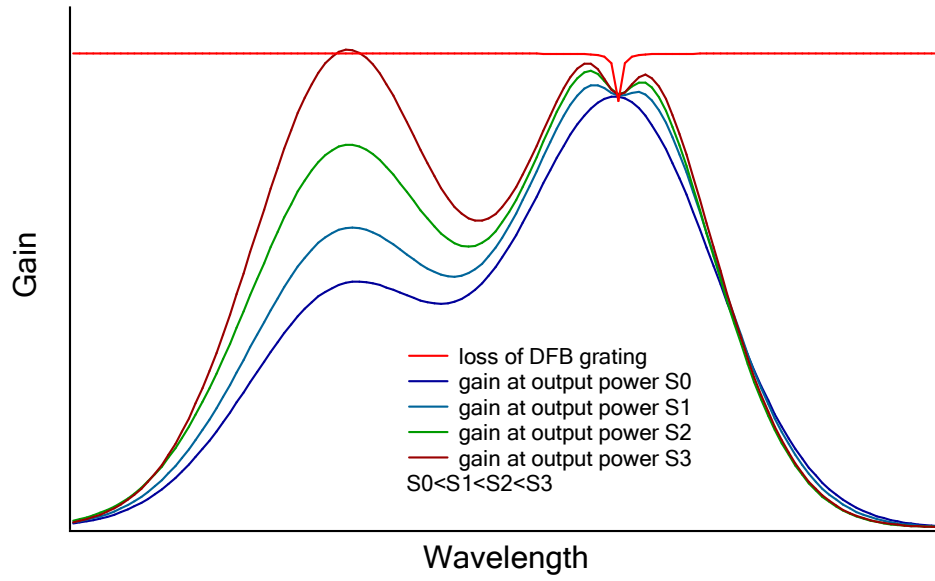


Fig. 5.13 The distortion of the gain spectrum of QD gain media due to the inhomogeneous broadening and spectral hole burning effects.

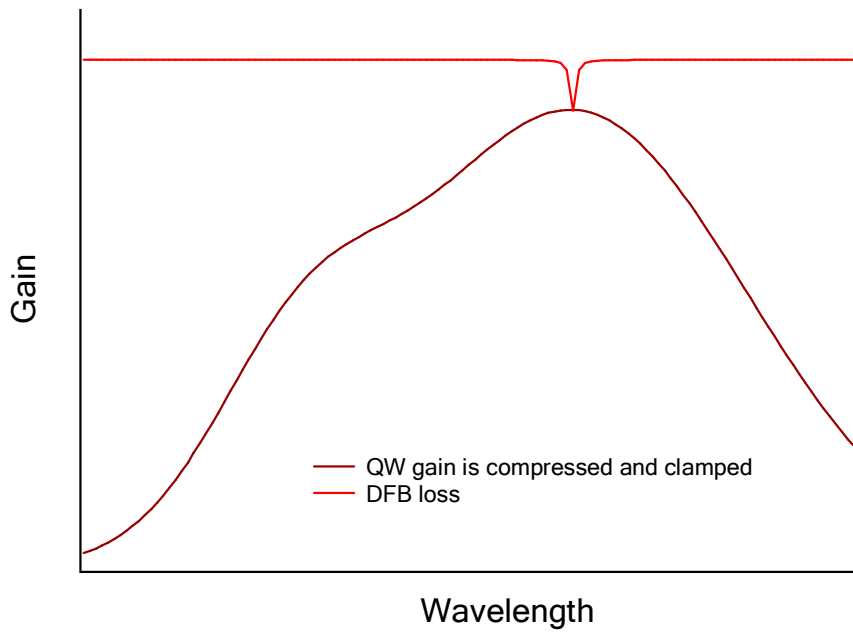


Fig. 5.14 The overall profile of QW homogeneously-broadened gain spectrum is clamped and kept unchanged even under a strong gain compression.

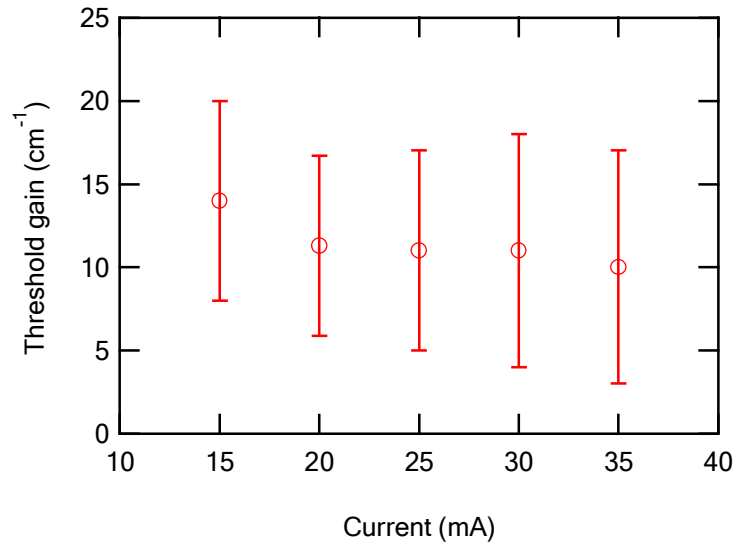


Fig. 5.15 The threshold gain of the QD DFB from the curve-fitting of the chirp measured at different biases.

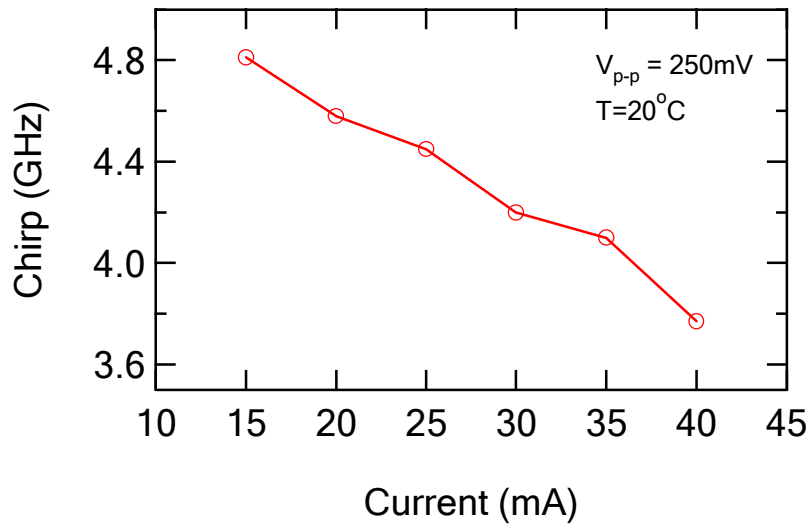


Fig. 5.16 The average chirp of the QD DFB with a fixed  $V_{pp}=0.25\text{V}$  under different DC current biases.

## **Chapter Six. CONCLUSIONS AND SUGGESTIONS**

### **FOR FUTURE WORK**

In this dissertation, the dynamic properties of QD DFBs are studied, including high-speed modulation, linewidth, external feedback effects and chirp performance. The above-threshold linewidth enhancement factor and strong gain compression effect in QDs are characterized and discussed.

Firstly, the optical response function of the QD DFB under direct modulation is measured. The modulation bandwidth is found to be saturated at 5 GHz. The possible limiting factors for the bandwidth are investigated, including the K-factor, effective carrier transport time and gain compression. Strong gain compression is found to be the limiting factor and the effective gain compression coefficient is determined to be  $4.3 \pm 0.4 \times 10^{-16} \text{ cm}^{-3}$ , which is about 30 times higher than the typical value in QWs. The suggestion to overcome this problem is to avoid the gain saturation by increasing the maximum gain of the QD active region. A novel analytical expression is derived to account for the enhancement of the nonlinear gain coefficient due to this hard gain saturation in QDs.

Secondly, the linewidth of the QD DFBs is studied and compared to that of a QW DFB. The linewidth-power product of 1.2 MHz-mW is found in QD DFBs, more than one order of magnitude lower than the typical value in QW DFBs. The figure of merit for the narrow linewidth,  $n_{sp}(1+\alpha^2)$ , is found to be 3-4 times lower (you never said this back in Chapter 3) in QDs than QWs given the same threshold gain. At the same time, the linewidth rebroadening and floor are found in the QD DFBs at relative low output powers,

from which the effective gain compression factor is estimated to be  $4-8 \times 10^{-16} \text{ cm}^{-3}$ . The effects of gain offset on the linewidth performance are also investigated and compared to Agrawal's theory.

Thirdly, the effects of external feedback on the QD DFB are compared to that of a typical QW DFB. The optical spectrum is shown to be unchanged within the 0.06nm resolution of the optical spectrum analyzer, while a 50% broadening of the 20-dB width in the spectrum of the QW DFB is present. More precise measurement of the linewidth of the QD DFB shows the critical external feedback level for coherence collapse is found to be -14 dB, about 8 dB improvement from QW DFBs and good enough for the isolator-free operation in 10 Gbps Ethernet applications. The relative intensity noise in the QD DFB under -14 dB external feedback is found to be 7 dB lower than that of the QW DFB with the same output power of 6 mW. Under 2.5 Gbps digital modulation, although the degradation of root-mean-square jitter behaves similarly in both QD and QW DFB, the SNR degradation of QD starts to degrade at -30 dB, about 20 dB improvement from the QW DFB. The origins for these improved resistance to external feedback in the QD DFB stem from the strong damping oscillation, HR coating and the loss coupled grating in the studied QD DFBs.

Finally, the chirp of a QD DFB is studied by the time-resolved-chirp measurement. In the first part of this experiment, the extinction ratio of the digital modulation is fixed around 10 dB. The chirp strength is found to be 13 MHz/mV, compared to the value in typical QW DFBs, with a center frequency shift about -1.4 MHz/mV. The effective alpha parameter is measured to be  $\alpha=3.9\pm0.2$  at threshold and increase with the output power,  $P$ , as  $\alpha_0(1+\epsilon_p P)$  with  $\epsilon_p=0.46\pm0.05 \text{ mW}^{-1}$ , corresponding to a effective gain compression

coefficient of  $6-8 \times 10^{-16} \text{ cm}^{-3}$ , more than one order of magnitude higher than that in QWs. In the second part of this experiment, with smaller modulation depth, the  $\alpha$  is measured to be  $\alpha_0=2.6\pm0.5$  at threshold and  $\epsilon_p= 0.7\pm0.2 \text{ mW}^{-1}$ . The gain compression coefficient,  $\epsilon_p$ , determined from the curve-fitting parameter in the adiabatic chirp term with the same TRC data, however, shows a value of  $0.2\pm0.1 \text{ mW}^{-1}$ , corresponding to  $1.6-3.2 \times 10^{-16} \text{ cm}^{-3}$ , still one order of magnitude higher than the typical value of  $10^{-17} \text{ cm}^{-3}$  of QWs. The discrepancy between  $\epsilon_\alpha$  and  $\epsilon$  can be explained by the gain saturation and the resulting carrier accumulation in the excited states of the QDs.

About the future work on QDs, the topic most directly related to this dissertation is to reduce the gain compression and gain saturation effects in QDs. Large maximum gain is preferred since it can keep the operation point of QD lasers away from the gain saturation and less carriers in the excited states. This will make the QD more ideal and give better performance in temperature, high speed and frequency stability.

Another promising application of QDs is mode-locked lasers. Although significant results always have been obtained by Zia Laser, Inc. and X. D. Huang etc., the potential of QDs for ultrashort pulses are not fully explored. The wide gain spectrum, strong gain/loss saturation indicates sub-ps pulses. The dispersion of the gain, loss and reflective index needs to be understood first for a better design. The group index dispersion can be measured by the variation of the FP mode spacing and compensated by an external chirped Bragg grating cavity, so that the intrinsic properties of the QD mode-locked devices can be investigated. The other basic physics here is whether or not the fast and slow carrier dynamics in QDs discussed in Chapter 1 help to stabilize the quantum dot



mode locked lasers and lead to less instability towards self-pulsation and Q-switching mode-locking. and reduced amplitude and phase noise. It is also notable that QD semiconductor saturable absorber mirror (SESAM) could be important for the ultrafast pulse generation in solid state lasers, considering the fast and slow carrier dynamics in QDs. Undistorted 18 dB amplification of femto-second pulses have been shown in QD amplifiers [32].

Very little knowledge about the nonlinear optics properties in QDs is known by now. The speed of the nonlinearity in QDs is much faster than the QWs due to the same reason for the high speed QD optical amplifiers discussed in Chapter 1. Although the IR  $\chi^{(3)}/g$  is measured by a Japanese group to be comparable in QDs and QWs, theoretically  $\chi^{(3)}$  is more enhanced in QDs. The difficulty of the measurement is the small confinement factor, which also effectively limits the application of QDs in nonlinear optics. The application of the QDs in mid-IR nonlinear optics seems interesting. By analog to the strong second harmonic generation by the resonant transition between the mini-band in quantum cascade lasers, the energy-level structure of QDs gives similar physics.

Besides these, the importance of the QD crystal growth can never be over-emphasized. To get more uniform dots and more gain, as well as QDs at various wavelengths on different substrates, are essential for the future of the self-assembled QDs discussed in this dissertation.

## **Appendix A. GAIN COMPRESSION AND GAIN SATURATION IN QD LASERS**

Unlike QWs, QDs are more subject to gain saturation due to a limited number of energy states. The small confinement factor and thus the small material gain usually force QD lasers to be operated near the gain saturation regime. The saturation of the ground-state gain inevitably leads to the decrease of the differential gain at the lasing wavelength and the carrier filling in the excited states in QDs. On the other hand, since gain compression is strong in QDs, gain saturation can be aggravated when the laser is above threshold. In this section, the effects of the gain saturation and gain compression on the dynamics of QD lasers will be derived.

The rate equation of the photon density in a laser is given as

$$\frac{dS}{dt} = \left( \frac{g}{1 + \epsilon_s S} - g_{th} \right) S + R_{sp} \quad (\text{A1.1})$$

where the  $S$  is the photon density,  $\epsilon_s$  is the gain compression coefficient related to  $S$ ,  $g$  is the gain,  $g_{th}$  is the threshold gain and  $R_{sp}$  is the spontaneous emission rate. For a steady state well above the threshold, the pure gain at the lasing wavelength should be equal to the threshold loss,

$$g = g_{th} (1 + \epsilon_s S) \equiv g_{th} (1 + \epsilon_P P) \quad (\text{A1.2})$$

with  $P$  the output power and  $\epsilon$  the gain compression coefficient related to the output power. Eqn. (A1.2) predicts that higher gain is required for higher output power.

Eqn. (A1.3) is used to describe the gain of QD media for its simplicity,.

$$g = g_{\max} \left[ 1 - e^{-\ln 2 \left( \frac{N}{N_{tr}} - 1 \right)} \right] \quad (\text{A1.3})$$

where the  $g_{\max}$  is the maximum gain for the ground-state lasing,  $N$  is the carrier density,  $N_{tr}$  the transparency carrier density and the factor of  $\ln 2$  is used for the equality of the maximum gain and maximum loss in QD gain media. Fig. A1.1 plots the gain versus carrier density normalized to the transparency carrier density in QDs.

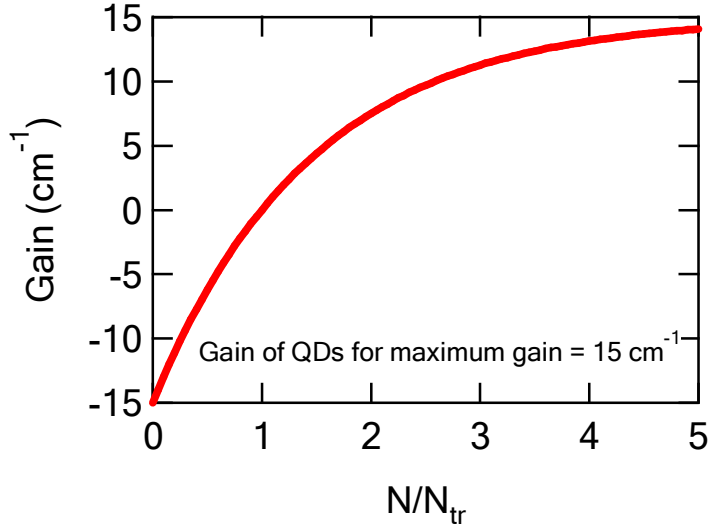


Fig. A1.1 The gain vs. normalized carrier density in a QD gain medium. The maximum ground-state gain is set to  $15 \text{ cm}^{-1}$ , which is typical in the devices studied in this dissertation.

When the laser is above threshold, Eqn. (A1.2) and (1.3) give the expression of the differential gain at the ground state:

$$a \equiv \frac{dg}{dN} = \frac{\ln 2}{N_{tr}} (g_{\max} - g) = \frac{\ln 2}{N_{tr}} (g_{\max} - (1 + \epsilon_P P) g_{th}) = a_0 \left( 1 - \frac{g_{th}}{g_{\max} - g_{th}} \epsilon_P P \right) \quad (\text{A1.4})$$

where the  $a_0$  is the differential gain at threshold.

The decrease of the differential gain given by Eqn. (A1.4) is directly related to the response of the QD devices under external modulation. The resonance frequency is give as:

$$\omega_R^2 = \frac{v_g g_{th} a P}{1 + \epsilon_p P} \approx \frac{v_g g_{th} a_0 P}{1 + \frac{g_{max}}{g_{max} - g_{th}} \epsilon_p P} \quad (\text{A1.5})$$

where the  $v_g$  is the group velocity. Eqn. (1.7) indicates that the gain compression effect is enhanced by the gain saturation by

$$\epsilon_{eff} = \frac{g_{max}}{g_{max} - g_{th}} \epsilon_p \quad (\text{A1.6})$$

For typical QD DFBs discussed in this dissertation,  $g_{max}$  and  $g_{th}$  are about  $15 \text{ cm}^{-1}$  and  $12 \text{ cm}^{-1}$  respectively. The gain compression effect is enhanced by a factor 5 in those devices and causes a severe limitation on the modulation bandwidth. It is also suggested by Eqn. (1.8) that larger maximum gain could improve the bandwidth by a factor of 2.

Another consequence of Eqn. (1.8) is the dependence of the alpha parameter on the output power due to the gain compression. Typically, people describe the gain compression causing an increase of the effective alpha parameter by [117]

$$\alpha_{eff} = \alpha(1 + \epsilon_p P) \quad (\text{A1.7})$$


where  $\alpha_{eff}$  is the effective linewidth enhancement factor and  $\alpha_0$  is the alpha parameter clamped at threshold. Since the refractive index at the lasing wavelength can be affected by the carriers in energy states far away from the resonance frequency, a clamp of the  $\alpha_0$  means a fix of a wide range of spectrum, which is not the case for QDs. As shown in Fig. 5.13, although the net gain at the ground state is clamped at threshold, the carrier density

at the excited states still keeps growing due to the spectral hole burning. Experimentally, lasing at the excited states is observed in the QD devices under high injection. Therefore, Eqn (A1.7) is not applicable to the gain compression effects in QDs. To model the effective alpha parameter in QDs, we simply divide the energy levels into ground states and excited states. The gain compression occurs locally within the homogeneous broadening of the ground states. The index change at the lasing wavelength can be caused by both of the gain variation at the ground states and excited states.


$$\delta n = \alpha_e \delta g_e + \alpha_g \delta g_g = (\alpha_e \frac{a_e}{a_g} + \alpha_g) \delta g_g \equiv \alpha \delta g \quad (\text{A1.8})$$

where  $\delta n$  and  $\delta g_g$  are the changes of the gain and refractive index at the ground state,  $\alpha$  is basically the alpha parameter which is measured from the device,  $a_e$  and  $a_g$  are the differential gains at excited and ground states respectively,  $\alpha_e$  describes the change of the ground-state index caused by the excited state gain and  $\alpha_g$  describes the ground-state index change caused by the ground-state gain variation. When the laser is above threshold,  $\alpha_g$  will increase as  $\alpha_g(1+\epsilon P)$  since it is from the energy levels within the homogeneous broadening. By putting Eqn. (A1.4) and (A1.7) into Eqn. (A1.8), we will have the dependence of the alpha parameter on the optical power as

$$\alpha(P) = \alpha_e \frac{a_e}{a_0 \left(1 - \frac{g_{th}}{g_{max} - g_{th}} \epsilon_p P\right)} + \alpha_g (1 + \epsilon_p P) \quad (\text{A1.9})$$



Filling of excited states



Ground-state gain compression

The decrease of differential gain effectively means more carriers in the excited states. Therefore, Eqn. (A1.9) includes the effects of the gain compression at the ground states

and the carrier filling of the excited states as illustrated in Fig. 5.13. Further simplification leads to:

$$\alpha(P) = \alpha_{th} \left( 1 + \frac{\frac{\alpha_e a_e}{a_0} \frac{g_{th}}{g_{max} - g_{th}} (1 + \epsilon_p P) + \alpha_g}{\frac{\alpha_e a_e}{a_0} + \alpha_g} \epsilon_p P \right) \quad (A1.10)$$

In the case of strong gain saturation or  $\alpha_g=0$  when the DFB mode is close to the ground-state gain peak, Eqn. (1.12) can be further simplified into:

$$\alpha(P) = \frac{\alpha_{th}}{\left( 1 - \frac{g_{th}}{g_{max} - g_{th}} \epsilon_p P \right)} \quad (A1.11)$$

indicating the dependence of the alpha parameter on the optical power is enhanced by a factor of  $g_{th}/(g_{max}-g_{th})$ . Eqn. (A1.10) also predicts that the increase of alpha parameter with the output power can be reduced if the threshold gain is less than a half of the maximum gain. Therefore, a larger maximum gain is also essential for a lower alpha parameter in QD gain media and the linewidth and frequency noise performance of the QD devices.

## **Appendix B. NON-DEGENERATE FOUR-WAVE MIXING IN QUANTUM DOT DISTRIBUTED FEEDBACK LASERS**

*Abstract:* We present wavelength conversion using non-degenerate four-wave-mixing (FWM) in loss coupled distributed feedback lasers (DFB) based on InAs/AlGaAs quantum dots (QD). The conversion efficiency is measured for to be -15dB to -30dB, with a cavity resonance bandwidth about 9GHz, for a signal-pump detuning range from 0.33nm to 8nm.

*Introduction:* Four-wave mixing (FWM) is a promising technique for wavelength conversion in communication systems [124]. Typically FWMs in semiconductors are realized in semiconductor optical amplifiers (SOA) and require external pumping sources [124]. Single mode laser is used as simplified and integrated alternative with its counter-propagating lasing modes functioning as internal pumps [125-127]. Considering the uniformity of the wavelength conversion, FWMs in gain or loss coupled DFBs suffer less from stop-band effects but more from the strong cavity resonance compared to those in index coupled DFBs [128]. In real communication systems, fortunately, wavelength channels are discrete and wavelength conversion can be enhanced by cavity resonance when the wavelength channels match the cavity modes. On the other hand, QDs have some fundamental advantages over quantum wells (QW) for nonlinear optics applications considering the  $\chi^{(3)}$  enhancement by the quantum confinement in more dimensions [128,129], ultrafast carrier recovery [47] and wide gain spectrum [50]. Though FWM's in quantum dot (QD) SOAs have been reported by different groups [130,131], no FWM

experiment in QD DFBs has yet been published. This letter reports the FWM and its cavity effects in a laterally loss-coupled (LLC) QD DFB.

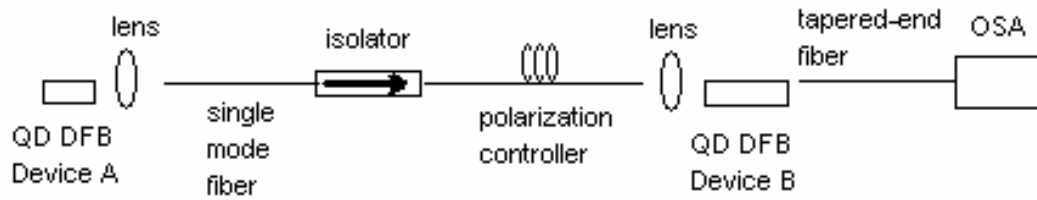


Fig. A2. 1. The experimental setup for four-wave mixing in a laterally-loss-coupled QD DFB (Device B).

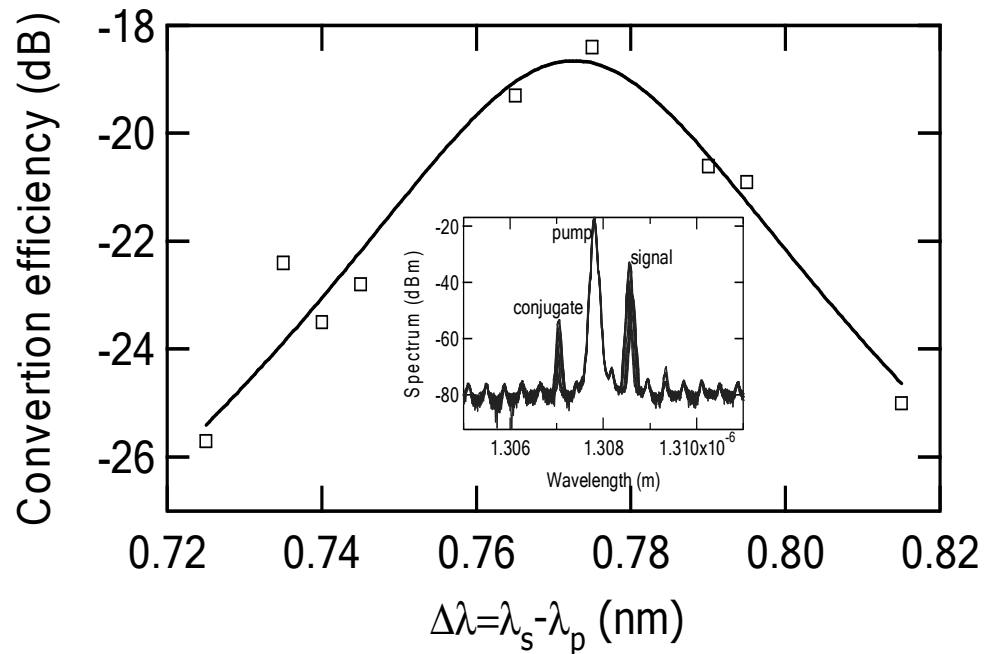


Fig.A2.2 Cavity resonance effect on the FWM wavelength conversion. The inset is the FWM spectrum with the pump ( $\lambda_p$ ), nine fine-tuned signals ( $\lambda_s$ ) and corresponding conjugate wavelengths.



*Experimental setup and QD DFB characteristics:* The experimental setup is presented in Fig. 1. Two LLC QD DFBs, Device *A* and *B*, are used as a signal source and a FWM nonlinear medium respectively. Two cascaded isolators and angle-polished single mode fibers are employed to avoid the external feedback into Device *A*. A fiber polarization controller is used to match the polarizations of the signal from device *A* and the DFB mode of device *B*. The FWM outputs are collected by a tapered-end fiber followed by an optical spectrum analyzer (OSA). The QD DFB is fabricated on an InAs/InGaAs QDs structure with a first order grating deposited laterally to the etched waveguide ridge. Except that the DFB mode is selectively enhanced by the grating implemented in the devices, the QD LLC-DFB spectrum shows cavity-resonance bumps (cavity modes) similar to typical Fabri-Parot amplifiers. Based on the amplitude variation of the cavity modes of device *B*, we find a weak stop-band about 4nm wide on the shorter-wavelength side of the DFB mode. This could be due to the index undulation associated with the loss grating in the DFBs. The details of the material growth, processing and performance of the laterally loss coupled QD DFBs can be found in previous publications [57]. In this experiment, both devices are biased above threshold and have a side-mode-suppression-ratio (SMSR) better than 50dB. Device *A* can be wavelength-tuned for about 8nm by different control sets of heat-sink temperature and pump current. Device *B* is asymmetrically high-reflectivity (HR) coated on the facets of the 600 $\mu$ m cavity. During our measurements, the wavelength and output power of device *B* is fixed. Knowing the output power and facet reflectivity of device *B*, we estimate the pump power for the FWM inside the cavity to be about 36mW at 1307nm.

*Results and discussion:* As shown in the inset of fig.2, a strong cavity effect on the wavelength conversion is observed when we tune the signal wavelength around the second cavity mode counted from the DFB mode. The conversion efficiency is plotted as function of the detuning from the pump in fig.2 with a maximum at the wavelength of the cavity mode. To estimate the 3dB bandwidth due to the cavity resonance, we curve-fit the data to a Lorentzian function and the full width of the half maximum (FWHM) is found to be 0.05 nm, corresponding to a conversion bandwidth about 9GHz at 1307nm.

We also investigate the FWM in device B over a wider spectrum range as shown in fig.3. For each data point, the wavelength of signal is carefully tuned so that the FWM conversion efficiency is maximized by lining up the conjugate beam with the cavity resonances. The locally maximized conversion efficiency varies from -14 dB to -30 dB with the detuning increases from 0.33 nm to 8nm, that is, from 60 GHz to 1.4 THz, with an inside-cavity pump power fixed at 36mA in device *B*. These efficiencies are comparable to the reported data in an index-coupled QW DFB with much higher carrier density [126]. As the conversion efficiency is plotted in fig.4 in log scales, we find two different regimes of the slope of the conversion efficiency relative to the signal-pump detuning: for 0.3nm to 3.3nm the slope is about -1.2 while for 4nm to 8nm about -2.4. Theoretically, the slope should close to -2 since  $|\chi^{(3)}|^2$  is a Lorentzian function of frequency detuning. In our case, cavity resonance should be taken into account. Applying the Haiki-Pioli technique [132] to the lasing spectrum of device *B*, we find that the net round-trip gain, defined as  $r_1 r_2 \exp(2gL)$  with  $g$  the gain,  $L$  the cavity length,  $r_1$  and  $r_2$  the reflectivities of the facets, has a positive slope in the regime from 0.3nm to 3.3nm and a negative one from 4nm to 8nm. Larger gain indicates a stronger cavity enhancement and

this explains the slope difference in fig.3. This non-constant distribution of the net gain in the device is resultant from the stop-band (about 4nm wide as observed in lasing spectrum) and also could from the spectrum hole burning effect which is believed to be significant in QDs [79]. The discontinuation around 4nm could be attributed to the crossing-over of the stop band.

*Conclusion:* The FWM in a quantum dot LLC DFB laser at 1307 nm is reported in this paper. The conversion efficiency is found to change from -14dB to -30dB for a detuning range from 60 GHz to 1.4 THz. The conversion efficiency is found proportional to  $(\Delta\lambda)^{-1.2}$  in the detune range of 0.3nm to 3.3 nm while  $(\Delta\lambda)^{-2.4}$  of 4nm to 8nm, which can be contributed to the cavity resonance and the net gain non-uniformity due to the residual stop-band from the loss grating and probably the spectrum hole burning effect in the QD DFB. Cavity enhancement of the wavelength conversion is characterized with a bandwidth about 9GHz.

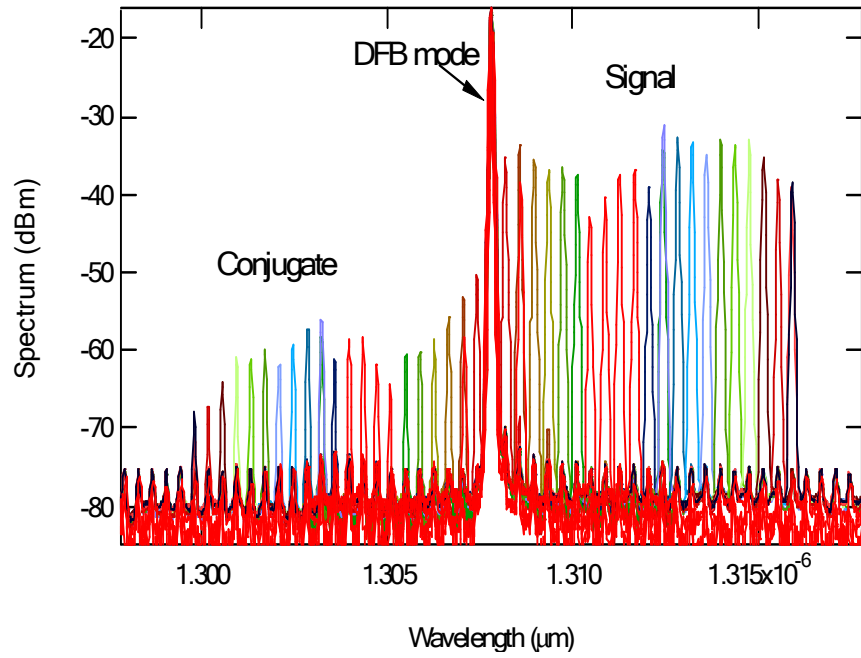


Fig. A2. 3. A plot of the DFB spectrum with twenty signals detuned differently from the pump wavelength. The FWM efficiency is maximized for each detuning by lining up the conjugate beam with the cavity mode.

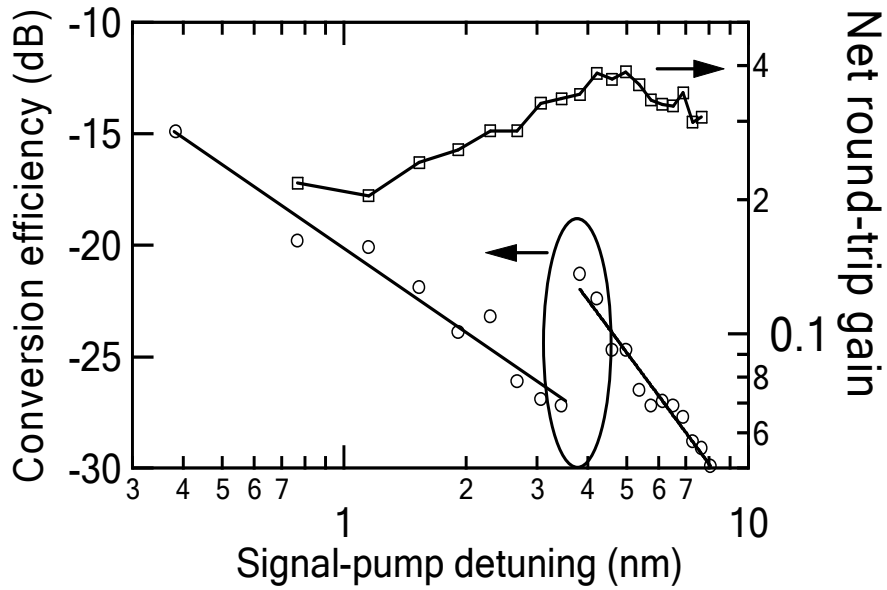


Fig.A2. 4. The FWM conversion efficiency with maximum cavity enhancement versus the detuning in the spectrum presented in fig.3. The net round-trip gain is obtained from the DFB spectrum without FWM using Haiki-Pioli technique.

## Appendix C. MATLAB CODE FOR THE THRESHOLD AND YIELD

### CALCULATIONS OF DFBS

#### 1. dispersion\_relation.m

```

clear all;
%Kfb=input('input Kfb: ');
%Kbf=input('input Kbf: ');
r1_facet=input('input r1: ');
r2_facet=input('input r2: ');
m=30; LL=50; JL=50;
index1=1;index2=1;
s_stat_index=0;
options = optimset('Display','off'); % Turn off Display

for Kfb=0.5:0.5:5

    Kbf=-Kfb; % minus for index coupled, plus for gain coupled

    for k = 0:m
        Kbf
        k
        tic;
        for n = 0:m

            r1=r1_facet*(cos(pi*2.0*k/m)+i*sin(pi*2.0*k/m));
            r2=r2_facet*(cos(pi*2.0*n/m)+i*sin(pi*2.0*n/m));

            index1=1;index2=1;

            for L = 0:LL
                %pp=L
                for J = 0:JL
                    p = (0.2*L)+(0.2*J-5)*i;

                    if abs(threshold1(p,r1,r2,Kfb,Kbf))<1
                        if index1==1
                            SS1(1)=p;
                            index1=2;
                        else
                            if abs(p-SS1(index1-1))>1
                                SS1(index1)=p;
                                index1=index1+1;
                            end
                        end
                    end
                end
            end

            if abs(threshold2(p,r1,r2,Kfb,Kbf))<1
                if index2==1
                    SS2(1)=p;
                    index2=2;
                else
                    if abs(p-SS2(index2-1))>1
                        SS2(index2)=p;
                        index2=index2+1;
                    end
                end
            end
        end
    end
end

```

```

    end
end

%index
s1_index=1;
    for s_index = 1:(index1-1)

        [s_value,f_value] = fsolve(@threshold1,SS1(s_index),options,r1,r2,Kfb,Kbf);
        if (abs(f_value)<0.0001)
            if(s1_index==1)
                Solutions1(k+1,n+1,s1_index)=s_value;
                s1_index=s1_index+1;
            else
                for loop_filter=(1:s1_index-1)
                    if(abs(s_value-Solutions1(k+1,n+1,s1_index-loop_filter))<0.01)
                        solution_match=1;
                        break;
                    else
                        solution_match=0;
                    end
                end
                if(solution_match==0)
                    Solutions1(k+1,n+1,s1_index)=s_value;
                    s1_index=s1_index+1;
                end
            end
        end
    end
end

for s_index=1:(s1_index-1)
    Solutions1(k+1,n+1,s_index)=sqrt(Solutions1(k+1,n+1,s_index)^2-Kfb*Kbf);
    Solutions1(k+1,n+1,s_index)=real(Solutions1(k+1,n+1,s_index))+2*i*imag(Solutions1(k+1,n+1,s_index));
    if (imag(Solutions1(k+1,n+1,s_index))<0)
        Solutions1(k+1,n+1,s_index)=-Solutions1(k+1,n+1,s_index);
    end
end

% change the solution to Beta
% Solutions1(k+1,n+1,s_index)=sqrt(Solutions1(k+1,n+1,s_index)^2-Kfb*Kbf);

% the gain is doubled when considering the gain of amplitude
% Solutions1(k+1,n+1,s_index)=real(Solutions1(k+1,n+1,s_index))+2*i*imag(Solutions1(k+1,n+1,s_index));

s2_index=1;f_value=1;
for s_index = 1:(index2-1)

    [s_value,f_value] = fsolve(@threshold2,SS2(s_index),options,r1,r2,Kfb,Kbf);
    if (abs(f_value)<0.0001)
        if(s2_index==1)
            Solutions2(k+1,n+1,s2_index)=s_value;
            s2_index=s2_index+1;
        else
            for loop_filter=(1:s2_index-1)
                if(abs(s_value-Solutions2(k+1,n+1,s2_index-loop_filter))<0.01)
                    solution_match=1;
                    break;
                else
                    solution_match=0;
                end
            end
            if(solution_match==0)

```

```

        Solutions2(k+1,n+1,s2_index)=s_value;
        s2_index=s2_index+1;
    end
end
end
end

for s_index=1:(s2_index-1)
    Solutions2(k+1,n+1,s_index)=sqrt(Solutions2(k+1,n+1,s_index)^2-Kfb*Kbf);
    Solutions2(k+1,n+1,s_index)=real(Solutions2(k+1,n+1,s_index))+2*i*imag(Solutions2(k+1,n+1,s_index));
    if (imag(Solutions2(k+1,n+1,s_index))<0)
        Solutions2(k+1,n+1,s_index)=-Solutions2(k+1,n+1,s_index);
    end
end

s_min_1(k+1,n+1)=1000*(1+i);
s_min_2(k+1,n+1)=1000*(1+i);

for s_index=1:s1_index-1
    if(abs(Solutions1(k+1,n+1,s_index))<1e-5)|(abs(s_min_1(k+1,n+1)-Solutions1(k+1,n+1,s_index))<1e-4)
        break;
    end
    if(imag(s_min_1(k+1,n+1))>imag(Solutions1(k+1,n+1,s_index)))
        s_min_2(k+1,n+1)=s_min_1(k+1,n+1);
        s_min_1(k+1,n+1)=Solutions1(k+1,n+1,s_index);
    else
        if(imag(s_min_2(k+1,n+1))>imag(Solutions1(k+1,n+1,s_index)))
            s_min_2(k+1,n+1)=Solutions1(k+1,n+1,s_index);
        end
    end
end

end

for s_index=1:s2_index-1

    if(abs(Solutions2(k+1,n+1,s_index))<1e-5)|(abs(s_min_1(k+1,n+1)-Solutions2(k+1,n+1,s_index))<1e-4)
        break;
    end

    if(imag(s_min_1(k+1,n+1))>imag(Solutions2(k+1,n+1,s_index)))
        s_min_2(k+1,n+1)=s_min_1(k+1,n+1);
        s_min_1(k+1,n+1)=Solutions2(k+1,n+1,s_index);
    else
        if(imag(s_min_2(k+1,n+1))>imag(Solutions2(k+1,n+1,s_index)))
            s_min_2(k+1,n+1)=Solutions2(k+1,n+1,s_index);
        end
    end
end

end

s_stat_index=s_stat_index+1;
s_stat(s_stat_index)=imag(s_min_2(k+1,n+1))-s_min_1(k+1,n+1);

end

toc
end

hold on;
h=cdfplot(s_stat);
newz = 1-get(h(1),'Ydata');

```

```

set(h(1),'Ydata',newz,'Color','red');

result_file=['yield_' Kfb num2str(Kfb) '_Kbf' num2str(Kbf) '_r1_' num2str(abs(r1)) '_r2_' num2str(abs(r2)) '.mat']
save(result_file);

end

```

## 2. threshold1.m

```

function y = threshold1(x,r1,r2,Kfb,Kbf)
y = F21(x,Kbf)*r1+F22(x,Kfb,Kbf)-r2*(F11(x,Kfb,Kbf)*r1+F12(x,Kfb));

function y = F11(x,Kfb,Kbf)
y=cos(x)-i*sqrt(x^2-Kfb*Kbf)*sinc(x/pi);

function y = F22(x,Kfb,Kbf)
y=cos(x)+i*sqrt(x^2-Kfb*Kbf)*sinc(x/pi);

function y = F12(x,Kfb)
y=Kfb*sinc(x/pi);

function y = F21(x,Kbf)
y=-Kbf*sinc(x/pi);

```

## 3. threshold2.m

```

function y = threshold2(x,r1,r2,Kfb,Kbf)
y = F21(x,Kbf)*r1+F22(x,Kfb,Kbf)-r2*(F11(x,Kfb,Kbf)*r1+F12(x,Kfb));

function y = F11(x,Kfb,Kbf)
y=cos(x)+i*sqrt(x^2-Kfb*Kbf)*sinc(x/pi);

function y = F22(x,Kfb,Kbf)
y=cos(x)-i*sqrt(x^2-Kfb*Kbf)*sinc(x/pi);

function y = F12(x,Kfb)
y=Kfb*sinc(x/pi);

function y = F21(x,Kbf)
y=-Kbf*sinc(x/pi);

```



## **Appendix D. HIGH GAIN QUANTUM DOT SEMICONDUCTOR OPTICAL AMPLIFIER FOR 1300 NM**

*Abstract*— Using an AlGaAs/GaAs waveguide structure with a six-stack InAs/InGaAs DWELL gain region having an aggregate dot density of approximately  $8 \times 10^{11} \text{ cm}^{-2}$ , an optical gain of 18 dB at 1300 nm has been obtained in a 2.4-mm long amplifier at 100-mA pump current. The optical bandwidth is 50 nm, and the output saturation power is 9 dBm. The dependence of the amplifier parameters on the pump current and the gain recovery dynamics has also been studied.

### 1. DEVICE STRUCTURE AND EXPERIMENT RESULTS

A six-stack InAs/InGaAs “dots-in-a-well” (DWELL) amplifier structure was grown by solid source molecular beam epitaxy on a (001) GaAs substrate using conditions and design criteria similar to those published previously [4,13]. The average dot density in a layer is about  $1.3 \times 10^{11} \text{ cm}^{-2}$ . The amplifier was fabricated using tilted ridge waveguide geometry. The 4-micron ridge was formed with inductively coupled plasma etching using  $\text{BCl}_3$  to remove part of AlGaAs cladding. Self-alignment of the ridge was achieved by protecting it with  $\text{SiN}_x$  during a wet oxidation of the remaining AlGaAs cladding layer. Ti/Pt/Au was evaporated for the metal contact to the  $\text{p}^+$ -GaAs cap layer. The substrate was lapped and polished to a thickness of 100  $\mu\text{m}$  and AuGe/Ni/Au was deposited for the n-type contact. The waveguide length is 2.4 mm. The cleaved facets with a tilt angle of  $6.8^\circ$  were left uncoated and provided a sufficiently low level of back reflection and thus of spectral ripples. Since available lensed fibers were used for coupling without any

optimization, the coupling losses were quite high and all the parameters reported below are given for the amplifier with these fiber-coupling losses de-embedded.

Electroluminescence measurements of the structure (Fig. D.1) show a ground state peak at 1305 nm with a spectral FWHM of 65 nm, indicating good homogeneity of the quantum dots. The origin of the ASE power decrease at currents above 100 mA is due to heating from the parasitic series resistance. It is also possible that a gradual misalignment of the collection optics with temperature could contribute to the decrease in measured power. Nevertheless, the important point is that the position of the ground state does not change appreciably with different pump levels. A possible explanation is that the thermal red shift of the band gap is balanced by a carrier band-filling effect. The spectrum shape doesn't change because it is determined primarily by dot inhomogeneity, which is temperature independent and the excited state population is not significant. Because of the saturation of the ground state energy levels at relatively low pump levels and the resulting occupation of excited energy levels with higher state densities, the blue shift in the QD emission due to band filling could be more significant than in a quantum well. Similar behavior has also been observed in experiments with the QD-SOA chip. The results obtained demonstrate the potential of QD technology for devices with high temperature stability because blue-shifting and red-shifting can be balanced.

A typical spectrum of the ASE in the QD-SOA is presented in Fig. D.2. The ASE maximum (disregarding spectral ripples) is at 1295 nm and the FWHM is 50 nm. The different peak wavelengths and FWHM's between the SOA and the electroluminescence are probably due to material differences across the 2-inch wafer. The Fabry-Perot spectral ripples at operating currents are quite low, < 2 dB, with their period of ~0.1 nm

corresponding to the chip length. It is noted that the slow amplitude modulation in the ripple in Fig. D. 2 is an intrinsic chip feature and is not caused by interference effects from the lensed fibers used for the coupling, because neither the position nor the amplitude of the ripples are fiber tip position dependent. The slow ripple is most probably due to wavelength dependent backreflection because of the mode conversion on the tilted facet [133] and coupling with substrate modes due to the transparency of the GaAs wafer substrate at 1300 nm [134]. The onset of lasing at 1304.5 nm ultimately limits the maximum QD-SOA gain. This indicates that probably even higher gain and obviously lower ripples could be obtained if the chip facets were AR-coated. In Fig. (D. 3) the ASE spectra for no signal and in saturation are presented. For the case where a 1300-nm CW signal is injected, it is seen that the spectral broadening is quasi-homogeneous in a wide spectral range around the gain maximum. This conclusion is supported by the fact that the reduction in the ASE power occurs in a broad wavelength region around the saturating signal. Such a wide homogeneous bandwidth is rather usual for operation of electrically pumped QD-SOA at room temperature when the dephasing time is very short as discussed in Chapter one. In our case of CW operation the inhomogeneous broadening due to dot size distribution is additionally masked by the carrier transport effects, which play an essential role there as could be concluded from the fact that saturation of the ASE power is significantly stronger on the red side than on the blue one.

The dependence of the QD-SOA chip small signal gain at wavelength 1300 nm on the current is presented in Fig. (D.4). The gain was measured by comparing the device gain to that at transparency current (~30 mA), which was determined by monitoring the saturation of the device transmission at high power of input signal. As the waveguide

losses are low,  $<2 \text{ cm}^{-1}$  it gives only a small, maximum 2 dB correction to the gain value. The results show a good agreement with the on/off gain ( $\sim 40 \text{ dB}$ ) and the values obtained from the fiber-to-fiber gain minus the coupling losses ( $\sim 12 \text{ dB}$  per facet), which were estimated by comparing the ASE power coupled in the fiber to the total ASE power. The high loss value is mainly because spherical fiber tapers were used while the light beam had 3:1 ellipticity. The coupling could be improved using, for example, biconic lensed fiber tapers. At currents in the vicinity of the lasing threshold (135 mA) the gain reaches the value of  $\sim 18 \text{ dB}$  ( $17 \text{ cm}^{-1}$ ), which is consistent the data on the ground state saturated gain in a Fabry-Perot laser grown under similar conditions [135]. In QD lasers, gain saturation is usually determined by the complete population of the quantum dot ground state. However, as already mentioned heating could also cause the gain saturation effect (Fig. D.1). The gain has strong, at least 20-dB polarization dependence. It is due to the QD gain polarization dependence – the TM gain maximum is significantly blue shifted either because the light-hole energy levels are not confined within the heavily compressively strained QD or because of the particular shape of the dot. Only if the dot had a symmetric cross-section in the direction of light propagation, the TE and TM ground state gain would be equal. The problem of strong polarization-dependent gain could be relaxed using a double pass with polarization rotation or polarization diversity configurations. In Fig. D.4 the current dependence of the 3-dB gain saturation power (chip output) for a CW signal at 1300 nm is also shown together with the typical dependence of the QD-SOA gain on the output power. Values of  $\sim 9 \text{ dBm}$  output saturation power are achievable. It is comparable with that of common bulk- and MQW-SOA's but it is essentially lower than the values obtained in numerical simulations [30].

Due to the onset of the lasing and heating, strong inversion of the QD ground state and the extremely low differential gain desirable for high saturation power could not be reached. The carrier capture time was also about one order of magnitude longer than that assumed in the simulations as it will be shown further. The linewidth enhancement factor has been estimated by the shift of the ASE spectral ripples in gain saturation as illustrated in Fig. D.5. As it is typical for QD devices, the linewidth enhancement factor is very low -  $\sim 0.1$ . It is essentially lower than the typical value of  $\sim 5$  for MQW-SOA, which was also measured in the same set up for a common commercially available 1300-nm MQW-SOA. From the ASE spectral density the noise figure of the QD-SOA was estimated to be  $\sim 8$  dB taking into account that the ASE is polarized.

The gain recovery dynamics of the QD-SOA sample was also studied. The measurements were based on the beating of two pulse trains with close pulse repetition frequencies. A 1.25-GHz train of 12-ps pulses with the center wavelength of 1300 nm served as the pump. The probe pulse train of 1.5-ps pulses at 1296 nm had 1.25 GHz-125 Hz repetition frequency. The maximum temporal delay is set by the pulse repetition frequency to  $\sim 800$  ps. The QD-SOA gain dynamics for different currents is shown in Fig. D.6 together with the results obtained for a common 1300-nm MQW-SOA. In a conventional MQW-SOA (Fig. D.6 b), for pulses longer than a few picoseconds the relaxation dynamics can be well described by a single exponent and the recovery time is strongly dependent on the carrier density. On the contrary, the recovery dynamics of the QD-SOA gain can be characterized by two time constants. Those were found to be  $\tau_1 \sim 9$  ps  $\tau_2 \sim 140$  ps by fitting a double exponent to the logarithm of the gain recovery profile. It is worth noting that the relaxation time constants were found to be practically

independent of the driving current in the studied range. The dependence of the relaxation time constants on the input pulse energy was also studied. It was found that for up to 4 dB pulse gain saturation there are no pronounced changes in the gain recovery dynamics.

The initial fast incomplete gain recovery with a relaxation time  $\sim 9$  ps could be attributed to several effects. On one side it could be an extensively discussed relaxation bottle neck but usually the carrier relaxation time to the QD ground state is  $\sim 1$  ps, significantly shorter than the observed one. On the other side it could be an interdot (“tunneling”) relaxation between the lateral coupled dots in a QD layer, which could become possible for room temperature at high QD densities, when coupling can lower the barrier between the QD [136,137]. The longer relaxation time constant corresponds to the relaxation of the total carrier density. More detailed investigations, are necessary to clarify the physics of the gain recovery dynamics. But it is out of the scope of the present paper. Especially the second, total carrier density relaxation process with 140-ps time would be an inhibiting factor for high bit rate transmission similar to the case of common bulk and MQW-SOA. Probably the effect might be reduced by optimization of the structure and especially by increasing the pump current [37]. In our case the maximum pump current was limited by the onset of lasing.

## 2. CONCLUSIONS

Parameters of a 1300-nm quantum dot semiconductor optical amplifier built using a 2.4-mm long structure of six InAs/InGaAs DWELL layers with very high dot density ( $8 \times 10^{11} \text{ cm}^{-2}$ ) have been studied. A gain as high as 18 dB with 50-nm bandwidth has been reached at low current (100 mA). The output saturation power for a CW signal is

~9 dBm. The linewidth enhancement factor is below 0.1. The polarization dependence of the gain is more than 20 dB, the noise figure is about 8 dB. Gain peak wavelength and bandwidth are practically temperature independent.

The obtained parameters are better than or comparable to that of a common SOA. It shows prospects of QD-SOA deployment in optical networks because of the ultra-fast gain recovery and the low linewidth enhancement factor, which allow to decrease the signal distortions by cross-gain modulation and chirp generation in high bit rate systems.

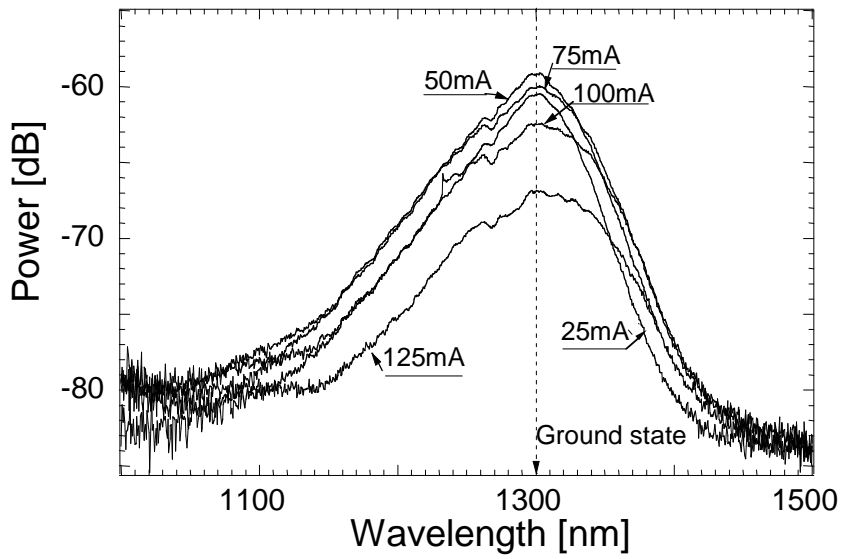


Fig. D.1. Electroluminescence spectra of the DWELL structure with the heat sink temperature fixed at 18°C for different injection currents.

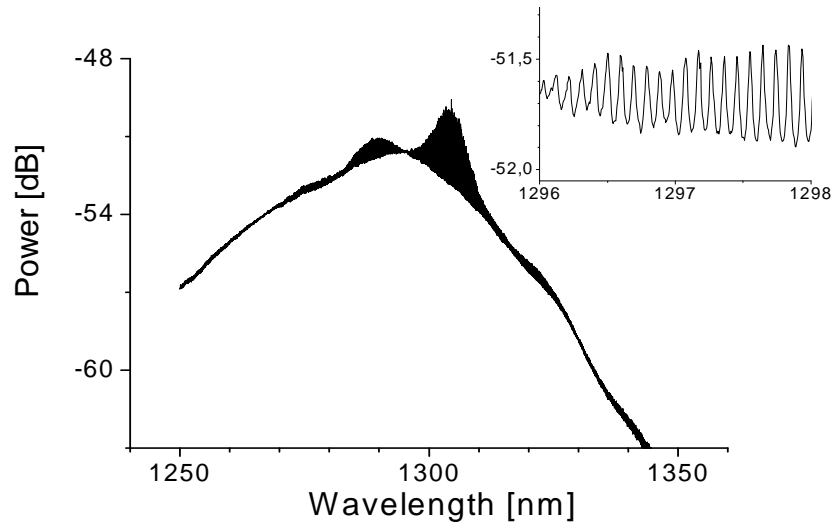


Fig. D.2. ASE spectrum of QD-SOA at the vicinity of the lasing threshold with a magnification of the central part in the inset. Optical resolution bandwidth is 0.01 nm.



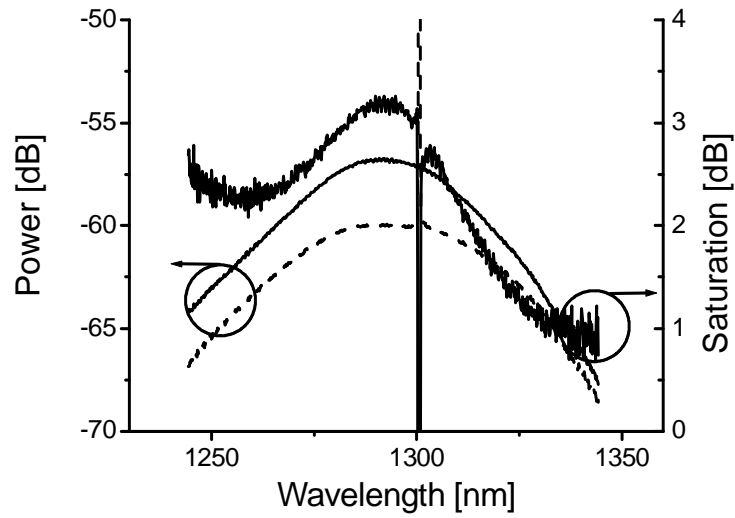


Fig. D.3. ASE spectra without and with a CW signal at 3-dB gain saturation and their ratio. The signal peak is outside the plot area.

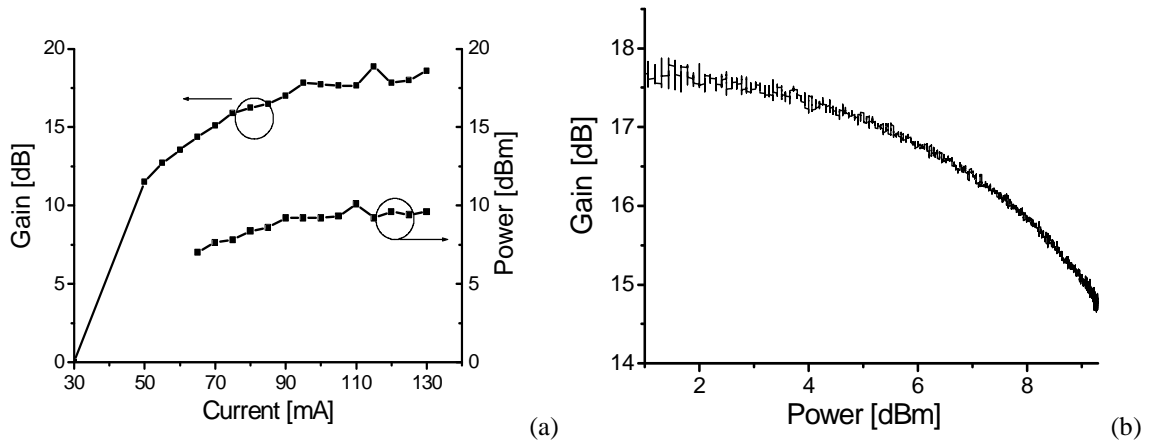


Fig. D.4. The small signal gain and 3-dB saturation output power dependence on current at 1300 nm (a); gain dependence on output power for 100-mA pump current (b). Heat sink temperature was 24°C.

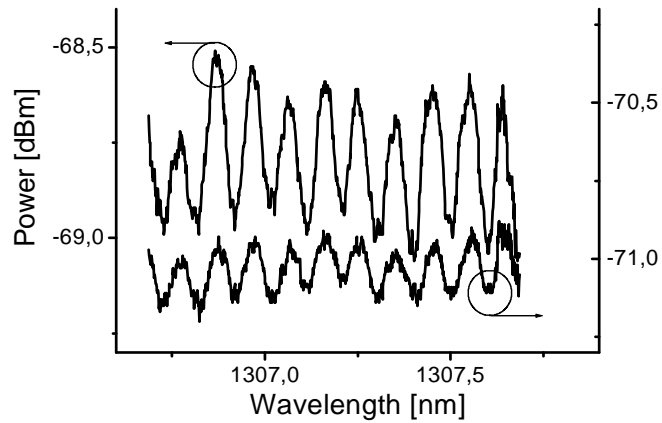


Fig. D.5. ASE spectral ripples without (upper curve) and with CW signal at 2-dB gain saturation (bottom curve) in a QD-SOA ( $\alpha_H \sim 0.1$ ).

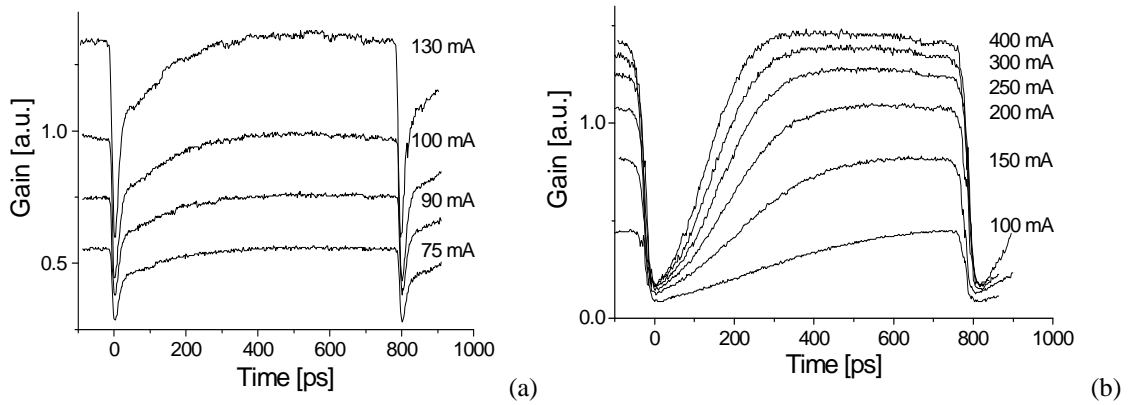


Fig. D.6. Gain recovery dynamics for the QD-SOA (a) and for a common MQW-SOA (b) for different currents. Shift of curves corresponds to the change of the small signal gain. The pump pulse duration: a) 12 ps and b)  $\sim 20$  ps. The input pump pulse energy: a)  $\sim 40$  fJ; b)  $\sim 300$  fJ.

## BIBLIOGRAPHY

1. Y. ARAKAWA and H. SAKAKI, "MULTIDIMENSIONAL QUANTUM WELL LASER AND TEMPERATURE-DEPENDENCE OF ITS THRESHOLD CURRENT," *APPLIED PHYSICS LETTERS* **40**, 939-941.
2. N. KIRSTAEDTER, N. N. LEDENTSOV, M. GRUNDMANN, D. BIMBERG, V. M. USTINOV, S. S. RUVIMOV, M. V. MAXIMOV, P. S. KOPEV, Z. I. ALFEROV, U. RICHTER, P. WERNER, U. GOSELE, and J. HEYDENREICH, "LOW-THRESHOLD, LARGE T-O INJECTION-LASER EMISSION FROM (INGA)AS QUANTUM DOTS," *ELECTRONICS LETTERS* **30**, 1416-1417.
3. N. N. LEDENTSOV, V. M. USTINOV, A. Y. EGOROV, A. E. ZHUKOV, M. V. MAKSIMOV, I. G. TABATADZE, and P. S. KOPEV, "OPTICAL-PROPERTIES OF HETEROSTRUCTURES WITH INGAAS-GAAS QUANTUM CLUSTERS," *SEMICONDUCTORS* **28**, 832-834 (1994).
4. G. T. Liu, A. Stintz, H. Li, K. J. Malloy, and L. F. Lester, "Extremely low room-temperature threshold current density diode lasers using InAs dots in In<sub>0.15</sub>Ga<sub>0.85</sub>As quantum well," *ELECTRONICS LETTERS* **35**, 1163-1165 (1999).
5. M. ASADA, Y. MIYAMOTO, and Y. SUEMATSU, "GAIN AND THE THRESHOLD OF 3-DIMENSIONAL QUANTUM-BOX LASERS," *IEEE JOURNAL OF QUANTUM ELECTRONICS* **22**, 1915-1921 (1986).
6. O. B. Shchekin and D. G. Deppe, "1.3  $\mu$  m InAs quantum dot laser with T<sub>o</sub>=161 K from 0 to 80 degrees C," *APPLIED PHYSICS LETTERS* **80**, 3277-3279 (2002).
7. T. C. Newell, D. J. Bossert, A. Stintz, B. Fuchs, K. J. Malloy, and L. F. Lester, "Gain and linewidth enhancement factor in InAs quantum-dot laser diodes," *IEEE PHOTONICS TECHNOLOGY LETTERS* **11**, 1527-1529 (1999).
8. N. A. Sobolev, A. Cavaco, M. C. Carmo, M. Grundmann, F. Heinrichsdorff, and D. Bimberg, "Enhanced radiation hardness of InAs/GaAs quantum dot structures," *Physica Status Solidi B-Basic Research* **224**, 93-96 (2001).
9. F. Guffarth, R. Heitz, M. Geller, C. Kapteyn, H. Born, R. Sellin, A. Hoffmann, D. Bimberg, N. A. Sobolev, and M. C. Carmo, "Radiation hardness of InGaAs/GaAs quantum dots," *APPLIED PHYSICS LETTERS* **82**, 1941-1943 (2003).
10. Z. Alferov, "Double heterostructure lasers: Early days and future perspectives," *IEEE JOURNAL OF SELECTED TOPICS IN QUANTUM ELECTRONICS* **6**, 832-840 (2000).
11. Bimberg, D. High power single and multimode quantum dot lasers with superior beam profile. Photonics West section 5365[2004.]. 1-26-2004.
12. L. A. Coldren and S. W. Corzine, *Diode lasers and photonic integrated circuits*, (John Wiley & Sons, Inc., 1995).
13. G. T. Liu, A. Stintz, H. Li, T. C. Newell, A. L. Gray, P. M. Varangis, K. J. Malloy, and L. F. Lester, "The influence of quantum-well composition on the performance of quantum dot lasers using InAs/InGaAs dots-in-a-well (DWELL) structures," *IEEE JOURNAL OF QUANTUM ELECTRONICS* **36**, 1272-1279 (2000).

14. N. Kirstaedter, O. G. Schmidt, N. N. Ledentsov, D. Bimberg, V. M. Ustinov, A. Y. Egorov, A. E. Zhukov, M. V. Maximov, P. S. KOPEV, and Z. I. Alferov, "Gain and differential gain of single layer InAs/GaAs quantum dot injection lasers," *APPLIED PHYSICS LETTERS* **69**, 1226-1228 (1996).
15. K. Kamath, J. Phillips, H. Jiang, J. Singh, and P. Bhattacharya, "Small-signal modulation and differential gain of single-mode self-organized In<sub>0.4</sub>Ga<sub>0.6</sub>As/GaAs quantum dot lasers," *APPLIED PHYSICS LETTERS* **70**, 2952-2953 (1997).
16. A. A. Ukhanov, "Study of the Carrier-induced optical properties in III-V quantum confined laser nano-structures," (2004).
17. N. Kirstaedter, N. N. Ledentsov, M. Grundmann, D. Bimberg, V. M. Ustinov, S. S. RUVIMOV, M. V. Maximov, P. S. KOPEV, Z. I. Alferov, U. RICHTER, P. Werner, U. Gosele, and J. HEYDENREICH, "LOW-THRESHOLD, LARGE T-O INJECTION-LASER EMISSION FROM (INGA)AS QUANTUM DOTS," *ELECTRONICS LETTERS* **30**, 1416-1417 (1994).
18. K. Mukai, Y. Nakata, K. Otsubo, M. Sugawara, N. Yokoyama, and H. Ishikawa, "High characteristic temperature of near-1.3- $\mu$ m InGaAs/GaAs quantum-dot lasers at room temperature," *APPLIED PHYSICS LETTERS* **76**, 3349-3351.
19. O. B. Shchekin and D. G. Deppe, "Low-threshold high-T-O 1.3- $\mu$ m InAs quantum-dot lasers due to P-type modulation doping of the active region," *IEEE PHOTONICS TECHNOLOGY LETTERS* **14**, 1231-1233 (2002).
20. D. Bimberg and N. Ledentsov, "Quantum dots: lasers and amplifiers," *JOURNAL OF PHYSICS-CONDENSED MATTER* **15**, R1063-R1076 (2003).
21. K. Mukai, Y. Nakata, K. Otsubo, M. Sugawara, N. Yokoyama, and H. Ishikawa, "High characteristic temperature of near-1.3- $\mu$ m InGaAs/GaAs quantum-dot lasers at room temperature," *APPLIED PHYSICS LETTERS* **76**, 3349-3351.
22. L. V. Asryan and R. A. Suris, "Characteristic temperature of quantum dot laser," *ELECTRONICS LETTERS* **33**, 1871-1872.
23. P. M. Smowton, E. J. Pearce, H. C. Schneider, W. W. Chow, and M. Hopkinson, "Filamentation and linewidth enhancement factor in InGaAs quantum dot lasers," *APPLIED PHYSICS LETTERS* **81**, 3251-3253 (2003).
24. A. V. Uskov, E. P. O'Reilly, D. McPeake, N. N. Ledentsov, D. Bimberg, and G. Huyet, "Carrier-induced refractive index in quantum dot structures due to transitions from discrete quantum dot levels to continuum states," *APPLIED PHYSICS LETTERS* **84**, 272-274 (2004).
25. A. V. Uskov, E. P. O'Reilly, D. McPeake, N. N. Ledentsov, D. Bimberg, and G. Huyet, "Carrier-induced refractive index in quantum dot structures due to transitions from discrete quantum dot levels to continuum states," *APPLIED PHYSICS LETTERS* **84**, 272-274 (2004).
26. P. K. Kondratko, S. L. Chuang, G. Walter, T. Chung, and N. Holonyak, "Observations of near-zero linewidth enhancement factor in a quantum-well coupled quantum-dot laser," *APPLIED PHYSICS LETTERS* **83**, 4818-4820 (2003).
27. S. Fathpour, P. Bhattacharya, S. Pradhan, and S. Ghosh, "Linewidth enhancement factor and near-field pattern in tunnel injection In<sub>0.4</sub>Ga<sub>0.6</sub>As self-assembled quantum dot lasers," *ELECTRONICS LETTERS* **39**, 1443-1445 (2003).

28. Leo H. Spiekman, "Semiconductor Optical Amplifier," *Optical Fiber Telecommunications*, (Elsevier Science, 2002), 699-732.
29. O. Qasaimeh, "Optical gain and saturation characteristics of quantum-dot semiconductor optical amplifiers," *IEEE JOURNAL OF QUANTUM ELECTRONICS* **39**, 793-798 (2003).
30. T. W. Berg and J. Mork, "Quantum dot amplifiers with high output power and low noise," *APPLIED PHYSICS LETTERS* **82**, 3083-3085 (2003).
31. T. Akiyama, M. Ekawa, M. Sugawara, H. Sudo, K. Kawaguchi, A. Kuramata, H. Ebe, K. Morito, H. Imai, and Y. Arakawa, **An Ultrawide-Band (120 nm) Semiconductor Optical Amplifier Having an Extremely-High Penalty-Free Output Power of 23 dBm Realized with Quantum-Dot Active Layers**. ECOC. 2003. 2003.
32. E. U. Rafailov, P. Loza-Alvarez, W. Sibbett, G. S. Sokolovskii, D. A. Livshits, A. E. Zhukov, and V. M. Ustinov, "Amplification of femtosecond pulses over by 18 dB in a quantum-dot semiconductor optical amplifier," *IEEE PHOTONICS TECHNOLOGY LETTERS* **15**, 1023-1025 (2003).
33. Z. Bakonyi, H. Su, G. Onishchukov, L. F. Lester, A. L. Gray, T. C. Newell, and A. Tunnermann, "High-gain quantum-dot semiconductor optical amplifier for 1300 nm," *IEEE JOURNAL OF QUANTUM ELECTRONICS* **39**, 1409-1414 (2003).
34. M. Sugawara, N. Hatori, T. Akiyama, Y. Nakata, and H. Ishikawa, "Quantum-dot semiconductor optical amplifiers for high bit-rate signal processing over 40 Gbit/s," *JAPANESE JOURNAL OF APPLIED PHYSICS PART 2-LETTERS* **40**, L488-L491 (2001).
35. M. Sugawara, T. Akiyama, N. Hatori, Y. Nakata, H. Ebe, and H. Ishikawa, "Quantum-dot semiconductor optical amplifiers for high-bit-rate signal processing up to 160 Gb s<sup>-1</sup> and a new scheme of 3R regenerators," *MEASUREMENT SCIENCE & TECHNOLOGY* **13**, 1683-1691 (2002).
36. T. Akiyama, H. Kuwatsuka, T. Simoyama, Y. Nakata, K. Mukai, M. Sugawara, O. Wada, and H. Ishikawa, "Nonlinear gain dynamics in quantum-dot optical amplifiers and its application to optical communication devices," *IEEE JOURNAL OF QUANTUM ELECTRONICS* **37**, 1059-1065 (2001).
37. T. Akiyama, N. Hatori, Y. Nakata, H. Ebe, and M. Sugawara, "Pattern-effect-free semiconductor optical amplifier achieved using quantum dots," *ELECTRONICS LETTERS* **38**, 1139-1140 (2002).
38. T. Akiyama, N. Hatori, Y. Nakata, H. Ebe, and M. Sugawara, "Pattern-effect-free amplification and cross-gain modulation achieved by using ultrafast gain nonlinearity in quantum-dot semiconductor optical amplifiers," *PHYSICA STATUS SOLIDI B-BASIC RESEARCH* **238**, 301-304 (2003).
39. A. V. Uskov, T. W. Berg, and J. Mork, "Theory of pulse-train amplification without patterning effects in quantum-dot semiconductor optical amplifiers," *IEEE JOURNAL OF QUANTUM ELECTRONICS* **40**, 306-320 (2004).
40. T. Akiyama, N. Hatori, Y. Nakata, H. Ebe, and M. Sugawara, "Pattern-effect-free amplification and cross-gain modulation achieved by using ultrafast gain nonlinearity in quantum-dot semiconductor optical amplifiers," *PHYSICA STATUS SOLIDI B-BASIC RESEARCH* **238**, 301-304 (2003).

41. A. Bilenca, R. Alizon, V. Mikhelashvili, D. Dahan, G. Eisenstein, R. Schwertberger, D. Gold, J. P. Reithmaier, and A. FORCHEL, "Broad-band wavelength conversion based on cross-gain modulation and four-wave mixing in InAs-InP quantum-dash semiconductor optical amplifiers operating at 1550 nm," *IEEE PHOTONICS TECHNOLOGY LETTERS* **15**, 563-565 (2003).
42. O. Qasaimeh, "Characteristics of cross-gain (XG) wavelength conversion in quantum dot semiconductor optical amplifiers," *IEEE PHOTONICS TECHNOLOGY LETTERS* **16**, 542-544 (2004).
43. T. Akiyama, O. Wada, H. Kuwatsuka, T. Simoyama, Y. Nakata, K. Mukai, M. Sugawara, and H. Ishikawa, "Nonlinear processes responsible for nondegenerate four-wave mixing in quantum-dot optical amplifiers," *APPLIED PHYSICS LETTERS* **77**, 1753-1755 (2000).
44. T. Akiyama, H. Kuwatsuka, N. Hatori, Y. Nakata, H. Ebe, and M. Sugawara, "Symmetric highly efficient (similar to 0 dB) wavelength conversion based on four-wave mixing in quantum dot optical amplifiers," *IEEE PHOTONICS TECHNOLOGY LETTERS* **14**, 1139-1141 (2002).
45. T. Akiyama, O. Wada, H. Kuwatsuka, T. Simoyama, Y. Nakata, K. Mukai, M. Sugawara, and H. Ishikawa, "Nonlinear processes responsible for nondegenerate four-wave mixing in quantum-dot optical amplifiers," *APPLIED PHYSICS LETTERS* **77**, 1753-1755 (2000).
46. P. Borri, W. Langbein, J. M. Hvam, F. Heinrichsdorff, M. H. Mao, and D. Bimberg, "Time-resolved four-wave mixing in InAs/InGaAs quantum-dot amplifiers under electrical injection," *APPLIED PHYSICS LETTERS* **76**, 1380-1382 (2000).
47. T. Akiyama, H. Kuwatsuka, T. Simoyama, Y. Nakata, K. Mukai, M. Sugawara, O. Wada, and H. Ishikawa, "Ultrafast nonlinear processes in quantum-dot optical amplifiers," *OPTICAL AND QUANTUM ELECTRONICS* **33**, 927-938 (2001).
48. Bimberg, D. High power single and multimode quantum dot lasers with superior beam profile. *Photonics West section 5365[2004.]*. 1-26-2004.
49. P. M. Varangis, H. Li, G. T. Liu, T. C. Newell, A. Stintz, B. Fuchs, K. J. Malloy, and L. F. Lester, "Low-threshold quantum dot lasers with 201 nm tuning range," *ELECTRONICS LETTERS* **36**, 1544-1545 (2000).
50. H. Li, G. T. Liu, P. M. Varangis, T. C. Newell, A. Stintz, B. Fuchs, K. J. Malloy, and L. F. Lester, "150-nm tuning range in a grating-coupled external cavity quantum-dot laser," *IEEE PHOTONICS TECHNOLOGY LETTERS* **12**, 759-761 (2000).
51. X. D. Huang, A. Stintz, H. Li, L. F. Lester, J. Cheng, and K. J. Malloy, "Passive mode-locking in 1.3  $\mu\text{m}$  two-section InAs quantum dot lasers," *APPLIED PHYSICS LETTERS* **78**, 2825-2827 (2001).
52. M. Kamp, M. Schmitt, J. Hofmann, F. Schafer, J. P. Reithmaier, and A. FORCHEL, "InGaAs/AlGaAs quantum dot DFB lasers operating up to 213 degrees C," *ELECTRONICS LETTERS* **35**, 2036-2037 (1999).
53. F. Klopff, R. Krebs, A. Wolf, M. Emmerling, J. P. Reithmaier, and A. FORCHEL, "InAs/GaInAs quantum dot DFB lasers emitting at 1.3  $\mu\text{m}$ ," *ELECTRONICS LETTERS* **37**, 634-636 (2001).
54. R. Krebs, F. Klopff, S. Rennon, J. P. Reithmaier, and A. FORCHEL, "High frequency characteristics of InAs/GaInAs quantum dot distributed feedback lasers emitting at 1.3  $\mu\text{m}$ ," *ELECTRONICS LETTERS* **37**, 1223-1225 (2001).

55. L.Zhang, R.Wang, Z.Zou, T.Newell, D.Webb, P.Varangis, and L.Lester. InAs quantum dot DFB lasers on GaAs for uncooled 1310nm fiber communications. *Optical Fiber Communication Conference*, Atlanta, GA. 2003.
56. H.Su, L. Zhang A. L. Gray R. Wang T. C. Newell and L. F. Lester. Linewidth study of GaAs-InGaAs Quantum Dot Distributed Feedback Lasers. *IEEE PHOTONICS TECHNOLOGY LETTERS* , accepted. 2004.
57. H. Su, L. Zhang, A. L. Gray, R. Wang, T. C. Newell, K. J. Malloy, and L. F. Lester, "High external feedback resistance of laterally loss-coupled distributed feedback quantum dot semiconductor lasers," *IEEE PHOTONICS TECHNOLOGY LETTERS* **15**, 1504-1506 (2003).
58. M. Sugawara, K. Mukai, and H. Shoji, "Effect of phonon bottleneck on quantum-dot laser performance," *Applied Physics Letters* **71**, 2791-2793 (1997).
59. M. Grundmann, R. Heitz, and D. Bimberg, "New approach to modeling carrier distribution in quantum dot ensembles: Gain and threshold of QD lasers and impact of phonon bottleneck," *Physica E* **2**, 725-728 (1998).
60. X. Q. Li, H. Nakayama, and Y. Arakawa, "Lifetime of confined LO phonons in quantum dots and its impact on phonon bottleneck issue," *Japanese Journal of Applied Physics Part 1-Regular Papers Short Notes & Review Papers* **38**, 473-476 (1999).
61. K. Mukai and M. Sugawara, "Slow carrier relaxation among sublevels in annealed self-formed InGaAs/GaAs quantum dots," *Japanese Journal of Applied Physics Part 1-Regular Papers Short Notes & Review Papers* **37**, 5451-5456 (1998).
62. H. Tsuchiya and T. Miyoshi, "Influence of phonon bottleneck on a quantum dot laser," *Solid-State Electronics* **42**, 1443-1447 (1998).
63. K. Ikeda, H. Sekiguchi, F. Minami, J. Yoshino, Y. Mitsumori, H. Amanai, S. Nagao, and S. Sakaki, "Phonon bottleneck effects in InAs/GaInP quantum dots," *Journal of Luminescence* **108**, 273-276 (2004).
64. J. Urayama, T. B. Norris, J. Singh, and P. Bhattacharya, "Observation of phonon bottleneck in quantum dot electronic relaxation," *PHYSICAL REVIEW LETTERS* **86**, 4930-4933 (2001).
65. T. S. Sosnowski, T. B. Norris, H. Jiang, J. Singh, K. Kamath, and P. Bhattacharya, "Rapid carrier relaxation in In<sub>0.4</sub>Ga<sub>0.6</sub>As/GaAs quantum dots characterized by differential transmission spectroscopy," *PHYSICAL REVIEW B-CONDENSED MATTER* **57**, R9423-R9426 (1998).
66. S. Ghosh, P. Bhattacharya, E. Stoner, J. Singh, H. Jiang, S. Nuttinck, and J. Laskar, "Temperature-dependent measurement of Auger recombination in self-organized In<sub>0.4</sub>Ga<sub>0.6</sub>As/GaAs quantum dots," *APPLIED PHYSICS LETTERS* **79**, 722-724 (2001).
67. I. P. Marko, A. D. Andreev, A. R. Adams, R. Krebs, J. P. Reithmaier, and A. FORCHEL, "Importance of Auger recombination in InAs 1.3 μm quantum dot lasers," *ELECTRONICS LETTERS* **39**, 58-59 (2003).
68. X. Q. Li, H. Nakayama, and Y. Arakawa, "Phonon bottleneck in quantum dots: Role of lifetime of the confined optical phonons," *PHYSICAL REVIEW B-CONDENSED MATTER* **59**, 5069-5073 (1999).
69. P. Borri, S. Schneider, W. Langbein, U. Woggon, A. E. Zhukov, V. M. Ustinov, N. N. Ledentsov, Z. I. Alferov, D. Ouyang, and D. Bimberg, "Ultrafast carrier dynamics and dephasing in InAs

- quantum-dot amplifiers emitting near 1.3- $\mu$ m-wavelength at room temperature," *APPLIED PHYSICS LETTERS* **79**, 2633-2635 (2001).
70. P. Eliseev, H. Li, A. Stintz, G. T. Liu, T. C. Newell, K. J. Malloy, and L. F. Lester, "Tunable grating-coupled laser oscillation and spectral hole burning in an InAs quantum-dot laser diode," *IEEE JOURNAL OF QUANTUM ELECTRONICS* **36**, 479-485 (2000).
  71. D. GAMMON, S. RUDIN, T. L. REINECKE, D. S. KATZER, and C. S. KYONO, "PHONON BROADENING OF EXCITONS IN GAAS/ALXGA1-XAS QUANTUM-WELLS," *PHYSICAL REVIEW B-CONDENSED MATTER* **51**, 16785-16789 (1995).
  72. P. Borri, W. Langbein, J. M. Hvam, E. Heinrichsdorff, M. H. Mao, and D. Bimberg, "Ultrafast gain dynamics in InAs-InGaAs quantum-dot amplifiers," *IEEE PHOTONICS TECHNOLOGY LETTERS* **12**, 594-596 (2000).
  73. K. Kim, J. Urayama, T. B. Norris, J. Singh, J. Phillips, and P. Bhattacharya, "Gain dynamics and ultrafast spectral hole burning in In(Ga)As self-organized quantum dots," *APPLIED PHYSICS LETTERS* **81**, 670-672 (2002).
  74. D. A. Yarotski, R. D. Averitt, N. Negre, S. A. Crooker, A. J. Taylor, G. P. Donati, A. Stintz, L. F. Lester, and K. J. Malloy, "Ultrafast carrier-relaxation dynamics in self-assembled InAs/GaAs quantum dots," *JOURNAL OF THE OPTICAL SOCIETY OF AMERICA B-OPTICAL PHYSICS* **19**, 1480-1484 (2002).
  75. P. Borri, W. Langbein, J. M. Hvam, F. Heinrichsdorff, M. H. Mao, and D. Bimberg, "Spectral hole-burning and carrier-heating dynamics in quantum-dot amplifiers: Comparison with bulk amplifiers," *PHYSICA STATUS SOLIDI B-BASIC RESEARCH* **224**, 419-423 (2001).
  76. M. Sugawara, T. Akiyama, N. Hatori, Y. Nakata, H. Ebe, and H. Ishikawa, "Quantum-dot semiconductor optical amplifiers for high-bit-rate signal processing up to 160 Gb s(-1) and a new scheme of 3R regenerators," *MEASUREMENT SCIENCE & TECHNOLOGY* **13**, 1683-1691 (2002).
  77. G. P. AGRAWAL, "SPECTRAL HOLE-BURNING AND GAIN SATURATION IN SEMICONDUCTOR-LASERS - STRONG-SIGNAL THEORY," *Journal of Applied Physics* **63**, 1232-1234 (1988).
  78. T. Akiyama, H. Kuwatsuka, T. Simoyama, Y. Nakata, K. Mukai, M. Sugawara, O. Wada, and H. Ishikawa, "Ultrafast nonlinear processes in quantum-dot optical amplifiers," *OPTICAL AND QUANTUM ELECTRONICS* **33**, 927-938 (2001).
  79. M. Sugawara, T. Akiyama, N. Hatori, Y. Nakata, H. Ebe, and H. Ishikawa, "Quantum-dot semiconductor optical amplifiers for high-bit-rate signal processing up to 160 Gb s(-1) and a new scheme of 3R regenerators," *MEASUREMENT SCIENCE & TECHNOLOGY* **13**, 1683-1691 (2002).
  80. T. Akiyama, N. Hatori, Y. Nakata, H. Ebe, and M. Sugawara, "Pattern-effect-free semiconductor optical amplifier achieved using quantum dots," *ELECTRONICS LETTERS* **38**, 1139-1140 (2002).
  81. A. V. Uskov, E. P. O'Reilly, D. McPeake, N. N. Ledentsov, D. Bimberg, and G. Huyet, "Carrier-induced refractive index in quantum dot structures due to transitions from discrete quantum dot levels to continuum states," *APPLIED PHYSICS LETTERS* **84**, 272-274 (2004).
  82. P. Borri, W. Langbein, J. Mork, J. M. Hvam, F. Heinrichsdorff, M. H. Mao, and D. Bimberg, "Dephasing in InAs/GaAs quantum dots," *PHYSICAL REVIEW B* **60**, 7784-7787 (1999).



83. A. Stintz, G. T. Liu, A. L. Gray, R. Spillers, S. M. Delgado, and K. J. Malloy, "Characterization of InAs quantum dots in strained In<sub>x</sub>Ga<sub>1-x</sub>As quantum wells," *JOURNAL OF VACUUM SCIENCE & TECHNOLOGY B* **18**, 1496-1501 (2000).
84. M. Kamp, J. Hofmann, F. Schafer, M. Reinhard, M. Fischer, T. Bleuel, J. P. Reithmaier, and A. FORCHEL, "Lateral coupling - a material independent way to complex coupled DFB lasers," *OPTICAL MATERIALS* **17**, 19-25 (2001).
85. P. Bhattacharya, D. Klotzkin, O. Qasaimeh, W. D. Zhou, S. Krishna, and D. H. Zhu, "High-speed modulation and switching characteristics of In(Ga)As-Al(Ga)As self-organized quantum-dot lasers," *IEEE JOURNAL OF SELECTED TOPICS IN QUANTUM ELECTRONICS* **6**, 426-438 (2000).
86. D. Bimberg, N. Kirstaedter, N. N. Ledentsov, Z. I. Alferov, P. S. KOPEV, and V. M. Ustinov, "InGaAs-GaAs quantum-dot lasers," *IEEE JOURNAL OF SELECTED TOPICS IN QUANTUM ELECTRONICS* **3**, 196-205 (1997).
87. L.A.Coldren and S.W.Corzine, *Diode lasers and Photonics Integrated Circuits*, (John Wiley & Sons, INC., 1995).
88. M. W. FLEMING and A. MOORADIAN, "SPECTRAL CHARACTERISTICS OF EXTERNAL-CAVITY CONTROLLED SEMICONDUCTOR-LASERS," *IEEE Journal of Quantum Electronics* **17**, 44-59 (1981).
89. M. R. MATTHEWS, K. H. CAMERON, R. WYATT, and W. J. DEVLIN, "PACKAGED FREQUENCY-STABLE TUNABLE 20 KHZ LINEWIDTH 1.5-MU-M INGAASP EXTERNAL CAVITY LASER," *Electronics Letters* **21**, 113-115 (1985).
90. E. PATZAK, A. SUGIMURA, S. SAITO, T. MUKAI, and H. OLESEN, "SEMICONDUCTOR-LASER LINEWIDTH IN OPTICAL FEEDBACK CONFIGURATIONS," *Electronics Letters* **19**, 1026-1027 (1983).
91. M. OKAI, "SPECTRAL CHARACTERISTICS OF DISTRIBUTED-FEEDBACK SEMICONDUCTOR-LASERS AND THEIR IMPROVEMENTS BY CORRUGATION-PITCH-MODULATED STRUCTURE," *Journal of Applied Physics* **75**, 1-29 (1994).
92. M. OKAI, M. SUZUKI, T. TANIWATARI, and N. CHINONE, "CORRUGATION-PITCH-MODULATED DISTRIBUTED-FEEDBACK LASERS WITH ULTRANARROW SPECTRAL LINEWIDTH," *Japanese Journal of Applied Physics Part 1-Regular Papers Short Notes & Review Papers* **33**, 2563-2570 (1994).
93. S. TAKANO, T. SASAKI, H. YAMADA, M. KITAMURA, and I. MITO, "SUB-MHZ SPECTRAL LINEWIDTH IN 1.5-MU-M SEPARATE-CONFINEMENT-HETEROSTRUCTURE (SCH) QUANTUM-WELL DFB LDS," *Electronics Letters* **25**, 356-357 (1989).
94. G.P.Agrawal, "Coherent Lightwave Systems," *Fiber-Optic communication systems*, (Wiley Interscience, 2002), 478-512.
95. H. OLESEN, B. TROMBORG, H. E. LASSEN, and X. PAN, "MODE-INSTABILITY AND LINEWIDTH REBROADENING IN DFB LASERS," *Electronics Letters* **28**, 444-446 (1992).
96. X. PAN, B. TROMBORG, and H. OLESEN, "LINEWIDTH REBROADENING IN DFB LASERS DUE TO WEAK SIDE MODES," *IEEE Photonics Technology Letters* **3**, 112-114 (1991).

97. H. WENZEL, H. J. WUNSCH, and U. BANDELOW, "LINEWIDTH REBROADENING IN SEMICONDUCTOR-LASERS DUE TO LATERAL SPATIAL HOLEBURNING," *Electronics Letters* **27**, 2301-2302 (1991).
98. G. P. AGRAWAL, G. H. DUAN, and P. GALLION, "INFLUENCE OF REFRACTIVE-INDEX NONLINEARITIES ON MODULATION AND NOISE PROPERTIES OF SEMICONDUCTOR-LASERS," *Electronics Letters* **28**, 1773-1774 (1992).
99. F. Girardin, G. H. DUAN, and P. GALLION, "Linewidth rebroadening due to nonlinear gain and index induced by carrier heating in strained quantum-well lasers," *IEEE Photonics Technology Letters* **8**, 334-336 (1996).
100. T. OKOSHI, K. KIKUCHI, and A. NAKAYAMA, "NOVEL METHOD FOR HIGH-RESOLUTION MEASUREMENT OF LASER OUTPUT SPECTRUM," *Electronics Letters* **16**, 630-631 (1980).
101. Bin Zhao and Amnon Yariv, "Quantum well semiconductor lasers," *Semiconductor lasers I Fundamentals*, Eli Kapon, ed., (Academic press, 1999), 1-109.
102. K. PETERMANN, "EXTERNAL OPTICAL FEEDBACK PHENOMENA IN SEMICONDUCTOR-LASERS," *IEEE Journal of Selected Topics in Quantum Electronics* **1**, 480-489 (1995).
103. M. F. Alam and M. A. Karim, "External optical feedback effects in distributed feedback semiconductor lasers," *Advances in Imaging and Electron Physics, Vol 107* **107**, 73-120 (1999).
104. T. OKOSHI, K. KIKUCHI, and A. NAKAYAMA, "NOVEL METHOD FOR HIGH-RESOLUTION MEASUREMENT OF LASER OUTPUT SPECTRUM," *Electronics Letters* **16**, 630-631 (1980).
105. K. H. Park, J. K. Lee, J. H. Han, H. S. Cho, D. H. Jang, C. S. Park, K. E. Pyun, and J. Jeong, "The effects of external optical feedback on the power penalty of DFB-LD modules for 2.5 Gb s(-1) optical transmission systems," *Optical and Quantum Electronics* **30**, 23-31 (1998).
106. G.P.Agrawal, *Fiber-Optic communication systems*, (John Wiley and Sons Inc, 1997).
107. K. Inoue, "An experimental study on chirp noise in a directly modulated semiconductor laser," *Ieice Transactions On Communications* **E81B**, 1197-1202 (1998).
108. J. FENG, T. R. CHEN, and A. YARIV, "ON CHIRP CONTROL IN 2 SECTION DISTRIBUTED-FEEDBACK SEMICONDUCTOR-LASERS," *Applied Physics Letters* **67**, 2913-2915 (1995).
109. C. Y. Tsai and C. Y. Tsai, "Effects of carrier heating on the frequency chirping of semiconductor lasers," *Electronics Letters* **33**, 2043-2045 (1997).
110. M. Bhattacharya, R. Mukherjee, and T. Chattopadhyay, "Reduction of frequency chirping in semiconductor lasers through injection locking," *Iete Journal of Research* **45**, 341-344 (1999).
111. R. Vinzio, Z. Toffano, and A. Destrez, "Analytical formulation of distortion and chirp in CATV DFB lasers including spatial hole burning," *IEEE Journal of Quantum Electronics* **34**, 311-317 (1998).

112. G. E. Shtengel, R. F. Kazarinov, G. L. Belenky, and C. L. Reynolds, "Wavelength chirp and dependence of carrier temperature on current in MQW InGaAsP-InP lasers," *IEEE Journal of Quantum Electronics* **33**, 1396-1402 (1997).
113. H. Saito, K. Nishi, A. Kamei, and S. Sugou, "Low chirp observed in directly modulated quantum dot lasers," *IEEE PHOTONICS TECHNOLOGY LETTERS* **12**, 1298-1300 (2000).
114. H. Saito, K. Nishi, and S. Sugou, "Low chirp operation in 1.6  $\mu\text{m}$  quantum dot laser under 2.5 GHz direct modulation," *ELECTRONICS LETTERS* **37**, 1293-1295 (2001).
115. K. Petermann, *Laser diode modulation and noise*, (Kluwer Academic Publishers, 1991).
116. Agilent Technologies. Making Time-Resolved Chirp Measurements using the optical spectrum analyzer and digital communication analyzer. 2004. Application Note 1550-7.
117. H. Li, "RF-modulation measurement of linewidth enhancement factor and nonlinear gain of vertical-cavity surface-emitting lasers," *IEEE Photonics Technology Letters* **8**, 1594-1596 (1996).
118. L.A. Coldren and S.W. Corzine, *Diode lasers and Photonics Integrated Circuits*, (John Wiley & Sons, INC., 1995), 213-221.
119. N. S. BERGANO, "WAVELENGTH DISCRIMINATOR METHOD FOR MEASURING DYNAMIC CHIRP IN DFB LASERS," *Electronics Letters* **24**, 1296-1297 (1988).
120. Douglas M. Baney and Wayne V. Sorin, "high resolution optical frequency analysis," *Fiber optic test and measurement*, Dennis Derickson, ed., (Prentice Hall, 1998), 206-207.
121. Agilent Technologies. Making Time-Resolved Chirp Measurements using the optical spectrum analyzer and digital communication analyzer. 2002. Application Note 1550-7.
122. L.A. Coldren and S.W. Corzine, *Diode lasers and Photonics Integrated Circuits*, (John Wiley & Sons, INC., 1995), 213-221.
123. Radhakrishnan Nagarajan and John E. Bowers, "High-speed Lasers," *Semiconductor lasers I Fundamentals*, Eli Kapon, ed., (Academic press, 1999), 177-290.
124. G.P. Agrawal, *Fiber-Optic communication systems*, (John Wiley & Sons, Inc., 2002).
125. J. Minch and S. L. Chuang, "Dual-pump four-wave mixing in a double-mode distributed feedback laser," *JOURNAL OF THE OPTICAL SOCIETY OF AMERICA B-OPTICAL PHYSICS* **17**, 53-62 (2000).
126. H. Kuwatsuka, H. Shoji, M. Matsuda, and H. Ishikawa, "Nondegenerate four-wave mixing in a long-cavity  $\lambda/4$ -shifted DFB laser using its lasing beam as pump beams," *IEEE JOURNAL OF QUANTUM ELECTRONICS* **33**, 2002-2010 (1997).
127. J. R. Minch, C. S. Chang, and S. L. Chuang, "Wavelength conversion in distributed-feedback lasers," *IEEE JOURNAL OF SELECTED TOPICS IN QUANTUM ELECTRONICS* **3**, 569-576 (1997).
128. I. Tomkos, I. Zacharopoulos, E. Roditi, and D. Syvridis, "Experimental investigation of wavelength conversion based on four-wave mixing in a three-electrode distributed feedback laser," *APPLIED PHYSICS LETTERS* **75**, 1195-1197 (1999).

129. H. Ishikawa, "Applications of quantum dot to optical devices," *SELF-ASSEMBLED INGAAS/GAAS QUANTUM DOTS* **60**, 287-323 (1999).
130. T. Akiyama, H. Kuwatsuka, N. Hatori, Y. Nakata, H. Ebe, and M. Sugawara, "Symmetric highly efficient (similar to 0 dB) wavelength conversion based on four-wave mixing in quantum dot optical amplifiers," *IEEE PHOTONICS TECHNOLOGY LETTERS* **14**, 1139-1141 (2002).
131. P. Borri, W. Langbein, J. M. Hvam, F. Heinrichsdorff, M. H. Mao, and D. Bimberg, "Time-resolved four-wave mixing in InAs/InGaAs quantum-dot amplifiers under electrical injection," *APPLIED PHYSICS LETTERS* **76**, 1380-1382 (2000).
132. B.W.Hakki and T.L.Paoli, "Gain spectra in GaAs double-heterostructure injection lasers," *Journal of applied physics* **46**, 1299-1306 (1975).
133. A. Vukovic, P. Sewell, T. M. Benson, and P. C. Kendall, "Advances in facet design for buried lasers and amplifiers," *IEEE Journal of Selected Topics in Quantum Electronics* **6**, 175-184 (2000).
134. P. G. ELISEEV and A. E. DRAKIN, "ANALYSIS OF THE MODE INTERNAL COUPLING IN INGAAS/GAAS LASER-DIODES," *Laser Physics* **4**, 485-492 (1994).
135. Y. Qiu, P. Gogna, S. Forouhar, A. Stintz, and L. F. Lester, "High-performance InAs quantum-dot lasers near 1.3  $\mu$  m," *Applied Physics Letters* **79**, 3570-3572 (2001).
136. A. Patane, A. Levin, A. Polimeni, L. Eaves, P. C. Main, M. Henini, and G. Hill, "Carrier thermalization within a disordered ensemble of self-assembled quantum dots," *Physical Review B* **62**, 11084-11088 (2000).
137. Z. X. Ma and K. Pierz, "Carrier thermalization and activation within self-assembled InAs/AlAs quantum dot states," *Surface Science* **511**, 57-64 (2002).